ZIRCON FROM SWIFT CREEK STAGE ERUPTIONS RECORDS THE ASSEMBLY AND EVOLUTION OF AN INTRUSIVE MAGMATIC COMPLEX BENEATH MOUNT ST. HELENS

By

Daniel M. Flanagan

Thesis

Submitted to the Faculty of the

Graduate School of Vanderbilt University

in partial fulfillment of the requirements

for the degree of

MASTER OF SCIENCE

in

Earth and Environmental Sciences

December, 2009

Nashville, Tennessee

Approved:

Professor Calvin F. Miller

Professor John C. Ayers

ACKNOWLEDGEMENTS

This study would not have been possible without the guidance of Prof. Calvin Miller, who is a walking encyclopedia of geologic knowledge and just may be the most patient man on the planet. Calvin is the embodiment of what every geologist and student advisor should strive to be, and working with him has made this project a valuable and enriching experience. I also owe a great deal of appreciation to Lily Claiborne, who served as both collaborator and mentor during the course of my research. Lily frequently and graciously donated her time and expertise to all facets of this project and there is no way to adequately describe how immensely helpful she has been. Mike Clynne and Ed Wolfe of the U.S. Geological Survey shared their abundant knowledge of Mount St. Helens deposits and took time out of their summer field season to provide invaluable assistance with sample collection. Without their efforts, this project could not have been nearly as successful as it has turned out to be. I am additionally grateful to Joe Wooden and Frank Mazdab of the Stanford/U.S. Geological Survey Microanalysis Center for the many hours of technical support that they have lent to SHRIMP analysis of zircon grains. Lastly, I would like to thank Profs. John Ayers and Guil Gualda for providing technical advice, as well as Tamara Carley, Lindy Colombini, Ashley Bromley, and Ayla Pamukcu for assistance with fieldwork, sample preparation, and SHRIMP analyses. Financial support for this project was provided by the National Science Foundation.

TABLE OF CONTENTS

LIST OF TABLES

LIST OF FIGURES

CHAPTER I

INTRODUCTION

Although numerous recent studies suggest that large felsic plutonic systems accumulate in small increments over timescales of 10^5–10^6 years (e.g., Bolhar et al., 2008; Claiborne et al., in revision; Coleman et al., 2004; Glazner et al., 2004; Lipman, 2007; Miller et al., 2007; Walker et al., 2007), disagreement persists over how these systems connect to volcanic complexes. One prominent hypothesis splits plutonic and volcanic rocks into separate realms; it states that large plutons preserved in the crust rarely existed as integrated, liquid-rich magma bodies and thus could not have been the source of sizeable volcanic eruptions (e.g., Coleman et al., 2004; Glazner et al., 2004). Alternatively, many authors contend that large silicic plutons record complex, multi-stage histories of growth, fractionation, solidification, rejuvenation, interaction with new magma batches, and melt segregation (e.g., Bolhar et al., 2008; Claiborne et al., in revision; Lipman, 2007; Shane et al., 2008; Walker et al., 2007), which suggest the existence of mobile, eruptible melt. These studies create an integrated model of volcanic and plutonic rocks in which plutons are the terminal record of multiple intrusive and differentiation events while volcanic rocks provide an instantaneous snapshot of the magmatic system (e.g., Bachmann et al., 2007). This model also suggests that the quantity, composition, and temperature of melt fluctuate in both time and space, but precise time-temperature-composition pathways of magmatic systems have not yet been documented. Furthermore, most studies pertaining to the construction of magmatic systems and the volcano-pluton connection have focused on large-scale batholiths, and as a result, very little is known about the manner and timescale of assembly of smaller-scale plutonic and volcanic systems.

The accessory mineral zircon ($ZrSiO_4$) is an ideal resource for investigating the evolution of magmatic systems and the connection between pluton construction and volcanism. Widespread in intermediate to felsic igneous rocks, zircon concentrates elements that act as useful geochemical and geochronological tracers (e.g., Hoskin and Schaltegger, 2003). Magmatic temperatures can also be determined through the Ti-in-zircon thermometer, which is based on the temperature-dependent partitioning of Ti between zircon and melt (Ferry and Watson, 2007; Watson et al., 2006). Due to negligible elemental diffusivities under most geologic conditions (e.g., Cherniak et al., 1997a; Cherniak et al., 1997b; Cherniak and Watson, 2003), zircon frequently retains chemical

zoning down to the sub-micron scale and a single grain may record multiple generations of growth with unique elemental and isotopic signatures. Thus, combined in situ trace element and radiometric age analyses of multiple zones within individual zircon grains provide the time-temperature-composition history of the magma(s) from which the zircons grew, and zircons from volcanic rocks may retain a record of the magmatic conditions within an underlying intrusive complex.

The study presented here utilizes zircon grains from rocks erupted during the Swift Creek stage (16–10 ka) of Mount St. Helens to investigate the evolution and construction of an arc magmatic system. It is part of a broader ongoing investigation (Claiborne et al., in prep.) of zircon within eruptive units spanning the entire history of the volcano (Table 1). This contribution focuses on the Swift Creek stage because it is a time period that marks an

Table 1. The eruptive history of Mount St. Helens

Eruptive stage	Eruptive period	Preserved eruptive products
Spirit Lake (3.9 ka–present)	Modern (1980 CE–present)	dacite domes, pyroclastic flows, tephras & blast deposit
	Goat Rocks (1800–1857 CE)	dacite dome, pyroclastic flows & tephras; andesite lava flow
	Kalama (1479–1750 CE)	dacite domes, pyroclastic flows & tephras; andesite pyroclastic flows, lava flows & tephra
	Sugar Bowl (1.2–1.15 ka)	dacite domes & blast deposit
	Castle Creek (2.2–1.895 ka)	basalt pyroclastic flow; basalt, basaltic andesite & andesite lava flows; basalt, basaltic andesite, andesite & dacite tephras
	Pine Creek (3.0–2.5 ka)	dacite domes, pyroclastic flows & tephras
	Smith Creek (3.9–3.3 ka)	dacite domes, pyroclastic flows & tephras
Swift Creek (16–10 ka)	–	dacite dome, pyroclastic flows & clasts within lahars; dacite & andesite tephras
Cougar (28–18 ka)	–	dacite pyroclastic flows & clasts in debris avalanche & lahar deposits; andesite-dacite lava flow; dacite (& andesite?) tephras
Ape Canyon (300–35 ka)	–	dacite & andesite domes; dacite tephras & clasts within glacial deposits, lahars & Cougar-stage debris avalanche deposit

With the exception of the Swift Creek stage, the ages of all eruptive stages and periods are from Clynne et al. (2008). See Mullineaux and Crandell (1981) and Mullineaux (1996) for a detailed description of the Spirit Lake stage and Clynne et al. (2008) for summaries of the Ape Canyon, Cougar, and Swift Creek stages.

important transition in both the eruptive and deep-seated histories of Mount St. Helens, as it is the first eruptive stage characterized by well-developed compositional cycles and extensive interaction between different magma batches (Clynne et al., 2008). Thorough sampling of units erupted during this relatively brief timeframe may also provide a more detailed view of the magmatic processes that occur beneath Mount St. Helens than is afforded by

broad sampling of numerous eruptive products. This study is one of the first to combine trace element and U-Th analyses of an accessory mineral, allowing us to discern fluctuations in magmatic conditions over shorter timescales (10^3–10^4 yrs.) than previously documented. We show that assembly of the Mount St. Helens magmatic system has occurred over hundreds of thousands of years by repeated intrusion of magma bodies that have stalled and crystallized to produce a storage zone beneath the volcano that is frequently rejuvenated by subsequent pulses of magma. Older (>~60–100 ka) zircon analyses document growth from relatively fractionated melts while younger zircon growth zones generally document less evolved melts. Our data also extend recent findings pertaining to the protracted evolution and construction of large plutons to small-scale arc volcanic systems.

CHAPTER II

MOUNT ST. HELENS

Geologic setting, eruptive history, and proposed magma origins

Mount St. Helens is a Quaternary stratovolcano located on the western edge of the Cascades volcanic arc in southwestern Washington. The volcano lies along the St. Helens seismic zone, a linear 100-km-long region of high seismicity, and its location corresponds to an offset in fault segments along this zone that favors local crustal extension (Weaver et al., 1987). The edifice of Mount St. Helens has been constructed upon the glaciated, dissected remains of a mid-Tertiary region of the Cascades arc. Bedrock exposures in the surrounding area range in age from 28–23 Ma and consist of shallow intrusions and volcanic and volcaniclastic rocks that represent basaltic cones and shields, andesite composite cones, and dacite domes (Evarts et al., 1987). This assemblage has been gently folded (strata dip uniformly east at an angle of 20–25^{o}) and affected by pervasive zeolite-facies metamorphism.

Mount St. Helens has a diverse and long-lived eruptive history. Preserved eruptive units predominantly consist of dacite domes, tephras, and pyroclastic flows, but andesite domes and basalt to andesite lava flows and tephras have also been occasionally produced (Table 1). The eruptive history of the volcano was originally documented over a period of thirty years by D.R. Mullineaux and D.R. Crandell, who described the eruptive products of the volcano in detail (Crandell, 1987; Mullineaux and Crandell, 1981; Mullineaux, 1996), established initial age control on lithologic units by radiocarbon dating of organic material within and adjacent to volcanic deposits (Crandell et al., 1981), and organized the eruptive history into four stages of activity (Table 1). Long considered to be relatively youthful (~40 ka), new geologic mapping and radiometric dating indicate that eruptions of Mount St. Helens have occurred for, at least, the past 300 k.y. (Clynne et al., 2008).

There is no general consensus on the origin of Mount St. Helens dacite, the most frequent and voluminous eruptive product manufactured by the volcano. Low concentrations of incompatible trace elements in the dacites in comparison to Mount St. Helens basalts argues against petrogenesis by fractional crystallization from mafic magma while partial melting models support derivation by melting of metasomatized mafic lower crust (Smith and Leeman, 1987). On the other hand, Berlo et al. (2004) favor production by fractional crystallization from mantle-derived parents and argue that partial melting of crustal rocks cannot produce the U-series disequilibria observed in the

dacites. Alternatively, it has been proposed that Mount St. Helens dacites result from partial melting of subducted oceanic crust (Defant and Drummond, 1993). Trace element contents of Mount St. Helens basalts suggest generation from a heterogeneous mantle source containing both mid-ocean ridge and ocean island basalt reservoirs (Smith and Leeman, 1993) while the andesites most plausibly represent mixtures of dacite and basalt (Gardner et al., 1995; Pallister et al., 1992; Smith and Leeman, 1993).

The Swift Creek stage

Except where otherwise noted, the description of the Swift Creek stage (16–10 ka) presented in this section summarizes (with a few minor modifications) the stratigraphy, ages, petrography, and geochemistry documented by Clynne et al. (2008). Lithologic units emplaced during this time period include two groups of airfall tephra layers (sets S and J) and three debris fans produced by lahars and collapse of growing lava domes (the Swift Creek, Crescent Ridge, and Cedar Flats fans). Lithic pyroclastic flows that occur within the Timberline section (Fig. 1) were also deposited during this time period, but their relation to other Swift Creek eruptive units is unclear. Differences in relative proportions and textural characteristics of phenocrysts suggest that the fans were produced by disruption of several dacite domes.

The set S tephras consist of five layers of mostly pumice lapilli and bombs with minor ash (Mullineaux, 1996). Pumice clasts from all layers predominantly exhibit phenocrysts of plagioclase, hornblende, and cummingtonite, but smaller amounts of hypersthene are also present. Geochemical analyses of pumice from uppermost layers Sg and So yield 62–66% SiO_2 (Fig. 2). The precise ages of all Swift Creek eruptive units are unknown; radiocarbon ages reported in the literature conflict with one another and in many cases are not internally consistent and/or do not agree with eruptive stratigraphy. Many samples also likely yield minimum ages because they were not pretreated to reduce contamination by modern organic material. Taken as a whole, the available radiocarbon data suggest an eruption age of ~15.5 ka for layers Sg and So (Fig. 3). The older layers of tephra set S lack weathering horizons and thus are likely no more than a few hundred years older (Mullineaux, 1996).

The Swift Creek fan is ~30 m thick and occurs south of the Mount St. Helens edifice in the drainage of the West Fork of Swift Creek (Fig. 1). The early portion of the fan consists of pumiceous and lithic pyroclastic flow deposits of predominantly cummingtonite-bearing plagioclase, hornblende, and hypersthene dacite with 67% SiO_2 while lithic pyroclastic flows of plagioclase-hornblende-hypersthene dacite with 64–65% SiO_2 mostly make up the

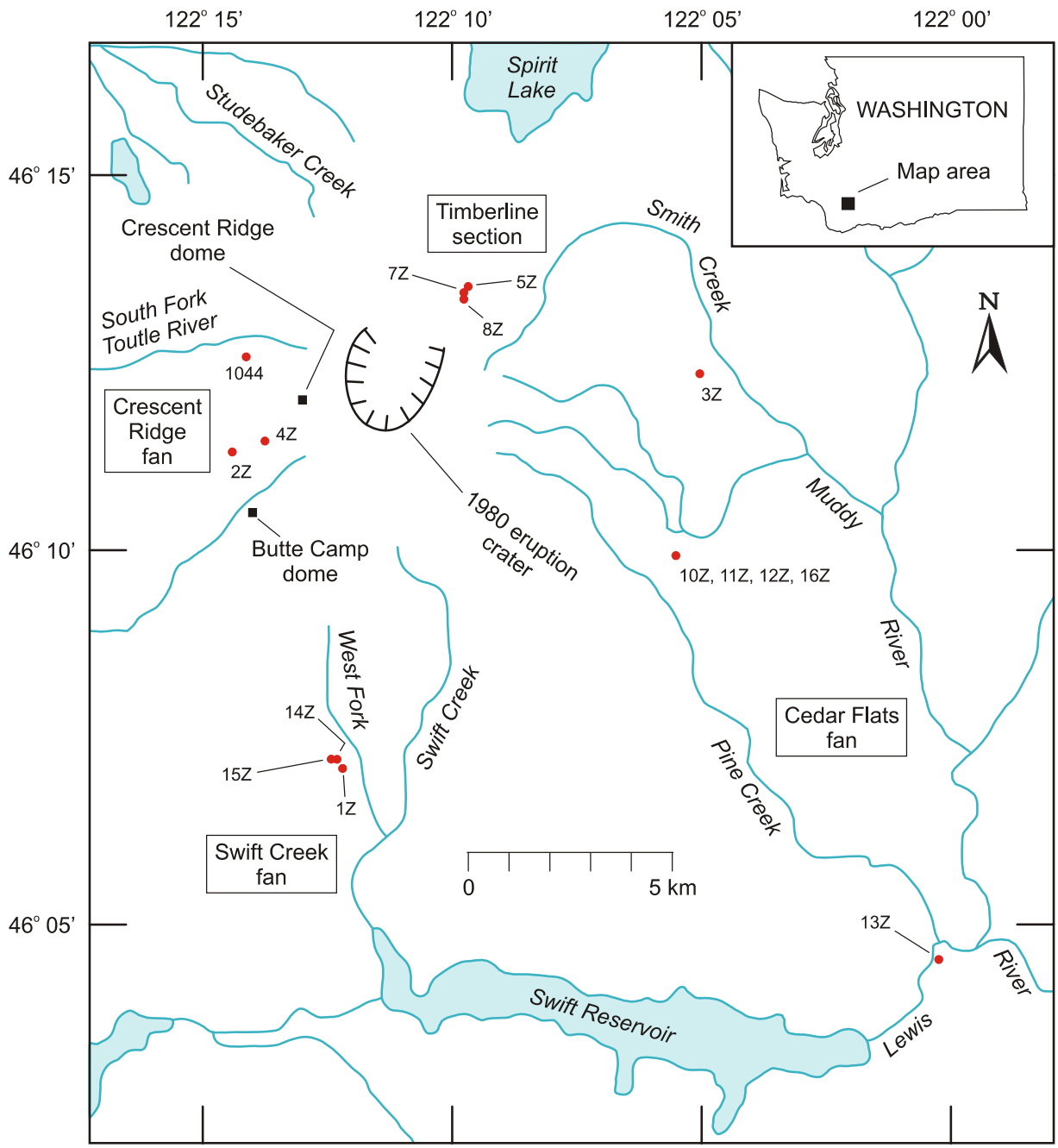

Figure 1. Sketch map of the Mount St. Helens area showing the approximate locations of debris fans erupted during the Swift Creek stage (denoted with boxes). Sample collection sites are marked with red circles and domes mentioned in the text are marked with black squares. The location coordinates of each sample are listed in Table 2.

later portion of the fan (Fig. 2). Stratigraphic relationships indicate that the early deposits predate late set S tephras and that the later deposits postdate set S tephras. Although the precise timeframe of accumulation is ambiguous, available radiocarbon dates suggest final emplacement of the fan by ~15 ka (Fig. 3).

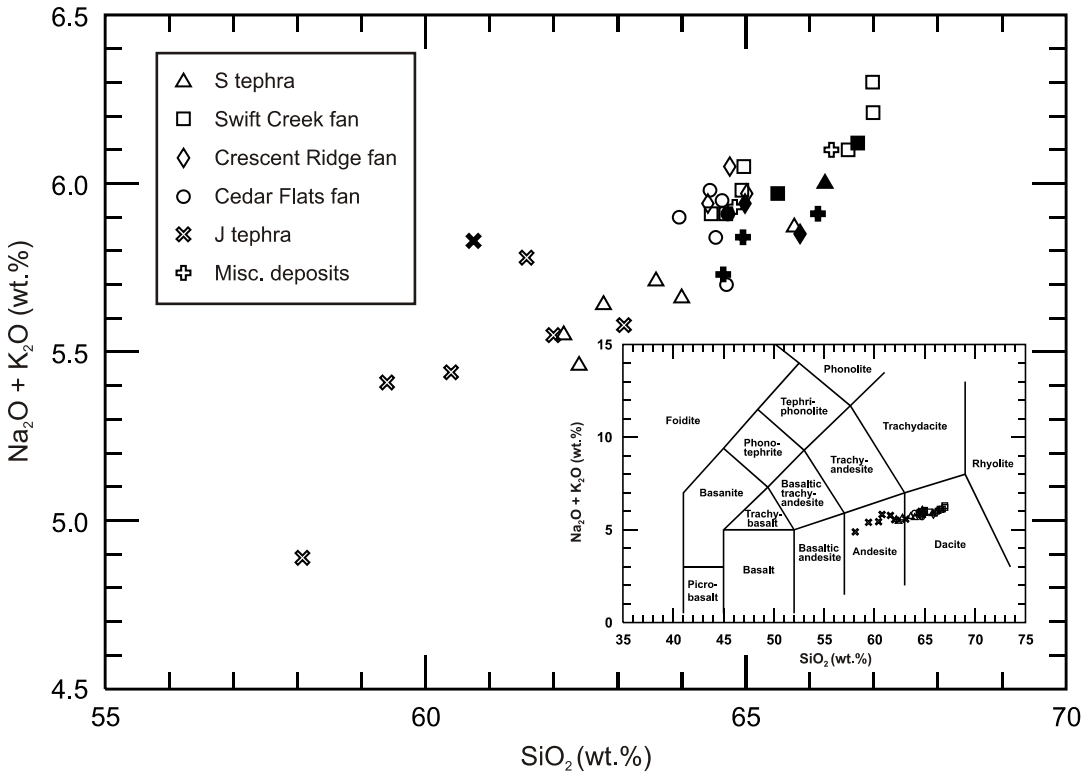

Figure 2. Total alkalies vs. silica diagram for eruptive units of the Swift Creek stage. Samples include analyses performed as part of this study (represented by filled symbols), recent U.S. Geological Survey analyses (M.A. Clynne, unpublished data), and analyses compiled from the literature (Clynne et al., 2008; Crandell, 1987; Halliday et al., 1983; Mullineaux, 1996; Smith and Leeman, 1987). All analyses were recalculated to 100% volatile free following the procedure outlined in Table 3. Rock classification scheme is from Le Bas et al. (1986).

The Crescent Ridge fan, located on the northwest and west flanks of the volcano, is at least 200 m thick and extends from the Studebaker Creek area southward to the Butte Camp dome region (Fig. 1). Pyroclastic flow deposits in this fan fall into two lithologic groups that contain 64–66% SiO_2 (Fig. 2). The lower (early) deposits primarily consist of pumiceous plagioclase-hornblende-cummingtonite dacite with sparse hypersthene, and the upper (later) deposits mostly contain lithic plagioclase-hornblende-hypersthene dacite with sparse augite. The portion of the Crescent Ridge dome that is currently exposed (Fig. 1) has composition and mineralogy similar to that of the early deposits, but the fan may have also originated from a now-buried portion of the Crescent Ridge dome or other domes that are no longer exposed. Stratigraphic relationships indicate that the Crescent Ridge fan probably completely overlies set S tephras and the Swift Creek fan, as no layers of these units have been found within or above it. Preliminary paleomagnetic data indicate that the early and late portions differ in age by no more than decades or centuries and the only available radiocarbon age suggests emplacement around 14 ka (Fig. 3).

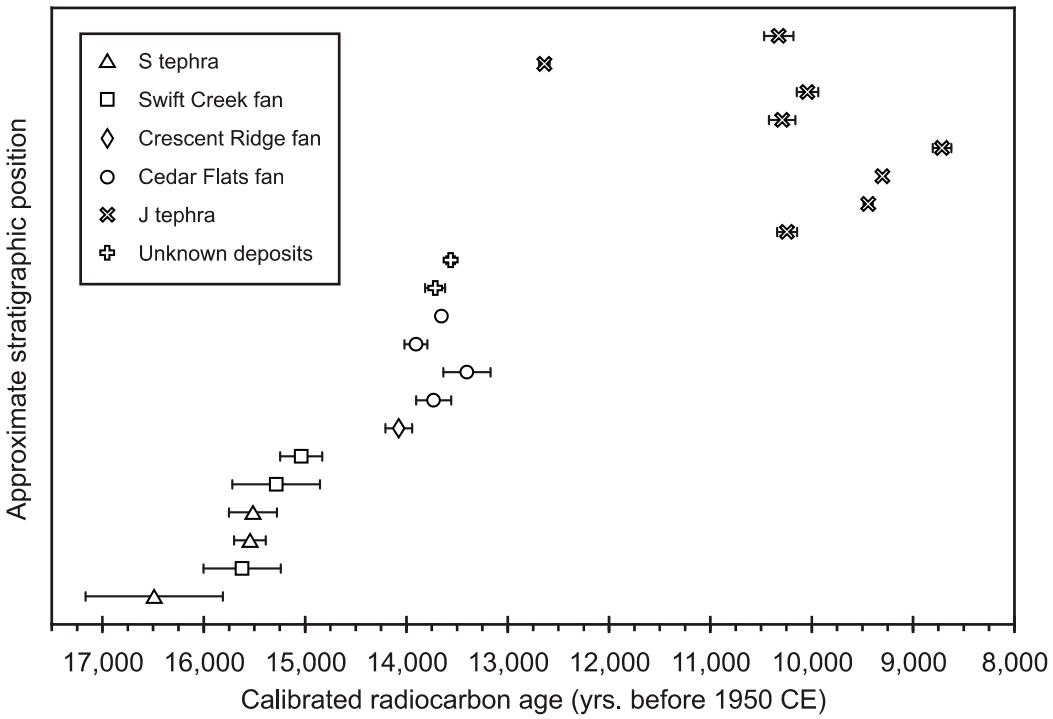

Figure 3. Dated samples for eruptive units of the Swift Creek stage showing 1σ error bars. Samples include recent U.S. Geological Survey radiocarbon analyses (M.A. Clynne, unpublished data), radiocarbon ages compiled from the literature (Baker and Bunker, 1985; Crandell et al., 1981; Hyde, 1975; Major and Scott, 1988; Waitt, 1985), and a date determined by fitting the paleomagnetic profile of sediment layers below tephra layer Sg to the profiles of the well-dated Mono Lake, CA and Fish Lake, OR sediment records (Clague et al., 2003). Compiled samples comprise all available ages for Swift Creek stage eruptive units with the exception of radiocarbon dates based on analysis of peats, which tend to yield erroneously old ages. All samples have been calibrated by M.A. Clynne using the curve of Fairbanks et al. (2005). The unknown deposits occur at the base of the set J tephras and are likely part of the Cedar Flats fan.

The Cedar Flats fan accumulated in the valley of Pine Creek, where it is at least 100 m thick, and spilled into the Lewis River valley, where it has a thickness of 50–100 m (Fig. 1). Lahar deposits make up the majority of the fan, but lithic pyroclastic flows also occur. Most clasts within the fan have plagioclase, hornblende, and hypersthene phenocrysts and contain 64–65% SiO_2 (Fig. 2). The Cedar Flats fan postdates set S tephras and the Swift Creek fan, and available radiocarbon ages suggest emplacement sometime between ~14 and 13 ka (Fig. 3).

Set J tephras primarily consist of coarse pumice lapilli and bombs with minor ash (Mullineaux, 1996). The early tephra layers (Js and Jy) are hornblende-hypersthene silicic andesite with 62–63% SiO_2 while the later tephras (Jb and Jg) are hornblende-hypersthene andesite (layer Jg also contains sparse augite) with 58–61% SiO_2 (Fig. 2). Set J tephras overlie all other known deposits of the Swift Creek stage and lack weathering horizons, indicating that they are probably closely spaced in time. Available radiocarbon ages are contradictory, but taken as a whole suggest

accumulation between ~10.5 and 10 ka (Fig. 3). The separation in radiocarbon ages between sets S and J (Fig. 3) is substantiated by the presence of a weathered and oxidized horizon at the top of layer So and oxidized ash-rich deposits that separate it from J on uplands near the volcanic edifice (Mullineaux, 1996).

We chose the Swift Creek stage for detailed study because it appears to represent an important transition in both the eruptive and deep-seated histories of the Mount St. Helens magmatic system. First, the Swift Creek stage potentially represents the first well-developed magmatic cycles of the volcano (Clynne et al., 2008). Unlike most Mount St. Helens rocks, eruptive products of the Ape Canyon stage (300–35 ka) commonly contain quartz and biotite, indicating that early magmas were relatively cool and wet. Mount St. Helens occasionally erupted cool and wet magmas, as indicated by the presence of cummingtonite phenocrysts, throughout the Cougar stage (28–18 ka), but most Cougar stage rocks lack quartz, biotite, and cummingtonite and thus represent hotter, drier, less evolved magmas than those produced during the Ape Canyon stage. The Swift Creek stage marks a shift from the poorly developed compositional cycles of previous stages to well-developed phases in volcanic activity. It began with the eruption of cummingtonite-bearing dacite (the set S tephras) and culminated with the emplacement of hot, dry andesite (the set J tephras). The early portions of both the Swift Creek and Crescent Ridge fans also document cooler, wetter conditions while the later portions indicate eruption of hotter, drier magmas, and set J pumice becomes more mafic with time. During the ongoing Spirit Lake stage (3.9 ka–present), eruptive behavior has become significantly more complex, with frequent compositional cycles that take place over short time intervals (e.g., Mullineaux and Crandell, 1981; Mullineaux, 1996). Basalt and basaltic andesite also appeared for the first time and andesite has erupted with greater frequency than in any of the preceding stages.

The Swift Creek stage might also mark the first eruptive stage during which extensive interaction occurred between different batches of magma (Clynne et al., 2008). Equilibrium textures of major phenocryst phases suggest that interaction between magma reservoirs was limited throughout much of the Ape Canyon stage (although data presented here suggest exchange of zircon crystals among different magma bodies during this time period). More complex phenocryst textures and a mixed-magma lava flow imply that the magmatic system was more integrated during the Cougar stage, but features indicative of strong disequilibrium are typically absent. In contrast, plagioclase and hornblende phenocrysts in Swift Creek stage eruptive units commonly display evidence of reheating, resorption, and reaction with their host melts, and some dacites also contain reacted cummingtonite or augite.

CHAPTER III

METHODS

Sample preparation and analytical techniques

We collected representative samples of as many Swift Creek stage eruptive lithologies as possible (see Fig. 1 for sample locations and Table 2 for sample descriptions) and attempted to extract zircon grains from each of them. Approximately 5 kg of each sample was crushed to pass through a 500 μm mesh and separated using hydraulic, heavy-liquid, and magnetic techniques at Vanderbilt University. Up to ~125 zircon grains per sample were hand-picked from the least magnetic fraction using a binocular microscope. In order to avoid contamination, many samples were washed to remove colluvium and/or hand-picked to eliminate lithic clasts and other extraneous materials prior to separation. Thirty to fifty zircons (or less) from each sample were mounted in epoxy, polished to expose grain interiors, photographed in reflected light on a petrographic microscope, and imaged by cathodoluminescence (CL) on the JEOL JSM 5600 scanning electron microscope at the Stanford/U.S. Geological Survey Microanalysis Center at Stanford University.

Individual zircon grains were analyzed for trace elements and ^{238}U-^{230}Th crystallization ages using the Stanford/USGS sensitive high resolution ion microprobe, reverse geometry (SHRIMP-RG). Spots were chosen for analysis based on zoning visible in CL images and in an attempt to avoid inclusions, cracks, and other grain defects visible in CL and reflected light images. Analyzed spots are representative of the zircon populations found within each sample, but also highlight interesting features such as sector zoning, resorption surfaces, and other important grain attributes. Where possible, multiple trace element and radiometric age analyses were performed on single grains and U-Th measurements were taken at the same spots used for trace element analysis in order to observe the compositional and thermal evolution of the zircons (and hence their host melts) with time. Data were collected during two analytical sessions (August 2008 and January 2009) with identical methods. Protocols for trace element analysis and data reduction followed Lowery Claiborne et al. (2006) while techniques for U-Th analysis are similar to those described in Wilson and Charlier (2009). During our second data collection session, analytical spots from the first session that yielded U-Th crystallization ages within error of the equiline (≥350 ka) were re-analyzed for ^{238}U-^{206}Pb ages following the methods of Booth et al. (2004).

Table 2. List of collected Swift Creek stage samples

Sample #	Location [a]	Eruptive unit [b]	Distinguishing minerals [c]	Zircon grains yielded [d]
SC08-1044	46° 12' 34.95" N 122° 14' 7.65" W	lower Crescent Ridge fan (pumiceous p.f.)	cummingtonite, hypersthene	10s of grains
SHD08-1Z	46° 7' 5.04" N 122° 12' 11.76" W	Swift Creek fan (lithic p.f.)	hypersthene	none
SHD08-2Z	46° 11' 18.66" N 122° 14' 24.42" W	Jg tephra (airfall pumice)	hypersthene, augite	<10 grains
SHD08-3Z	46° 12' 21.36" N 122° 5' 2.16" W	pre-J surge deposit (pumice)	cummingtonite	100s of grains
SHD08-4Z	46° 11' 27.48" N 122° 13' 45.06" W	upper Crescent Ridge fan (lithic p.f.)	hypersthene, augite	–
SHD08-5Z	46° 13' 31.26" N 122° 9' 40.68" W	Timberline section (lithic p.f.)	cummingtonite	100s of grains
SHD08-7Z	46° 13' 26.40" N 122° 9' 45.90" W	Timberline section (lithic p.f.)	hypersthene	10s of grains
SHD08-8Z	46° 13' 21.14" N 122° 9' 45.89" W	Timberline section (lithic p.f.)	cummingtonite	10s of grains
SHD08-10Z	46° 9' 55.56" N 122° 5' 30.84" W	Jy tephra (airfall pumice)	hypersthene	–
SHD08-11Z	"	Jb tephra (airfall pumice)	hypersthene	–
SHD08-12Z	"	Sg tephra (airfall pumice)	cummingtonite, hypersthene	100s of grains
SHD08-13Z	46° 4' 31.89" N 122° 0' 14.62" W	Cedar Flats fan (lithic p.f.)	hypersthene	10s of grains
SHD08-14Z	46° 7' 12.36" N 122° 12' 18.54" W	early Swift Creek fan (lithic p.f.)	cummingtonite, hypersthene	100s of grains
SHD08-15Z	46° 7' 12.49" N 122° 12' 25.55" W	later Swift Creek fan (lithic p.f.)	hypersthene	10s of grains
SHD08-16Z	46° 9' 55.56" N 122° 5' 30.84" W	Cedar Flats fan (lithic p.f.)	hypersthene	10s of grains

[a] Datum for location coordinates is North American 1927.
[b] p.f. = pyroclastic flow
[c] All samples also contain plagioclase, hornblende, magnetite, ilmenite (?), and apatite.
[d] To date, attempts to separate zircon grains from samples SHD08-4Z, -10Z, and -11Z have been unsuccessful.

All samples that were analyzed for zircon geochemistry and geochronology were analyzed for whole-rock geochemistry. Two additional samples were also selected for geochemical analysis in order to obtain representative compositions of all Swift Creek debris fans and tephras. Rock powders were prepared from unaltered portions of the samples using an alumina ceramic shatter box at Vanderbilt University (SHD08-2Z, -14Z, and -15Z) and a mild steel shatter box (SC08-1044, SHD08-3Z, -4Z, -5Z, -8Z, -12Z, and -13Z) at Activation Laboratories Ltd. (Ancaster,

Ontario, Canada). Prior to pulverization, 1–5 mm chips of weathered samples (SC08-1044, SHD08-3Z and -12Z) and samples analyzed for whole-rock U-series disequilibria (SHD08-2Z, -14Z and -15Z; L.L. Claiborne, K.M. Cooper, and D.M. Flanagan, unpublished data) were ultrasonically cleaned in successive baths of 0.1M oxalic acid + 2% H_2O_2 and 0.1M HCl + 2% H_2O_2 in order to reduce incipient alteration. Major and trace element analyses were performed by Activation Laboratories using a combination of inductively coupled plasma mass spectrometry and instrumental neutron activation analysis.

Determination of zircon crystallization age populations present in each sample

^{238}U-^{230}Th model ages were calculated as two-point isochrons between the zircon analysis and inferred melt values of ($^{238}U/^{232}Th$) and ($^{230}Th/^{232}Th$), where parentheses denote an activity ratio. Determining activity ratios that accurately represent the melt composition associated with each zircon analysis is challenging because zircon crystals typically reside in magmas to which they are not cognate (e.g., Bacon and Lowenstern, 2005; Claiborne et al., in revision; Miller et al., 2007; Walker et al., 2007; Wilson and Charlier, 2009). Most measured ($^{238}U/^{232}Th$) and ($^{230}Th/^{232}Th$) values of Mount St. Helens rocks range from 1.0–1.4 and cluster around 1.2 (Cooper and Donnelly, 2008; L.L. Claiborne, K.M. Cooper, and D.M. Flanagan, unpublished data). We thus chose ($^{238}U/^{232}Th$) = ($^{230}Th/^{232}Th$) = 1.2 as a likely average value for Mount St. Helens magmas. Using the Isoplot 3.0 software package (Ludwig, 2003), we fit measured ($^{238}U/^{232}Th$) and ($^{230}Th/^{232}Th$) values from each sample onto the smallest number of statistically viable isochrons (based on MSWD and probability) that accurately represent all or most of the data. All isochrons were constrained to intercept the equiline at 1.2 and an age for each population was calculated from the slope of the associated isochron. Since assuming a whole-rock value of ($^{238}U/^{232}Th$) = ($^{230}Th/^{232}Th$) = 1.2 for each zircon analysis introduces additional uncertainty into the isochron ages, we calculated a maximum and minimum age for each population by constraining the associated isochron to intercept the equiline at 1.0 and 1.4, respectively. However, because Th/U ratios of the zircons are high, model ages and isochrons are not very sensitive to the choice of initial activity ratio; in almost all cases, the maximum and minimum age for each isochron differs from the calculated isochron age by <5 k.y. As a test on the isochron ages, we also utilized Isoplot to create probability density curves for each sample and to discriminate statistically meaningful age populations using the "Unmix" function (see Sambridge and Compston, 1994 for details). Note that the Unmix algorithm requires the user to identify the number of age populations present within a sample. In order to independently determine this value, we

gradually increased the number of populations until the relative misfit parameter (Sambridge and Compston, 1994) did not significantly change (<0.05). While determination of the isochron ages and use of the Unmix function both require some degree of subjectivity, consistency within samples between the isochron ages, peaks in the probability density curves, and ages yielded by the Unmix function permit confidence in our interpretations.

Ti-in-zircon thermometer

The Ti-in-zircon thermometer (Ferry and Watson, 2007; Watson et al., 2006) describes the temperature dependence of Ti uptake into zircon. It was developed from both synthetic and well-characterized natural zircons and has been calibrated for temperatures ranging from 580–1400 °C at 1.0 ± 0.5 GPa. We utilized the Ferry and Watson (2007) calibration of the thermometer, $T(K) = \frac{-(4800 \pm 86)}{\log[\text{Ti conc. (ppm)}] + \log(\alpha_{SiO_2}) - \log(\alpha_{TiO_2}) - (5.711 \pm 0.072)}$, to estimate crystallization temperatures of Swift Creek stage zircons. Accurate utilization of the thermometer requires reasonably well-constrained values for the activity of SiO_2 and TiO_2 (α_{SiO_2} and α_{TiO_2}) at the time of zircon crystallization. This is problematic, as we cannot utilize whole-rock or glass compositions to pinpoint these values because they may not represent the original host melts from which zircons grew and because α_{SiO_2} and α_{TiO_2} can vary throughout the evolution of a magma. However, natural glass compositions demonstrate that silicic melts typically have α_{TiO_2} values of 0.6–0.9 at geologically relevant temperatures (Hayden and Watson, 2007) and melt compositions and temperatures required for zircon growth generally restrict α_{TiO_2} to >0.5 (Watson and Harrison, 2005). Using the rutile (TiO_2) solubility equation of Hayden and Watson (2007), we calculated α_{TiO_2} of glasses within Spirit Lake stage rocks (Blundy and Cashman, 2005; L.L. Claiborne, unpublished data; Gardner et al., 1995; Pallister et al., 2008) across a range of relevant temperatures in order to constrain the characteristic values of Mount St. Helens melts. No glass analyses exist for pre-Spirit Lake stage rocks, but whole-rock compositions of Swift Creek stage rocks are similar to rocks of the Spirit Lake stage (Clynne et al., 2008). At temperatures indicated by the composition of magnetite-ilmenite pairs in contact with melt, most of the glasses have α_{TiO_2} between 0.5 and 0.7. These likely represent minimum values at the time of zircon crystallization because zircon typically crystallizes later than magnetite and ilmenite (i.e., at a lower temperature) and calculated activity values increase with decreasing temperature. Since no Mount St. Helens rocks contain rutile (i.e., $\alpha_{TiO_2} < 1$), we estimate that the maximum α_{TiO_2} of Mount St. Helens melts is ~0.9. We therefore utilize $\alpha_{TiO_2} = 0.7$ in our calculations of zircon crystallization

temperatures and we quantify the uncertainty in the estimated temperatures due to fluctuations in α_{TiO_2} by varying it from 0.5–0.9. Since growth of zircon grains generally occurs at or near quartz saturation, we assign a value of 1 to α_{SiO_2}.

CHAPTER IV

RESULTS

Zircon within Swift Creek stage samples

We successfully extracted zircon from eleven out of the fifteen collected samples (Table 2). The presence of abundant zircon in Swift Creek rocks generally correlates with the presence of cummingtonite phenocrysts; most of the eruptive units that yielded hundreds of zircon grains contain cummingtonite while those that yielded lesser amounts do not, although sample SC08-1044, a cummingtonite-bearing pumice, yielded very few grains. Out of these eleven samples, eight (SHD08-2Z, -3Z, -5Z, -8Z, -12Z, -13Z, -14Z, and -15Z) were selected for detailed trace element and crystallization age analysis. The selected samples encompass at least one eruptive unit from each of the Swift Creek debris fans and tephras except for the Crescent Ridge fan.

Zircon grains from the samples chosen for analysis are mostly euhedral and prismatic, but a small proportion are slightly rounded, and acicular and stubby, subequant grains are also common (Fig. 4). Extracted grains vary widely in size, but prismatic and stubby grains are typically no more than ~250 μm long and ~100 μm wide while acicular grains are typically ~250–400 μm long (a few grains range up to 500 μm) and ~50–100 μm wide. The zircons exhibit a diverse array of zoning patterns, including thin to thick euhedral growth bands (Figs. 4a–d), thin bands of oscillatory zoning (Figs. 4e–g), sector zoning (Figs. 4h–j), and striped zoning (Figs. 4k–m) that occur in numerous different combinations within individual grains. Growth bands are commonly truncated by curved boundaries and embayments, likely indicating grain resorption due to periods of melt undersaturation in zircon. While there is no obvious correlation between the morphology and zoning patterns exhibited by the zircon grains, similar grain populations (i.e., grains that exhibit similar morphology and zoning) are present in varying proportions in most samples. Samples SHD08-13Z and -15Z, however, contain grains that are much more weakly zoned (Fig. 4c). An exceedingly small number of zircon grains (<5) show evidence of possible recrystallization in CL images, and these areas were avoided during the trace element and radiometric age analyses.

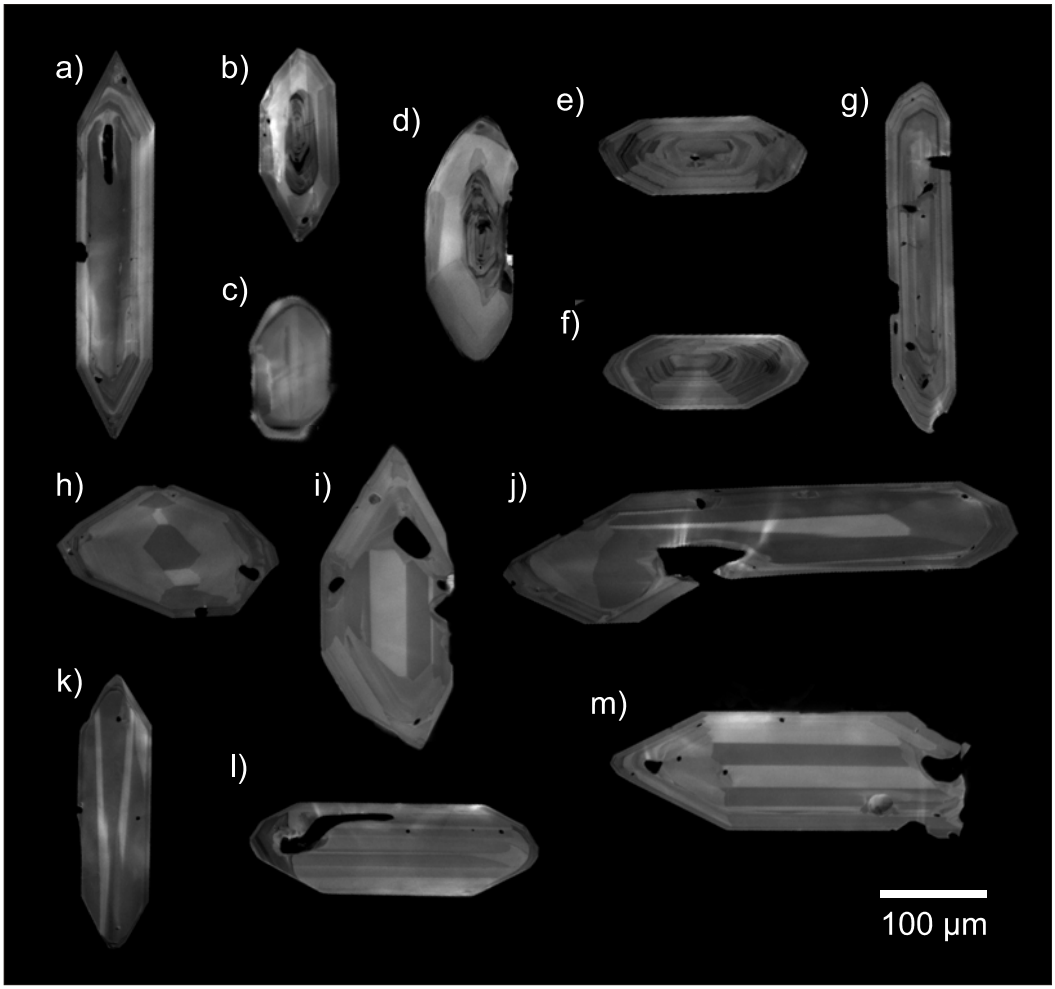

Figure 4. Representative cathodoluminescence images of zircon grains extracted from Swift Creek stage eruptive units. **(a–d)** Examples of grains that exhibit euhedral growth bands. **(e–g)** Examples of grains that exhibit oscillatory zoning. **(h–j)** Examples of grains that exhibit sector zoning. **(k–m)** Examples of grains that exhibit striped zoning. Note that many grains (most notably a, b, d, h, i, and m) exhibit two or more types of growth patterns and that many grains contain truncated growth bands and/or curved boundaries between adjacent zones. A small proportion of grains (b, c, and l) are also slightly rounded.

Whole-rock geochemistry of Swift Creek stage samples

We present the first compilation of whole-rock major and trace element geochemistry of Swift Creek stage eruptive units in Table 3. Major element Harker diagrams show typical trends, with increasing Na_2O and K_2O and decreasing FeO, MgO, CaO, Al_2O_3, and TiO_2 with increasing SiO_2 (Fig. 5). Like other eruptive stages of Mount St. Helens (e.g., Defant and Drummond, 1993; Smith and Leeman, 1987, 1993), Swift Creek stage eruptive units contain elevated Al_2O_3 contents in comparison to most arc dacites. Nevertheless, Swift Creek rocks have trace element signatures that are characteristic of most arcs (Fig. 6a); they contain relatively high concentrations of fluid

Table 3. Major and trace element geochemistry of Swift Creek stage samples

	SC08-1044	SHD08-2Z	SHD08-3Z	SHD08-4Z	SHD08-5Z	SHD08-8Z	SHD08-12Z	SHD08-13Z	SHD08-14Z	SHD08-15Z
Major elements (wt.%)										
SiO_2	65.85	60.75	66.13	64.99	64.96	64.65	66.24	64.72	66.75	65.50
Al_2O_3	16.13	17.90	17.44	17.07	17.22	17.25	17.20	17.25	16.71	16.78
Na_2O	4.29	4.54	4.55	4.54	4.53	4.45	4.60	4.54	4.61	4.48
K_2O	1.56	1.29	1.36	1.40	1.31	1.28	1.40	1.37	1.51	1.49
CaO	4.34	5.95	4.22	4.88	4.91	5.16	4.30	5.00	4.17	4.81
FeO	3.85	4.26	3.26	3.38	3.41	3.38	3.13	3.28	3.06	3.22
Fe_2O_3	1.07	1.18	0.91	0.94	0.95	0.94	0.87	0.91	0.85	0.89
MgO	1.96	3.03	1.40	1.92	1.85	2.01	1.50	2.07	1.53	2.09
TiO_2	0.757	0.849	0.557	0.641	0.598	0.621	0.560	0.638	0.572	0.629
P_2O_5	0.11	0.21	0.10	0.17	0.18	0.17	0.12	0.14	0.16	0.09
MnO	0.081	0.021	0.071	0.079	0.077	0.079	0.076	0.074	0.077	0.015
Zircon sat. temp. [a]	766	716	805	768	761	751	772	747	755	726
Trace elements (ppm)										
Ba	353	362	334	330	334	325	330	311	365	292
Cs	1.8	0.9	1.8	1.1	0.9	1.1	1.8	0.8	0.9	1.0
Pb	<5	<5	5	7	<5	<5	6	<5	7	5
Rb	40	20	40	41	36	31	38	29	33	28
Sr	493	826	489	532	522	519	501	579	489	606
Th	3.03	1.82	2.54	3.04	2.43	2.31	2.74	2.77	2.60	2.27
U	1.43	0.73	1.14	1.29	1.11	0.99	1.23	1.28	0.99	1.01
Hf	3.8	2.8	4.6	3.8	3.7	3.3	3.6	3.3	3.5	2.8
Nb	6.8	5.8	9.1	7.8	7.4	6.8	6.9	5.1	5.3	3.7
Sc	8.54	12.1	7.16	9.58	8.49	9.22	7.53	10.40	7.8	9.5
Ta	0.49	0.4	0.43	0.47	0.46	0.45	0.46	0.31	0.4	0.3
Zr	161	109	227	174	156	143	161	135	135	104
Co	12.4	19.0	9.2	12.3	12.2	12.0	9.5	13.2	8.0	10.0
Cr	19.8	39.0	17.3	16.6	16.0	36.5	12.9	20.9	19.0	23.0
Ni	16	32	8	14	17	18	8	16	11	16
V	88	122	57	79	74	79	56	97	62	96
Y	10	11	9	11	9	10	9	14	10	7
La	15.3	16.6	14.2	14.8	15.3	14.3	20.2	17.6	15.7	9.5
Ce	33.3	35.8	31.3	33.2	33.6	31.9	30.5	32.6	31.3	20
Pr	3.53	4.13	3.29	3.48	3.55	3.38	3.04	3.74	3.99	1.92
Nd	14.3	17	12.9	14.1	14.2	13.8	11.9	14.8	27	7.6
Sm	3.32	3.38	2.99	3.42	3.32	3.33	2.81	3.61	2.99	1.82
Eu	0.996	1.30	1.050	1.120	1.120	1.090	1.000	1.120	1.10	0.90

Table 3. (continued)

	SC08-1044	SHD08-2Z	SHD08-3Z	SHD08-4Z	SHD08-5Z	SHD08-8Z	SHD08-12Z	SHD08-13Z	SHD08-14Z	SHD08-15Z
Gd	2.61	3.01	2.37	2.78	2.70	2.57	2.17	3.11	2.56	1.74
Tb	0.37	0.42	0.34	0.41	0.38	0.36	0.33	0.45	0.38	0.25
Dy	2.10	2.25	2.00	2.34	2.08	2.11	1.93	2.57	2.19	1.40
Ho	0.41	0.43	0.39	0.46	0.40	0.39	0.38	0.51	0.43	0.27
Er	1.19	1.22	1.14	1.35	1.18	1.13	1.14	1.50	1.27	0.79
Tm	0.171	0.179	0.160	0.200	0.175	0.157	0.163	0.206	0.183	0.118
Yb	1.02	1.11	0.96	1.22	1.05	0.94	0.97	1.18	1.11	0.76
Lu	0.154	0.160	0.149	0.167	0.147	0.139	0.144	0.167	0.158	0.119

Major element values recalculated to 100% volatile free with $Fe_2O_3 = 0.2 \times Fe_2O_3(t)$ and $FeO = 0.8998 \times [Fe_2O_3(t) - Fe_2O_3]$. Recalculation followed the same protocol as Clynne et al. (2008) for direct comparison of results.
[a] Zircon saturation temperature (^oC) calculated from the equation of Watson and Harrison (1983).

mobile elements (e.g., Cs, U, Pb, Sr) and large ion lithophile elements (e.g., Rb, Ba, K) and relatively low concentrations of high field strength elements (e.g., Nb, Ta, Ti, Y, Lu). In addition, chondrite-normalized rare earth element (REE) patterns display enrichments in light rare earth elements (LREEs) relative to heavy rare earth elements (HREEs; Fig. 6b).

Zircon crystallization ages

S tephra

Results of all radiometric age determinations for Swift Creek stage samples are reported in Table A1. For a sample of Sg pumice (SHD08-12Z), 22 ^{238}U-^{230}Th analyses were performed on 15 zircon grains. Measured model ages range from 23–170 ka and no analyses are within error of the sample eruption age (~15.5 ka) or the equiline. While there is some disagreement between the probability density curve (PDC) peaks and the isochron and Unmix ages, the three techniques overall yield very similar results. The U-Th analyses fall onto three isochrons with approximate ages of 31 ± 2 ka, 68 ± 6 ka, and 156 ± 14 ka, the PDC displays a prominent peak at 29 ka and smaller peaks at 61, 79, and 154 ka, and the Isoplot Unmix algorithm identifies age populations of 31 ± 2, 66 ± 6, and 155 ± 15 ka (Fig. 7).

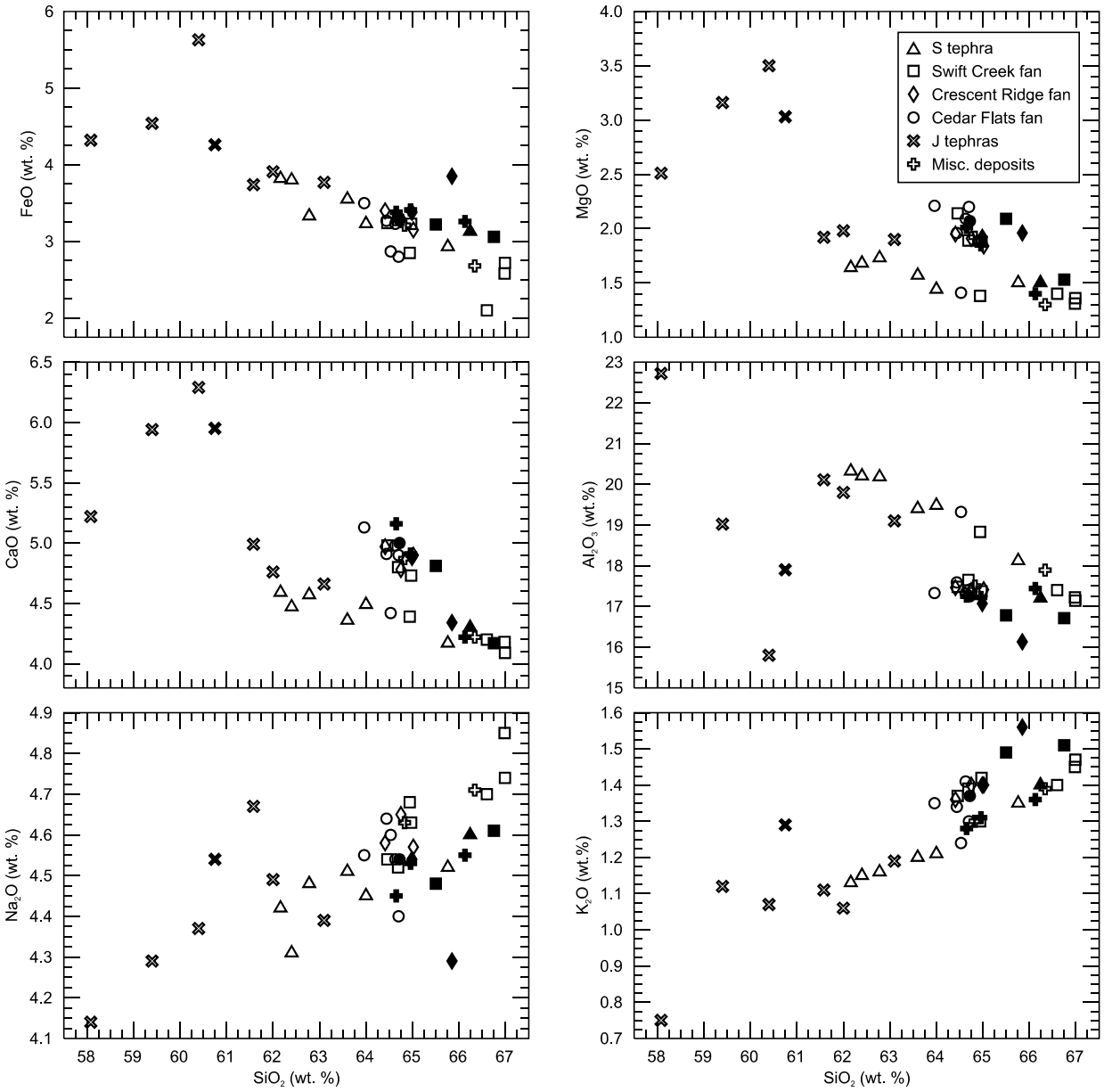

Figure 5. Selected major element oxides vs. silica diagrams for eruptive units of the Swift Creek stage. Samples include analyses performed as part of this study (represented by filled symbols), recent U.S. Geological Survey analyses (M.A. Clynne, unpublished data), and analyses compiled from the literature (Clynne et al., 2008; Crandell, 1987; Halliday et al., 1983; Mullineaux, 1996; Smith and Leeman, 1987). All analyses were recalculated to 100% volatile free following the procedure outlined in Table 3.

Swift Creek fan

We performed 22 U-Th measurements on 16 zircon grains from the lower portion of the Swift Creek fan (SHD08-14Z). Most of the model ages extend from 20–179 ka and are best characterized by three isochrons with approximate ages of 25 ± 3, 52 ± 4, and 153 ± 14 ka (Fig. 7). One spot with an undefined U-Th age and a spot near

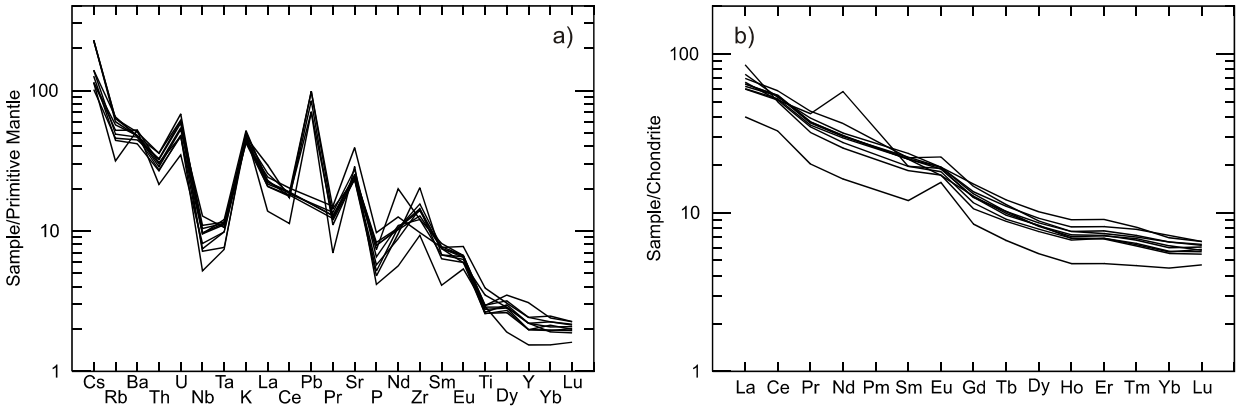

Figure 6. (a) Primitive-mantle normalized trace element plot and **(b)** chondrite-normalized rare earth element plot for eruptive units of the Swift Creek stage. Only analyses performed as part of this study are plotted. Normalizing values are from Sun and McDonough (1989).

the equiline with an age of 250^{+69}_{-42} ka yielded ^{238}U-^{206}Pb ages of 23.1 and 32.4 Ma, respectively, which correspond to the age of Tertiary Cascades arc rocks. One U-Th analysis with a geologically impossible age of 6 ka and one other analysis may be within error of the Swift Creek fan eruption age (final emplacement by ~15 ka). The isochron ages, PDC ages, and Unmix ages are, within error, nearly identical with the exception of one additional age population returned by the Unmix algorithm. The PDC exhibits prominent peaks at 27 and 47 ka and a smaller peak at 157 ka while the Unmix ages are 24 ± 3 ka, 51 ± 4 ka, 113 ± 40 ka, and 156 ± 20 ka (Fig. 7).

We also analyzed 18 spots on 12 grains from the upper portion of the Swift Creek fan (SHD08-15Z). The U-Th ages range from 16–270 ka and are best described by isochron ages of ~18 ± 5, 33 ± 6, 51 ± 6, and 176 ± 27 ka (Fig. 7). Three analytical spots have model ages within error of the timeframe of emplacement of the Swift Creek fan and one spot has an age within error of the equiline. Prominent peaks at 18, 34, and 49 ka and a minor peak at 158 ka are present in the PDC, and the Unmix function discerns age populations of 18 ± 5, 34 ± 8, and 49 ± 8 ka (Fig. 7). Unlike the other samples described thus far, the error ellipses of U-Th analyses assigned to different isochrons substantially overlap (Fig. 7), but most of the age populations identified by the isochron diagram, the PDC, and the Isoplot Unmix routine are identical within error, permitting confidence in the isochron ages. Note, however, that the Unmix algorithm does not discern the oldest age population identified by the isochron diagram and PDC. Hence, while the distribution of U-Th data points and the U-Th age histogram (Fig. 7) strongly suggest that many older ages exist, we cannot determine with certainty whether or not they represent a single, coherent population.

Figure 7. Probability density curves (left panels) and corresponding ($^{230}Th/^{232}Th$) vs. ($^{238}U/^{232}Th$) isochron diagrams (right panels) for U-Th age analyses of zircon grains extracted from Swift Creek stage eruptive units. All model ages were calculated as two-point isochrons between the zircon analysis and inferred melt values of ($^{230}Th/^{232}Th$) = ($^{238}U/^{232}Th$) = 1.2 (indicated with square symbols on the isochron diagrams). Error ellipses denote 1σ analytical uncertainties in ($^{230}Th/^{232}Th$) and ($^{238}U/^{232}Th$). Plotted isochrons represent the smallest number of viable age populations that accurately describe all or most of the data for each sample. Analyses that do not fall onto any isochron are delineated with an "x" and were thus not included in isochron statistics (i.e., MSWD and probability) calculations. Arrows indicate peaks and shoulders in the probability density curves. For presentation purposes, some analyses with high ($^{230}Th/^{232}Th$) and ($^{238}U/^{232}Th$) values have been excluded.

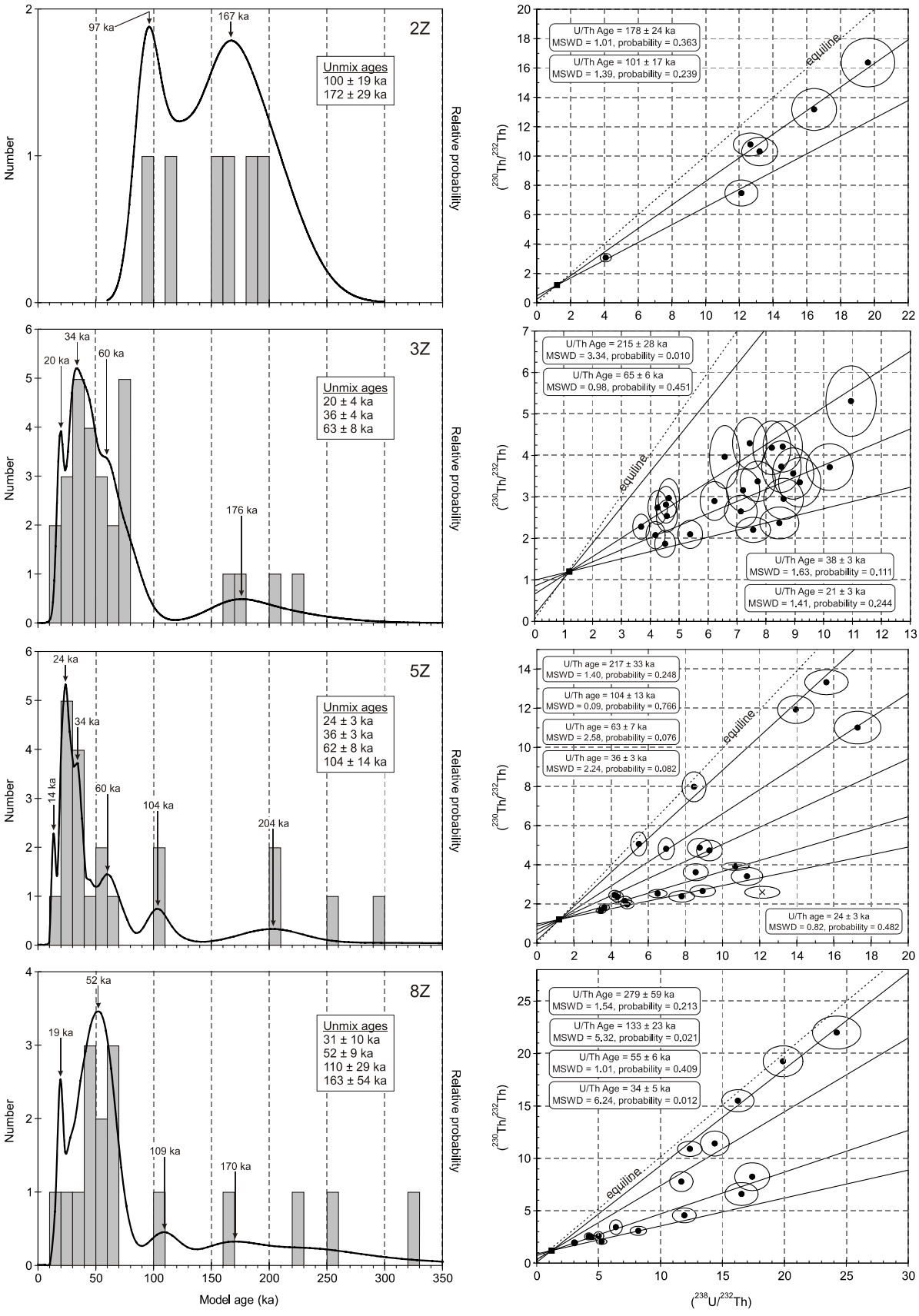
2Z
97 ka
167 ka
Unmix ages
100 ± 19 ka
172 ± 29 ka
U/Th Age = 178 ± 24 ka
MSWD = 1.01, probability = 0.363
U/Th Age = 101 ± 17 ka
MSWD = 1.39, probability = 0.239
equiline
3Z
20 ka
34 ka
60 ka
176 ka
Unmix ages
20 ± 4 ka
36 ± 4 ka
63 ± 8 ka
U/Th Age = 215 ± 28 ka
MSWD = 3.34, probability = 0.010
U/Th Age = 65 ± 6 ka
MSWD = 0.98, probability = 0.451
U/Th Age = 38 ± 3 ka
MSWD = 1.63, probability = 0.111
U/Th Age = 21 ± 3 ka
MSWD = 1.41, probability = 0.244
5Z
24 ka
34 ka
14 ka
60 ka
104 ka
204 ka
Unmix ages
24 ± 3 ka
36 ± 3 ka
62 ± 8 ka
104 ± 14 ka
U/Th age = 217 ± 33 ka
MSWD = 1.40, probability = 0.248
U/Th age = 104 ± 13 ka
MSWD = 0.09, probability = 0.766
U/Th age = 63 ± 7 ka
MSWD = 2.58, probability = 0.076
U/Th age = 36 ± 3 ka
MSWD = 2.24, probability = 0.082
U/Th age = 24 ± 3 ka
MSWD = 0.82, probability = 0.482
8Z
52 ka
19 ka
109 ka
170 ka
Unmix ages
31 ± 10 ka
52 ± 9 ka
110 ± 29 ka
163 ± 54 ka
U/Th Age = 279 ± 59 ka
MSWD = 1.54, probability = 0.213
U/Th Age = 133 ± 23 ka
MSWD = 5.32, probability = 0.021
U/Th Age = 55 ± 6 ka
MSWD = 1.01, probability = 0.409
U/Th Age = 34 ± 5 ka
MSWD = 6.24, probability = 0.012
Number
Relative probability
Model age (ka)
(230Th/232Th)
(238U/232Th)

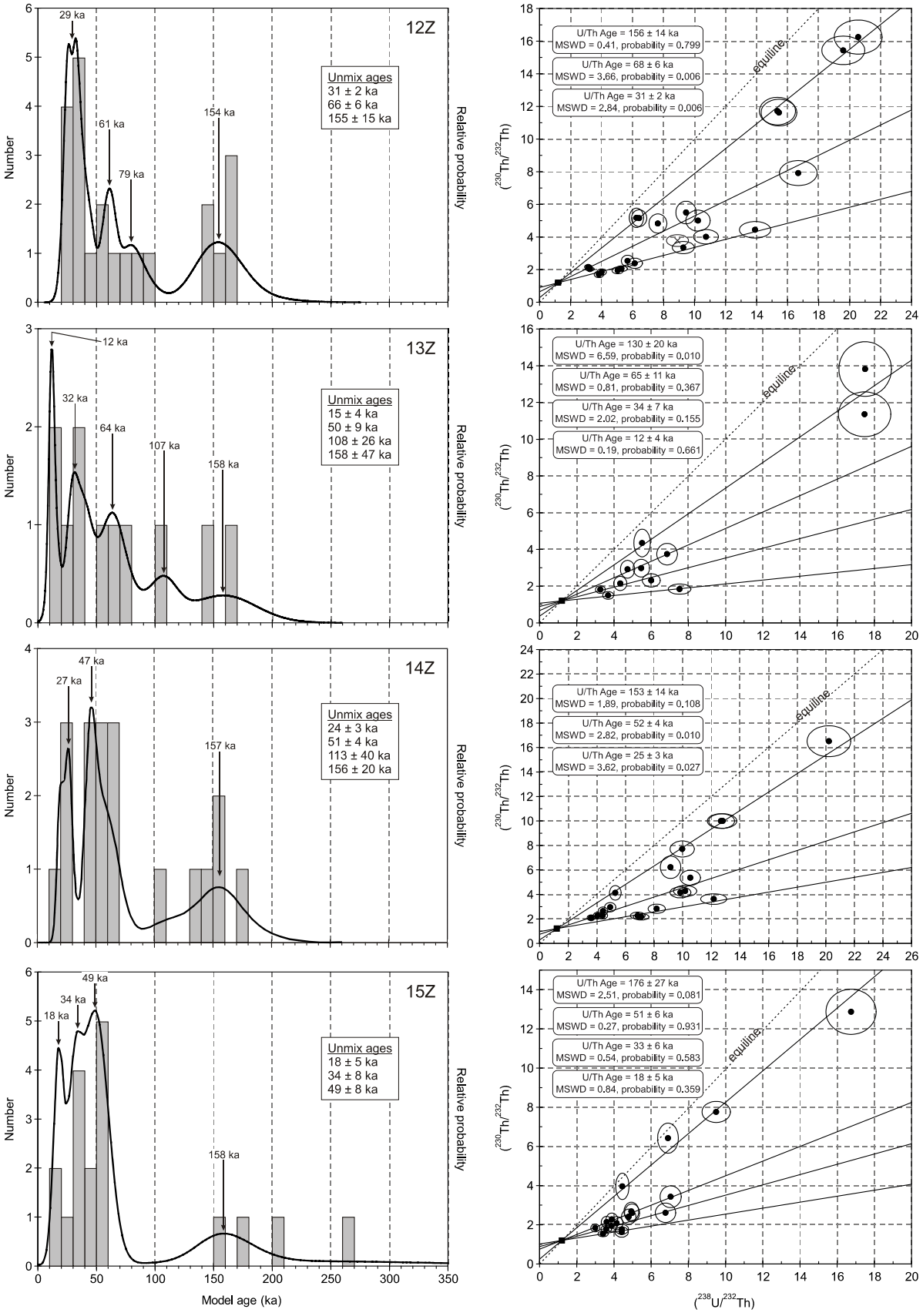
12Z
29 ka
61 ka
79 ka
154 ka
Unmix ages
31 ± 2 ka
66 ± 6 ka
155 ± 15 ka
U/Th Age = 156 ± 14 ka
MSWD = 0.41, probability = 0.799
U/Th Age = 68 ± 6 ka
MSWD = 3.66, probability = 0.006
U/Th Age = 31 ± 2 ka
MSWD = 2.84, probability = 0.006
13Z
12 ka
32 ka
64 ka
107 ka
158 ka
Unmix ages
15 ± 4 ka
50 ± 9 ka
108 ± 26 ka
158 ± 47 ka
U/Th Age = 130 ± 20 ka
MSWD = 6.59, probability = 0.010
U/Th Age = 65 ± 11 ka
MSWD = 0.81, probability = 0.367
U/Th Age = 34 ± 7 ka
MSWD = 2.02, probability = 0.155
U/Th Age = 12 ± 4 ka
MSWD = 0.19, probability = 0.661
14Z
27 ka
47 ka
157 ka
Unmix ages
24 ± 3 ka
51 ± 4 ka
113 ± 40 ka
156 ± 20 ka
U/Th Age = 153 ± 14 ka
MSWD = 1.89, probability = 0.108
U/Th Age = 52 ± 4 ka
MSWD = 2.82, probability = 0.010
U/Th Age = 25 ± 3 ka
MSWD = 3.62, probability = 0.027
15Z
18 ka
34 ka
49 ka
158 ka
Unmix ages
18 ± 5 ka
34 ± 8 ka
49 ± 8 ka
U/Th Age = 176 ± 27 ka
MSWD = 2.51, probability = 0.081
U/Th Age = 51 ± 6 ka
MSWD = 0.27, probability = 0.931
U/Th Age = 33 ± 6 ka
MSWD = 0.54, probability = 0.583
U/Th Age = 18 ± 5 ka
MSWD = 0.84, probability = 0.359
equiline
Number
Relative probability
Model age (ka)
(230Th/232Th)
(238U/232Th)

Cedar Flats fan

Eleven U-Th ages were measured on 8 zircon grains from a hypersthene-hornblende dacite of the Cedar Flats fan (SHD08-13Z). Two of the analyses are within error of the timeframe of fan emplacement (probably between 14 and 13 ka) and no analyses are within error of the equiline. Measured model ages vary from 12–162 ka and fall onto four isochrons with approximate ages of 12 ± 4, 34 ± 7, 65 ± 11, and 130 ± 20 ka (Fig. 7). The PDC similarly contains peaks at 12, 32, and 64 ka, but it also exhibits two peaks at 107 and 158 ka rather than one peak near 130 ka, and the Unmix algorithm yields age populations of 15 ± 4, 50 ± 9, 108 ± 26, and 158 ± 47 ka (Fig. 7). All three age determination methods confirm the existence of a population of analyses near the eruption age of the Cedar Flats fan, but the otherwise conflicting results preclude precise determination of the zircon crystallization ages within this sample.

J tephra

Six U-Th analyses were performed on four zircon grains from a sample of Jg pumice (SHD08-2Z). The crystallization ages range from 93–198 ka and are characterized by two isochron ages of ~101 ± 17 ka and 178 ± 24 ka (Fig. 7). None of the analyses are within error of the sample eruption age (~10.5–10 ka) or the equiline. Within error, the ages provided by the PDC and the Unmix function are identical to the isochron ages; the PDC exhibits two peaks at 97 and 167 ka while the Unmix algorithm identifies populations of 100 ± 19 and 172 ± 29 ka (Fig. 7).

Miscellaneous samples

We determined U-Th ages of 30 spots on 15 grains within pumice from a surge deposit erupted sometime prior to the emplacement of the set J tephras (SHD08-3Z). The model ages range from 19 ka to the equiline (i.e., ≥350 ka) and are best described by isochrons with ages of ~21 ± 3, 38 ± 3, 65 ± 6, and 215 ± 28 ka (Fig. 7). Two spots have crystallization ages that may be within error of the sample eruption age and one analysis falls on the equiline. Prominent peaks at 20, 34, and 60 ka and a minor peak at 176 ka are present on the PDC, and the Unmix routine gives ages of 20 ± 4, 36 ± 4, and 63 ± 8 ka (Fig. 7). As with sample SHD08-15Z, there is substantial overlap in the error ellipses of U-Th analyses assigned to different isochrons, but strong agreement between the three age determination techniques, with the exception of the oldest population, supports most of the isochron ages.

We performed 23 U-Th analyses on 17 grains from a lithic pyroclastic flow (SHD08-5Z) within the Timberline section (Fig. 1). The measured crystallization ages extend from 15–297 ka and are characterized by five isochrons with ages of ~24 ± 3, 36 ± 3, 63 ± 7, 104 ± 13, and 217 ± 33 ka (Fig. 7). One analysis on the equiline yielded a U-Pb age of 25.5 Ma. Two other analyses within error of the equiline yielded U-Pb ages (53 ± 307 and 214 ± 21 ka) similar to the corresponding U-Th ages (252^{+167}_{-63} and 297^{+250}_{-70} ka, respectively). One U-Th analysis with a geologically impossible age of 1 ka and two other model ages potentially fall within error of the sample eruption age (unknown). The PDC displays prominent peaks at 24 and 34 ka and smaller peaks at 14, 60, 104, and 204 ka, and the Unmix function distinguishes age populations of 24 ± 3, 36 ± 3, 62 ± 8, and 104 ± 14 ka (Fig. 7). Similar to several other samples, most of the isochron ages, PDC ages, and Unmix ages agree within error, but we cannot confidently discern whether or not the >200 ka analyses represent a coherent population.

Lastly, 17 U-Th age determinations were conducted on 10 zircon grains from an additional lithic pyroclastic flow within the Timberline section (SHD08-8Z). The mineralogy (Table 2) and geochemistry (Table 3) of this sample are very similar to those of SHD08-5Z, but the zircon grains are distinguishable by differences in morphology and zoning. The U-Th model ages range from 19 to ≥350 ka and fall onto four isochrons with approximate ages of 34 ± 5, 55 ± 6, 133 ± 23, and 279 ± 59 ka (Fig. 7). One analysis may be within error of the sample eruption age and two fall on or within error of the equiline. The isochron, PDC, and Unmix methods provide somewhat conflicting results; the PDC exhibits major peaks at 19 and 52 ka and minor peaks at 109 and 170 ka while Unmix yields ages of 31 ± 10, 52 ± 9, 110 ± 29, and 163 ± 54 ka (Fig. 7).

All Swift Creek stage samples

In total, 149 spots on 97 zircon grains were analyzed for U-Th crystallization ages. The vast majority of the measured model ages range from tens to hundreds of thousands of year before eruption, and only a small portion (<10%) fall within error of sample eruption ages. However, zircon rims were often too narrow for analysis and analyses of zircon surfaces might reveal more crystallization ages within error of eruption. Taken as a whole, the Swift Creek zircon crystallization ages are best characterized by seven isochrons with ages of ~16 ± 2, 26 ± 1, 39 ± 2, 62 ± 3, 103 ± 8, 168 ± 8, and 280 ± 42 ka. The PDC contains predominant peaks or shoulders at 32, 44, and 60 ka and smaller peaks at 102 and 157 ka while the Unmix algorithm discerns age populations of 21 ± 2, 37 ± 3, 61 ± 5, 100 ± 11, and 162 ± 10 (Fig. 8). Based on similarities between the isochron ages, PDC peaks, and Unmix ages, we

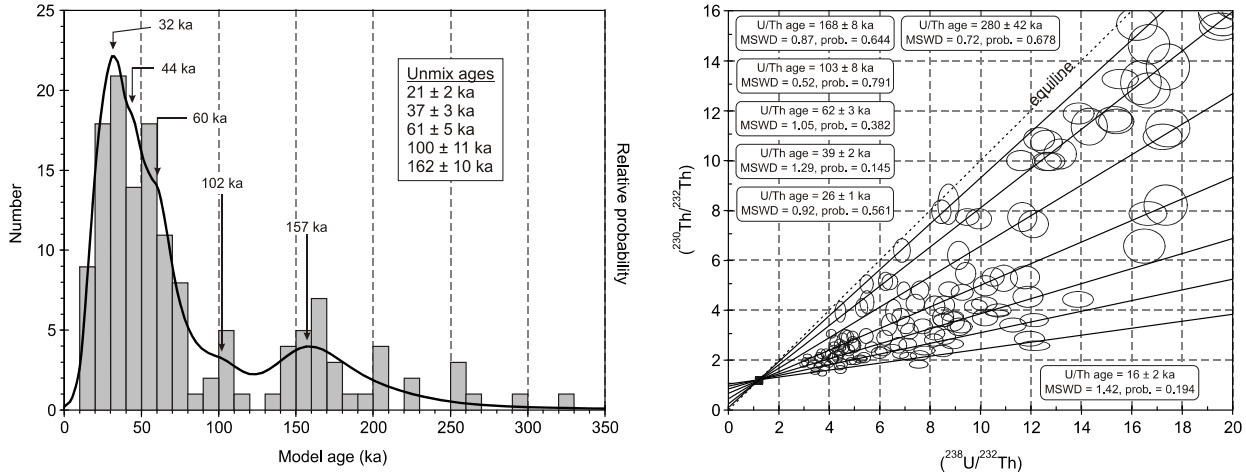

Figure 8. Probability density curve and isochron diagram for all U-Th age analyses of zircon grains within Swift Creek stage rocks.

argue that episodes of Swift Creek zircon crystallization occurred at ~20–30, 40, 60, 100, and 160 ka. While there are clearly a significant number of analyses with U-Th ages <20 ka and >160 ka (Fig. 8), disagreements between the three age determination methods suggest that they do not represent single, coherent populations. It is also important to note that many of the oldest analyses fall on or within error of the equiline and were not reanalyzed by U-Pb, meaning that they may actually be >350 ka.

Zircon trace element geochemistry

Hf, U, Th, Ti, and $T_{Ti\text{-}in\text{-}zirc}$

Trace element compositions of 174 spots on 81 zircon grains are provided in Table A2. In the discussion that follows, we refer to the innermost identifiable zones of zircon grains as centers, zones on the edge of a grain (including rims that clearly surround all other zones) are termed edges, and interior refers to either a zone between a center and an edge or a zone that is not definitively a center or an edge. Zircons from Swift Creek rocks have Hf concentrations ranging from 6600–13300 ppm. Grain centers and interiors have lower minimum Hf concentrations (7300 and 6300 ppm, respectively) than grain edges (8100 ppm) and edges extend up to a higher maximum concentration (13300 ppm) than centers and interiors (~12500 ppm), but all spot locations otherwise show very similar ranges in Hf content (Fig. 9). Likewise, most of the individual samples span Hf values that strongly overlap with the range of all samples, except for SHD08-13Z, which only extends up to 11000 ppm, and SHD08-14Z, which

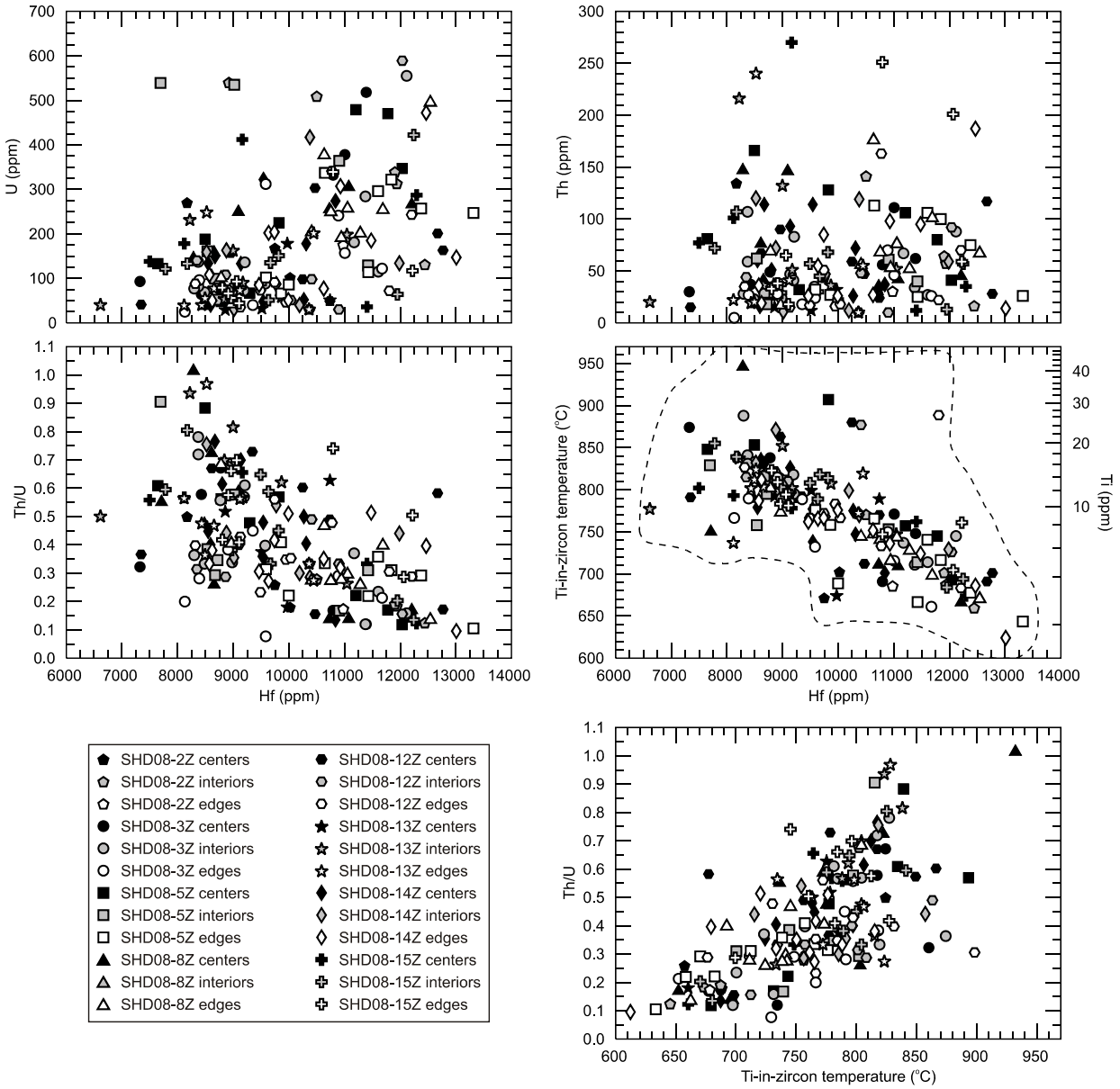

Figure 9. Geochemical variation diagrams for Hf, Th, U, Ti, and estimated zircon crystallization temperature of zircon grains from Swift Creek stage rocks. Trace element analyses are grouped according to sample and spot location; each shape corresponds to a different eruptive unit while symbol shading denotes the region of the zircon grain on which the analysis was performed (black = grain centers, gray = grain interiors, and white = grain edges and rims). The dashed line in the Ti-in-zircon temperature vs. Hf plot delineates the potential error in calculated zircon crystallization temperatures due to variations in the activity of TiO_2 between 0.5 and 0.9.

only ranges down to 8500 ppm. Uranium concentrations generally increase with increasing Hf, Th shows no correlation with Hf, and Th/U, Ti, and estimated crystallization temperature ($T_{Ti\text{-}in\text{-}zirc}$) decrease with increasing Hf concentration (Fig. 9).

Uranium contents of Swift Creek zircons extend from 25 to 950 ppm, yet all but three analyses yielded concentrations <700 ppm and the majority of spots (~70%) contain <200 ppm. Thorium concentrations span 5–550 ppm, but most spots (~80%) have <100 ppm and only five spots have >300 ppm. With the exception of outlier points (U >700 ppm and Th <300 ppm), all spot locations and most individual samples display very similar ranges in U, Th, and Th/U. Note, however, that sample SHD08-13Z exhibits a much lower maximum U concentration (250 ppm) than any other sample and that samples SHD08-13Z and -15Z have higher maximum values of Th (240 and 270 ppm, respectively) than any other sample (Fig. 9).

Titanium concentrations vary from 2 to 41 ppm and zircon crystallization temperatures calculated using the Ti-in-zircon thermometer range from 625–945 ^{o}C. Average uncertainties in the calculated temperatures due to variations in α_{TiO_2} between 0.5 and 0.9 are –25 ^{o}C and +35 ^{o}C (Fig. 9). Ranging α_{SiO_2} down to 0.7 induces an average additional uncertainty of 33^{o} into the minimum calculated temperatures but does not affect maximum temperatures. Zircon centers and interiors extend up to higher Ti values (41 and 26 ppm, respectively), and thus higher $T_{Ti\text{-}in\text{-}zirc}$ (945 and 890 ^{o}C), than zircon edges (18 ppm Ti and 845 ^{o}C), but all spot locations otherwise exhibit very similar ranges. All Swift Creek samples also nearly completely overlap in both Ti concentration and estimated crystallization temperature. Neither U nor Th exhibits a strong correlation with crystallization temperature, but Th/U systematically increases with increasing temperature (Fig. 9).

As shown above, there are no major geochemical distinctions among trace element analyses from different samples and spot locations. Significant differences do emerge, however, when the data are grouped according to crystallization age. For the remainder of this paper, we refer to analytical spots with ages corresponding to the "all Swift Creek" isochron ages of 16, 26, 39, and 62 ka (see Fig. 8) as the younger crystallization age populations while analyses corresponding to the isochron ages of 103, 168, and 280 ka are termed older crystallization age populations. Although there is a strong degree of overlap in the range of Hf values of these two groups, ~70% of the older analytical spots contain Hf concentrations >10000 ppm while ~75% of the younger spots have <10000 ppm Hf (Fig. 10). The younger age populations also extend down to lower Hf concentrations than the older populations (7200 ppm vs. 8100 ppm). Likewise, ~70% of the older analyses exhibit $T_{Ti\text{-}in\text{-}zirc}$ below 775 ^{o}C while ~70% of the younger analyses exhibit $T_{Ti\text{-}in\text{-}zirc}$ above 775 ^{o}C, and the older age populations have lower minimum and maximum estimated crystallization temperatures (660 and 880 ^{o}C) than the younger populations (690 and 945 ^{o}C). While both groups span similar Th values, about 65% of the older zircon growth zones contain >200 ppm U and ~80% have

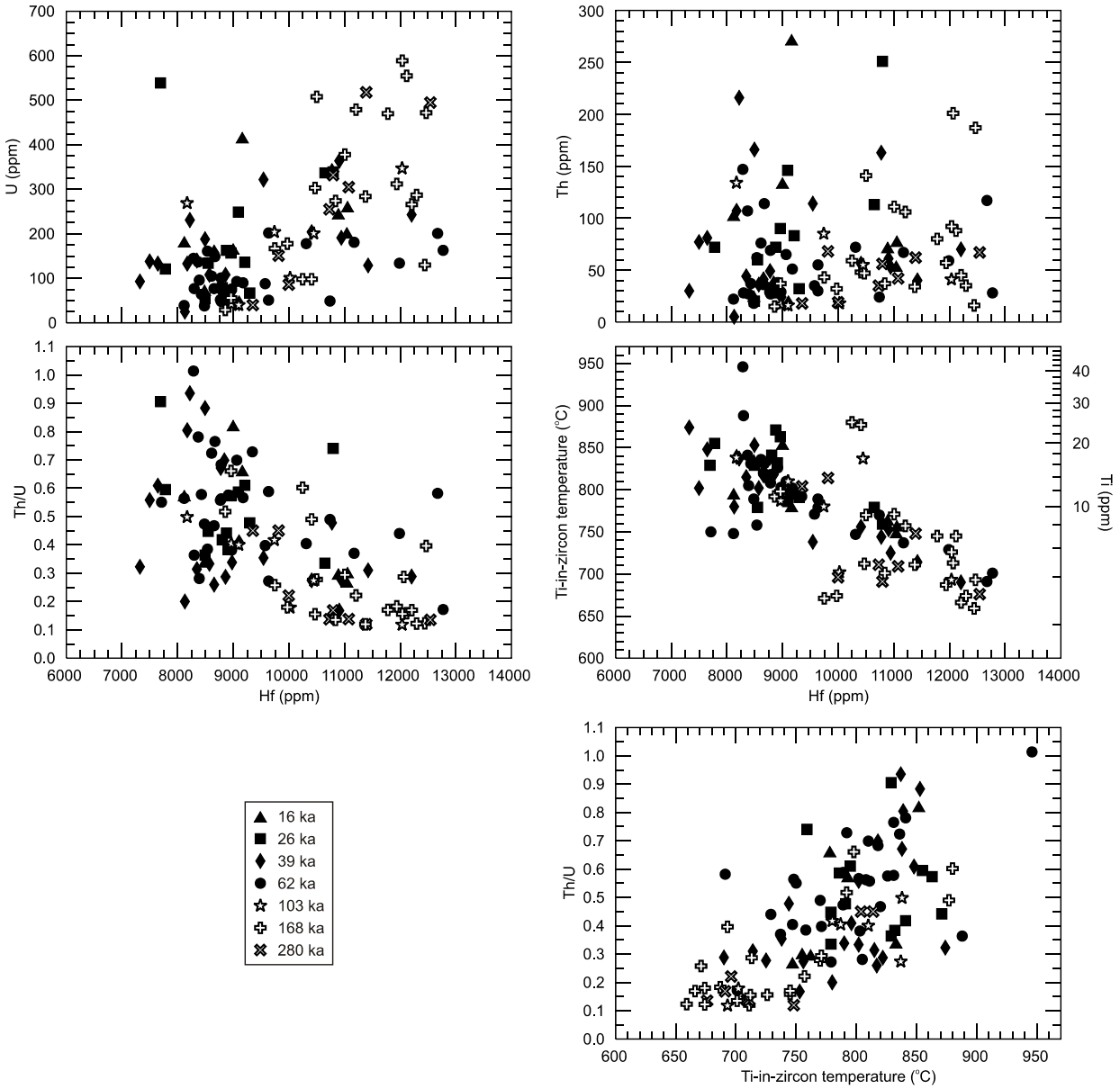

Figure 10. Geochemical variation diagrams for Hf, Th, U, Ti, and estimated zircon crystallization temperature of zircon grains from Swift Creek stage rocks. Trace element analyses are grouped according to age population (the given ages correspond to the isochron ages for all Swift Creek zircon analyses as a whole; see Fig. 8 and Table A1). Each shape corresponds to a different population, with black symbols denoting younger analyses and white symbols denoting older analyses.

Th/U <0.4. In contrast, ~75% of younger analytical spots have <200 ppm U and ~60% exhibit Th/U >0.4. The younger analyses also vary up to higher Th/U than the older populations (1.0 vs. 0.7; Fig. 10).

Rare earth elements

Zircons from Swift Creek stage eruptive units are strongly enriched in HREEs relative to LREEs on chondrite-normalized REE diagrams and have positive Ce anomalies (Fig. 11), features that are characteristic of natural magmatic zircons (e.g., Hoskin and Schaltegger, 2003). Most analytical spots also exhibit slight negative Eu anomalies (~80% of analyses range from Eu/Eu* = 0.5–0.8), but deep Eu anomalies are rare. Enrichment in the HREEs relative to the LREEs as indicated by chondrite-normalized ratios of Yb/Nd [$(Yb/Nd)_N$] generally increases with increasing Hf (Fig. 12) and decreases with increasing crystallization temperature. Enrichment in the middle rare earth elements (MREEs) relative to the LREEs as indicated by $(Gd/Nd)_N$ slightly increases with increasing Hf and decreases with increasing temperature. Lastly, HREE enrichment relative to the MREEs as indicated by $(Yb/Gd)_N$ weakly increases with increasing Hf and decreases with increasing temperature. Ratios of $(Yb/Nd)_N$, $(Gd/Nd)_N$, and $(Yb/Gd)_N$ all fall with increasing Th/U (Fig. 12). Similar to most other elemental signatures, there are slight differences in the ranges of $(Yb/Nd)_N$, $(Gd/Nd)_N$, and $(Yb/Gd)_N$ among different eruptive units and spot locations, but centers, interiors, edges, and all individual samples for the most part span very similar values. In contrast, most (~70%) older analytical spots contain $(Yb/Nd)_N$ >1000 while most (~65%) younger analytical spots have $(Yb/Nd)_N$ <1000, ~70% of older analyses exhibit $(Gd/Nd)_N$ >60 while ~65% of younger analyses fall below 60, and ~60% of older growth zones plot above $(Yb/Gd)_N$ = 20 while ~80% of younger domains have $(Yb/Gd)_N$ <20 (Fig. 12). The magnitude of the Eu anomaly (Eu/Eu*) does not correlate with Hf concentration, $T_{Ti\text{-}in\text{-}zirc}$, or Th/U, but the Ce anomaly (Ce/Ce*) roughly increases with increasing Hf and falls with rising crystallization temperature and Th/U (Fig. 13). The ranges of Eu/Eu* and Ce/Ce* of different samples and spot locations strongly overlap, and there are also no major distinctions in the Eu anomalies of different crystallization age populations. However, ~75% of the older analyses exhibit elevated Ce/Ce* (>100) while ~ 65% of the younger analyses have Ce/Ce* <100 (Fig. 13).

Chondrite-normalized concentrations of Nd (Nd_N) vary from 0.03–35, although only five analyses plot above 10 (Fig. 14). Not including these outliers, center and interior analytical spots extend up to higher Nd_N (~9) than edge analyses (6), but all spot locations otherwise span very similar Nd_N contents. The ranges in Nd_N of all of the individual samples almost entirely overlap. Among other LREEs, chondrite-normalized Ce concentrations of Swift Creek zircons span 4–150 while La_N varies from 0–3. Due to their typically low concentrations in natural zircons, La and Nd concentrations can be heavily skewed by small LREE-rich melt and mineral inclusions (such as apatite, which is ubiquitous in Swift Creek stage rocks). However, our zircon analyses do not appear to have been

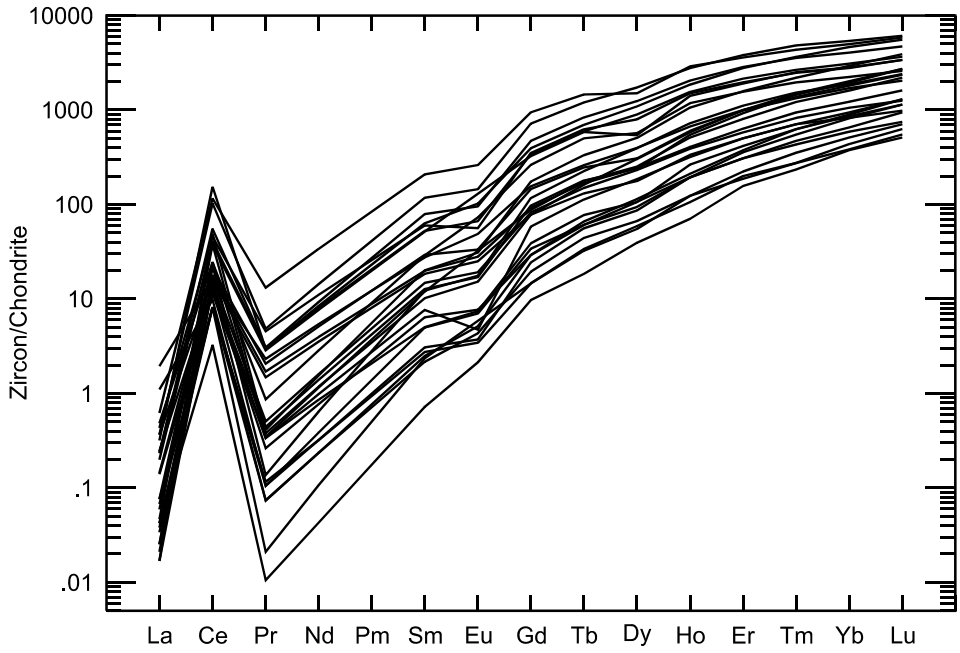

Figure 11. Chondrite-normalized rare earth element plot showing selected analyses that are representative of the composition of zircon grains extracted from eruptive units of the Swift Creek stage.

affected by inclusions, as none of them exhibit anomalously high La_N or Nd_N. Chondrite-normalized concentrations of Gd (representative of the MREEs) extend from 10 to 940 and primarily fall below 400 while values of Lu_N (representative of the HREEs) range from 420–6100 (Fig. 14). Similar to Nd_N, zircon centers and interiors have higher maximum Gd_N (~500) and Lu_N (6000) than zircon edges (most analyses plot at or below Gd_N = 150 and Lu_N = 3000). While there are differences in the span of Gd_N and Lu_N values exhibited by Swift Creek eruptive units, all samples overall have very similar concentrations. In contrast, ~80% of older analytical spots have Nd_N <2 and ~75% have Gd_N <100, although the Gd_N and Nd_N contents of the younger spots are fairly evenly distributed and both groups of age populations have similar Lu_N values. Chondrite-normalized concentrations of Nd and Gd sharply decrease with increasing Hf below 10000 ppm and level off above 10000 ppm (Fig. 14). Chondrite-normalized concentrations of Lu also decrease with increasing Hf, although the correlation is much weaker. Similarly, Nd_N and Gd_N values remain relatively uniform below 750 ^oC and sharply increase with increasing $T_{Ti\text{-}in\text{-}zirc}$ above 750 ^oC while Lu_N shows a weak trend of increasing concentration with increasing $T_{Ti\text{-}in\text{-}zirc}$. With increasing Th/U, chondrite-normalized concentrations of all REEs systematically increase (Fig. 14).

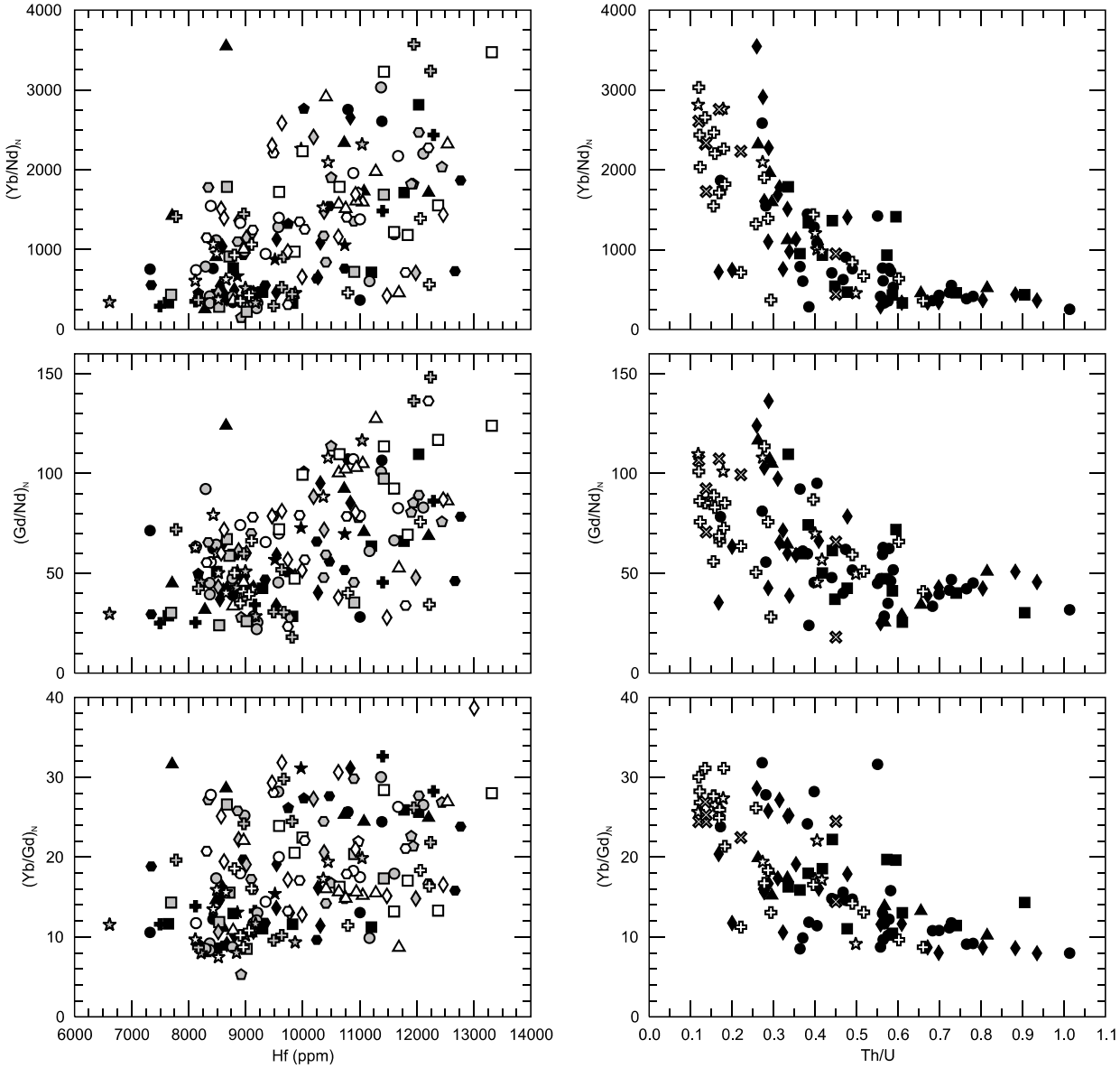

Figure 12. Variation of rare earth element ratios with Hf and Th/U of Swift Creek zircons. Analyses plotted in the left panels are grouped according to sample and spot location while analyses plotted in the right panels are grouped according to age. See Figs. 9 and 10 for symbol legend.

Inter- and intra-grain variability of zircon trace element composition

While zircon grains from different Swift Creek stage eruptive units typically exhibit nearly identical geochemical characteristics, there are dramatic differences in trace element geochemistry between and within grains. Among zircons from a particular sample, some individual grains encompass restricted ranges of Hf, $T_{Ti\text{-}in\text{-}zirc}$, Th/U, and Yb/Nd while others span the compositional range of all analyzed Swift Creek stage zircons. A small portion of grains display systematic trends in trace element contents from center to edge, but fluctuations in trace element

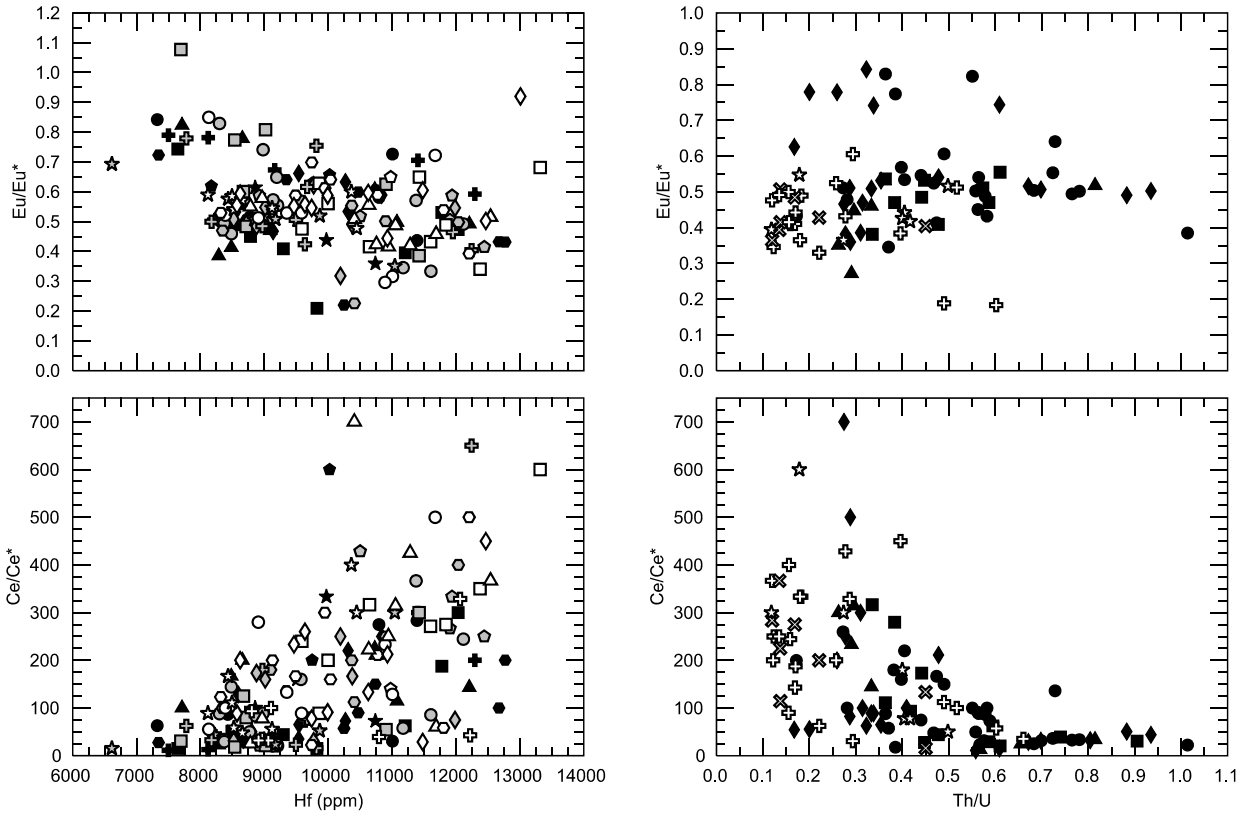

Figure 13. Variation of Eu and Ce anomalies with Hf and Th/U of zircon grains within Swift Creek stage eruptive units. Analyses plotted in the left panels are grouped according to sample and spot location while analyses plotted in the right panels are grouped according to age. See Figs. 9 and 10 for symbol legend.

signatures are more common (Fig. 15). These variations occur over periods of 10^3–10^4 years and often, but not universally, correspond to distinct zones visible in CL images. The pattern of fluctuation varies markedly from grain-to-grain, even within zircons from the same sample, although similar patterns recur among grains from all samples. As observed in the entire suite of trace element analyses, increases in Hf generally correspond to decreases in estimated crystallization temperature, decreases in Th/U, and increases in Yb/Nd (Fig. 15).

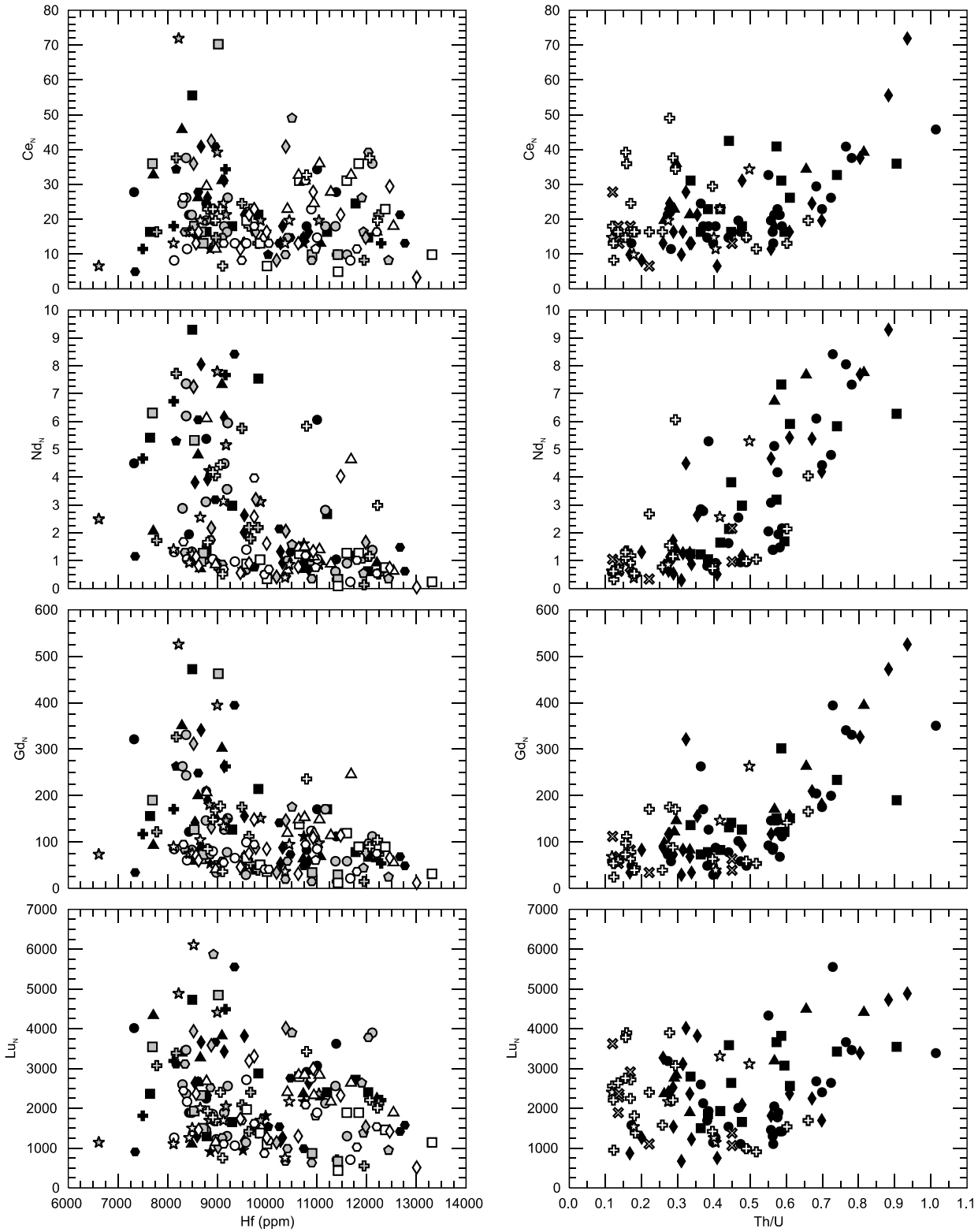

Figure 14. Variation of chondrite-normalized rare earth element concentrations with Hf and Th/U of zircons extracted from Swift Creek stage rocks. Analyses plotted in the left panels are grouped according to sample and spot location while analyses plotted in the right panels are grouped according to age. See Figs. 9 and 10 for symbol legend.

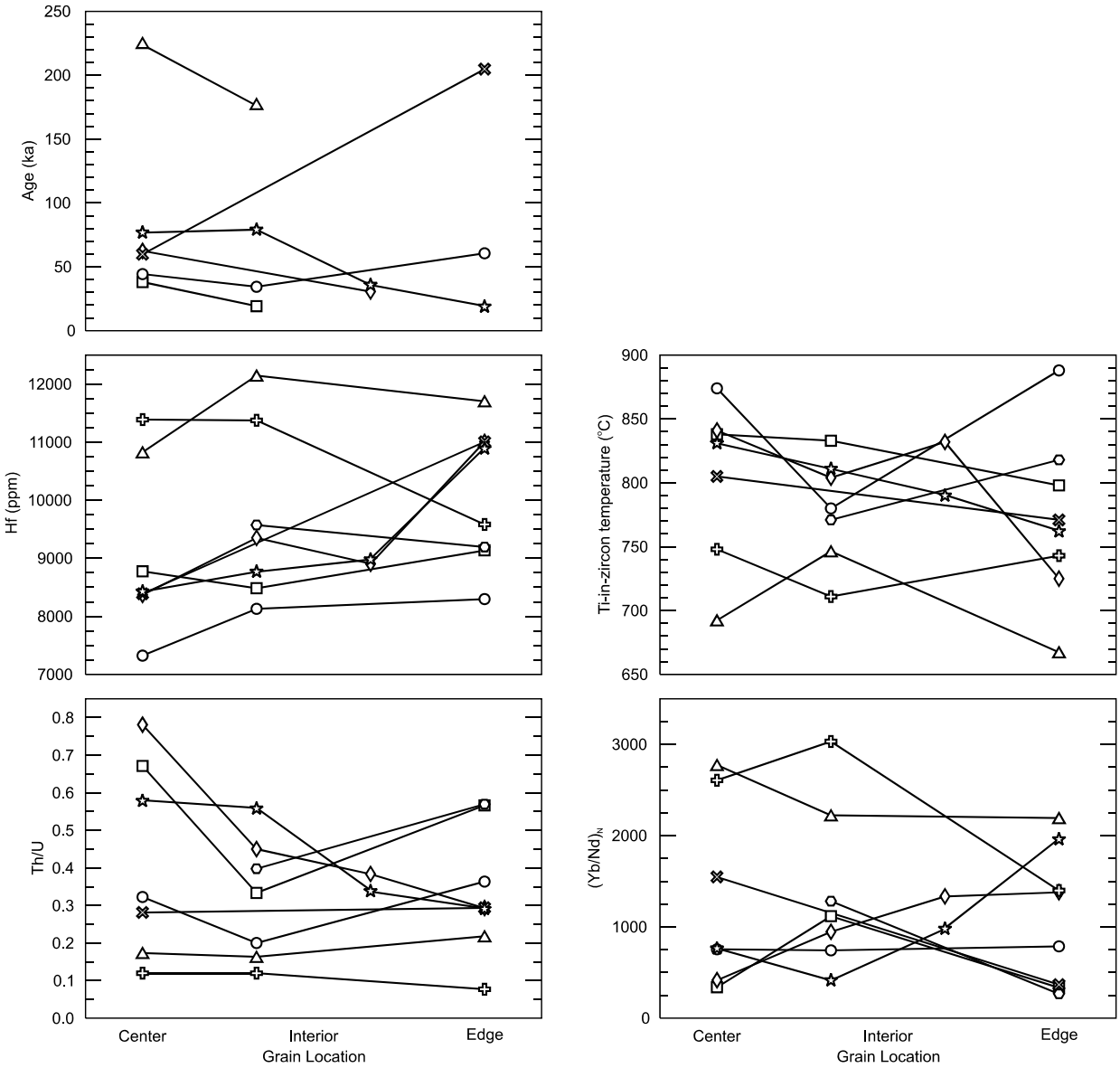

Figure 15. Intra-grain variability in crystallization age, Hf, Ti-in-zircon temperature, Th/U, and chondrite-normalized Yb/Nd for zircons from sample SHD08-3Z. Each symbol represents a single grain.

CHAPTER V

DISCUSSION

Reliability of calculated Ti-in-zircon temperatures

Many previous applications of the Ti-in-zircon thermometer have assumed that α_{SiO_2} and $\alpha_{TiO_2} = 1$. This approach has been criticized (e.g., Fu et al., 2008), given that inappropriate assignment of activity values can potentially induce substantial error (>100 ^{o}C in extreme cases) in calculated temperatures. For this study, we utilized matrix glass analyses to constrain characteristic α_{TiO_2} values of Mount St. Helens melts and we also evaluated potential error in our calculated temperatures due to uncertainty in SiO_2 and TiO_2 activities (see section entitled "Ti-in-zircon thermometer" in Chap. 3). All of our estimated crystallization temperatures (625–945 ^{o}C) are reasonable for zircon growth in silicic and intermediate melts. Moreover, the activities of SiO_2 and TiO_2 likely vary together during magmatic evolution (mafic melts tend to have lower α_{TiO_2} than felsic melts: Hayden and Watson, 2007), and the effects of under- or overestimating both α_{SiO_2} and α_{TiO_2} offset one another (Ferry and Watson, 2007). Accordingly, variations in our calculated zircon crystallization temperatures are useful even if the exact temperature values are not correct.

Other potential problems associated with use of the Ti-in-zircon thermometer include pressure dependence of Ti uptake into zircon, resetting of Ti concentration by subsolidus alteration or diffusion, disequilibrium crystallization, deviations from Henry's Law, and uncertainty in calibration of the thermometer (Fu et al., 2008). Thermodynamic calculations suggest that pressures that deviate a great deal from 2 GPa, at which the thermometer was calibrated, could introduce errors in Ti-in-zircon temperature estimates – underestimates would result at higher pressure and overestimates would occur at lower pressure (Ferriss et al., 2008; Ferry and Watson, 2007). Zircon presumably grows beneath Mount St. Helens at a pressure below 2 GPa, meaning that calculated temperatures may be somewhat too high, but any errors would be modest and systematic. In addition, experimental measurements suggest that diffusive transport of Ti ions in zircon is limited to ~5 μm in 10 G.y.; this diffusivity is much lower than values measured for Pb and the REEs, implying that determinations of Ti concentration in zircon are more robust than U-Pb age analyses (Cherniak and Watson, 2007). Other proposed complicating factors pertaining to use of the thermometer also apparently do not produce substantial error, as temperatures recorded in zircons from the Spirit

Mountain batholith (Claiborne et al., in revision) are entirely consistent with magmatic conditions extensively documented by field, geochemical, and petrologic methods (Walker et al., 2007). Lastly, the recently developed NanoSIMS imaging technique reveals variations in zircon trace element composition on a sub-micron scale and documents regions of high Ti within natural and synthetic zircon grains (Hofmann et al., 2009). These high Ti "hot spots" are sometimes difficult to detect with standard CL and back-scattered electron imaging and could potentially raise the apparent temperature of a conventional ion microprobe analytical spot by tens of degrees. However, we took great care to avoid inclusions during analysis, and even if some of our analytical areas contain Ti "hot spots" that were not visible in images, we are confident that we have performed enough trace element analyses (174) to ensure that our overall results and conclusions are valid.

Interpretation of trace element signatures

Zircon is the dominant reservoir of Zr and Hf in the Earth's crust and preferentially incorporates Zr over Hf (Bea et al., 2006). As a result, zircon crystallization and separation from bulk magma causes progressive enrichment in Hf relative to Zr in the remaining melt. Low whole-rock and glass values of Zr/Hf are thus a unique indicator of zircon fractionation, and zircon grains that grow from highly differentiated melt contain abundant Hf (Lowery Claiborne et al., 2006). Correlations with Hf and $T_{Ti\text{-}in\text{-}zirc}$ imply that Yb/Nd and Th/U also serve as useful fractionation indicators. As previously described, Yb/Nd of Swift Creek zircons rises with increasing Hf concentration and decreasing $T_{Ti\text{-}in\text{-}zirc}$ while Th/U decreases with increasing Hf and decreasing temperature, suggesting that high values of Yb/Nd and low values of Th/U fingerprint fractionated melts.

Increasing Yb/Nd with increasing differentiation (reflected by rising Hf and falling estimated temperature) in Swift Creek stage zircons is not likely a result of fractionation of either plagioclase or amphibole, the two most abundant major phases in Mount St. Helens rocks. Crystallization of plagioclase cannot substantially affect the relative concentrations of the REEs because most rare earths, with the exception of Eu, are incompatible in plagioclase (e.g., Bachmann et al., 2005). While Yb and Nd are compatible in amphibole, amphibole exhibits similar partition coefficients for both elements in silicic melts (e.g., Bacon and Druitt, 1988; Sisson, 1994). Moreover, if amphibole fractionation were primarily responsible for changes in the slope of Swift Creek zircon REE patterns, then Yb/Nd would decrease with progressive differentiation. Crystallization of zircon also cannot be the primary mechanism for changes in Yb/Nd because although zircon contains high concentrations of the REEs, it displays a

strong preference for the HREEs over the LREEs (e.g., Fig. 11), meaning that zircon crystallization causes progressive enrichment of Nd relative to Yb in coexisting melt. The observed Yb/Nd trend thus requires co-crystallization of zircon with a LREE-rich mineral phase or phases, such as apatite, monazite, sphene, allanite, and/or chevkinite in order to lower Nd with progressive fractionation. Out of these phases, only apatite has been observed in Mount St. Helens rocks. Apatite incorporates LREEs much more favorably than zircon (e.g., Kd_{Nd}^{zircon} = 1.4–4.8 while $Kd_{Nd}^{apatite}$ = 33–61: Fujimaki, 1986) and is much more abundant than zircon in Swift Creek stage eruptive units. As a result, crystallization of a typical Mount St. Helens dacite may yield faster decreases in LREEs than HREEs, leading to higher Yb/Nd values for more evolved melts. Co-crystallization of apatite and zircon could also potentially explain the observed trend of increasing Yb/Gd with increasing fractionation because most MREEs are also more compatible in apatite than in zircon (e.g., Kd_{Gd}^{zircon} = 6.0–6.8 and $Kd_{Gd}^{apatite}$ = 44–96: Fujimaki, 1986). However, co-crystallization of zircon and apatite does not account for increasing Gd/Nd with increasing differentiation, and in order for Nd to have a bulk partition coefficient >1, apatite would have to make up ~1.5–3% of the crystallizing assemblage. It is also possible that apatite may not have crystallized with zircon, as Swift Creek stage zircon grains likely did not grow within their host magmas (see below). A more plausible explanation for the observed geochemical trends is that zircon also crystallized with another LREE- and MREE-rich accessory mineral(s) in the source region that was not incorporated into the final host magmas.

The Ce and Eu anomalies of magmatic zircons are related to the ratios of Ce^{4+}/Ce^{3+} and Eu^{3+}/Eu^{2+} in the zircon host melt, and they may therefore be controlled by oxygen fugacity (e.g., Bolhar et al., 2008; Hoskin and Schaltegger, 2003). However, we argue that melt fractionation also controls the magnitude of the anomalies. We have shown above that Ce/Ce* correlates with degree of melt evolution, with higher values at elevated Hf and low $T_{Ti\text{-}in\text{-}zirc}$ values. Zircons within the Spirit Mountain batholith show this same trend as well as decreasing Eu/Eu* with increasing fractionation (Claiborne et al., in revision; Lowery Claiborne et al., 2006). As before, evolution of the Ce anomaly is likely controlled by fractionation of apatite, monazite, sphene, allanite, and/or chevkinite. While zircon strongly prefers Ce^{4+} over Ce^{3+}, trivalent LREEs are typically more compatible in other accessory phases. The absence of any discernible trend in the magnitude of the Eu anomaly with melt evolution in Swift Creek stage zircons is best explained by co-crystallization of plagioclase and amphibole, which have opposite effects on Eu concentrations in coexisting melt.

Decreasing Th/U with increasing fractionation in Swift Creek stage zircons appears to be related to U concentration; analytical spots exhibit high U values at elevated Hf and low $T_{Ti\text{-}in\text{-}zirc}$ while Th remains uniform across the range of Hf and estimated temperature values. Similar to the REE patterns, co-crystallization of zircon with a Th-rich accessory mineral could cause the observed changes in Th/U by removing Th from the melt faster than U. However, increases in the concentrations of U and Th with melt evolution suggest that both elements were incompatible with the crystallizing mineral assemblage, an observation that is inconsistent with co-crystallization of zircon and other accessory minerals. Although the underlying cause of these trends is unclear, similar signatures have been observed in zircons from the Spirit Mountain batholith in southern Nevada (Claiborne et al., in revision; Lowery Claiborne et al., 2006) and the Separation Point Suite in New Zealand (Bolhar et al., 2008).

Construction and evolution of the Mount St. Helens magmatic system

Zircon was generally an undersaturated phase in erupted Swift Creek magmas. Zircon saturation temperatures (Watson and Harrison, 1983) calculated from whole-rock compositions of Swift Creek stage samples range from ~720–800 ^{o}C (Table 3) while eruption and pre-eruptive storage temperatures of Mount St. Helens dacites are typically ≥850 ^{o}C, although lower temperatures have been documented (e.g., Gardner et al., 1995; Pallister et al., 2008; Rutherford et al., 1985; Rutherford and Devine, 2008). This finding is corroborated by a paucity of U-Th model ages (<10% of analyses) within error of eruption. Additionally, all but one of the zircon-bearing Swift Creek stage eruptive units (Jg tephra) exhibit multiple age populations that span on the order of 10^5 years. Each eruptive unit contains a unique combination of populations, but similar ages frequently recur from sample to sample (Fig. 7). We consequently infer that most of our analyzed zircon grains did not grow within their ultimate host melts, but rather were recycled from previous episodes of crystallization. Application of the Ti-in-zircon thermometer to Swift Creek stage zircons mostly yields crystallization temperatures below the eruption temperatures of the final host magmas for reasonable SiO_2 and TiO_2 activities (Fig. 9), suggesting that zircon growth most likely occurred within magma bodies stored beneath the volcano. All of these observations point to construction of the Mount St. Helens magmatic system by repeated intrusion of new magma batches that stall and crystallize within the crust. Taken together with the strong geochemical overlap between zircon analyses from different samples (Figs. 9 and 12–14), they also indicate that erupted Swift Creek magmas primarily entrained and recycled zircon grains from this crystal-rich storage zone (or zones). While we cannot determine the nature of the crystal storage zone(s) with certainty (i.e.,

mostly solidified intrusions vs. crystal mush), intra-grain geochemical trends (see below) and new magnetotelluric data documenting a connection between the magma conduit that supplies Mount St. Helens with an underlying region of high electrical conductivity (Hill et al., 2009) suggest that a large body of partially molten rock may be present beneath the volcano.

Intra-grain variability in zircon trace element signatures reveals multiple magmatic differentiation episodes within a complex magmatic plumbing system. Increases in Hf and Yb/Nd and decreases in temperature and Th/U reflect melt evolution by mineral fractionation (and perhaps magma mixing) whereas decreases in Hf and Yb/Nd and increases in temperature and Th/U most likely reflect interaction of evolved magma hosting zircon grains with hotter, more mafic magma. Accordingly, fluctuations in geochemistry from the center to the edge of most Swift Creek zircon grains (Fig. 15) document multi-stage histories of growth, fractionation, solidification, rejuvenation, and interaction with new magma batches within a melt-rich storage zone(s). Variable compositional trends from center to edge record differing histories for individual grains from any one sample (precluding the possibility that Swift Creek eruptions all tapped the same source) and suggest mixing of zircon crystals by magma interaction.

The geochemical signatures of Swift Creek stage zircon grains illustrate that older zircon growth zones (>~60–100 ka) crystallized from cooler, more evolved melts than younger zircon growth zones. These two groups significantly overlap in composition and temperature, as many younger analyses exhibit features similar to those of the most evolved zircon growth zones and several older analyses display relatively undifferentiated trace element signatures. Nevertheless, older analytical spots typically exhibit higher Hf, lower $T_{Ti\text{-}in\text{-}zirc}$, higher Yb/Nd, and lower Th/U than younger spots. This trend of decreasing evolution with time implies that the fundamentally dacitic magma system of Mount St. Helens has been strongly influenced by input of mafic magma since ~100–60 ka. This finding reinforces several previous investigations of the mineralogy and geochemistry of Mount St. Helens eruptive products that also suggest increasing input of mafic melt through time (e.g., Clynne et al., 2008; Gardner et al., 1995; Smith and Leeman, 1993), but we argue that mafic input began much earlier than previously inferred (~1.2 ka). Since erupted Swift Creek magmas were generally undersaturated in zircon and zircon crystallization ages primarily range from tens to hundreds of thousands of years before eruption, our analyses do not provide insight into the compositional cycles and magmatic interactions that took place during the Swift Creek stage, but instead predominantly record earlier stages of the magmatic system.

The U-Th age spectra of zircons from rocks of the Swift Creek eruptive stage record ~250 k.y. of the construction of the Mount St. Helens magmatic system (Fig. 8) while U-Th and U-Pb age spectra of zircons from lithologic units spanning the entire eruptive history indicate that magmatism initiated by around 500 ka (Claiborne et al., in prep.). Most sample isochron ages and the isochron ages for Swift Creek samples as a whole are resolvable, even when taking into account minimum and maximum ages. Coupled with strong overall agreement between ages determined from isochron diagrams, probability density curves, and the Isoplot Unmix function, this suggests that Swift Creek zircons grew episodically, with dominant periods of magma intrusion and subsequent zircon crystallization taking place at ~20–30, 40, 60, 100, and 160 ka (Fig. 8). Nevertheless, we cannot rule out continuous growth due to the high extent of overlap between the error ellipses of U-Th analyses and the spread of the U-Th age spectra. It is also important to note that our overall conclusions about the construction and evolution of the Mount St. Helens magmatic system are not affected if the absolute ages cited above are incorrect or if growth was continuous.

Overall, our U-Th radiometric age and trace element analyses suggest the following model for assembly of the Mount St. Helens magmatic system. Dacitic melts (potentially generated by partial melting of the lower crust due to injections of basaltic melt: e.g., Smith and Leeman, 1987) periodically rise into the crust below the present site of the volcanic edifice, stall, and crystallize to produce zircon-bearing intrusive bodies. Subsequent pulses of ascending magma rejuvenate and interact with these bodies, mixing zircon crystal populations and inducing new phases of zircon growth and melt fractionation over periods of 10^3–10^4 yrs. The zircon storage zones were only occasionally injected by less evolved magmas during the early stages of the Mount St. Helens magmatic system, but mafic input became more common starting around ~100–60 ka. Throughout the history of the volcano, magmas that do not stall in the crust interact with and rejuvenate the intrusive bodies on their way to eruption, thereby entraining, recycling, and mixing zircon grains. Erupted magmas apparently ascend rapidly through the crust, as U-series disequilibria in plagioclase phenocrysts from recent (<2.2 ka) Mount St. Helens lavas record crustal residence times of less than one thousand years (Cooper and Reid, 2003; Cooper and Donnelly, 2008). Major phases within Mount St. Helens rocks therefore record the history of erupted magmas while zircon primarily records the magmatic conditions within the storage zones underlying the volcano.

This study and the associated investigation of Claiborne et al. (in prep.) are the first to document the existence of an active intrusive complex beneath an arc volcano and record a clear connection between the intrusive

complex and volcanic activity. We also extend evidence for the incremental accumulation of large-scale batholiths over periods of 10^5–10^6 yrs (e.g., Bolhar et al., 2008; Claiborne et al., in revision; Coleman et al., 2004; Glazner et al., 2004; Lipman, 2007; Miller et al., 2007; Walker et al., 2007) to small-scale volcanic systems. Lastly, the focused investigation of a brief eruptive episode presented in this contribution reveals the same history as zircon grains obtained from a broad sampling of eruptive units spanning the entire history of the volcano (Claiborne et al., in prep.), implying that a detailed view of the plumbing system of volcanic complexes may not require exhaustive sampling of all (or most) eruptive products.

CHAPTER VI

CONCLUSIONS

We employed combined U-Th radiometric age and trace element analyses of zircon from eruptive units of the Swift Creek stage (16–10 ka) of Mount St. Helens in order to obtain time-temperature-composition records of the melts from which these crystals grew. Our results reveal the construction and evolution of the magmatic system beneath Mount St. Helens and have ramifications for the assembly of small-scale volcanic complexes and the connection between volcanic and plutonic rocks. More specifically, we draw the following conclusions:

(1) Zircons from most samples contain multiple populations of U-Th ages that span on the order of 10^5 years. Each of the Swift Creek eruptive units contains a unique combination of populations, but similar ages frequently recur from sample to sample. The vast majority of measured model ages range from tens to hundreds of thousands of year before eruption, and only a small portion (<10%) fall within error of sample eruption ages. We infer that Swift Creek stage zircons grew episodically, with periods of crystallization occurring at ~20–30, 40, 60, 100, and 160 ka. Many analyses also exhibit ages <20 ka and >160 ka, but these may not represent single, coherent populations.

(2) For the most part, there are no major geochemical distinctions among analyses of different spot locations and zircon grains extracted from different samples. However, older analytical spots (>~60–100 ka) typically show evidence of having grown from more evolved melts (i.e., higher Hf and Yb/Nd, lower crystallization temperature and Th/U) than younger analytical spots. This trend suggests that the fundamentally dacitic magma system of Mount St. Helens has been strongly influenced by input of mafic magma since ~100–60 ka. We primarily attribute the evolution of trace element signatures observed within Swift Creek stage zircons to fractionation of zircon, apatite, and another unknown accessory mineral (or minerals).

(3) Individual zircons from any one Swift Creek stage sample exhibit fluctuations in trace element signatures from the centers to the edges of grains, recording multi-stage histories of growth, fractionation, solidification, rejuvenation, and interaction with new magma batches within a melt-rich zone beneath the volcano over periods of 10^3–10^4 yrs. Variable patterns of fluctuation record differing histories for individual grains and suggest mixing of zircon populations due to magma interactions.

(4) The Mount St. Helens magmatic system has been constructed over hundreds of thousands of years by repeated intrusion of new magma batches that stall and crystallize within the crust to produce a crystal storage zone (or zones). Zircon trace element signatures primarily record the long-term magmatic conditions and interactions within this active intrusive body and do not record conditions immediately preceding eruption. Pulses of ascending magma rejuvenate and interact with these bodies, mixing zircon crystal populations and inducing new phases of zircon growth and melt fractionation. Magmas that do not stall in the crust entrain and mix zircon crystals from the crystal storage zone(s) and carry them to eruption. This study is one of the first to document the existence of an intrusive complex beneath an active arc volcano and records a clear connection between Mount St. Helens volcanism and an underlying plutonic magmatic system. Our results also suggest that, similar to large-scale batholiths, small-scale volcanic systems accumulate in small increments over prolonged periods of time (10^5–10^6 yrs.).

(5) Zircons from a detailed sampling of eruptive units of the Swift Creek stage (16–10 ka) generally exhibit U-Th age spectra and trace element signatures similar to those documented in zircon grains from a broad sampling of Ape Canyon (300–35 ka), Cougar (28–18 ka), and Spirit Lake (3.9 ka–present) stage rocks. This finding suggests that a detailed view of the construction, evolution, and magmatic plumbing of volcanic complexes may not require exhaustive sampling of all (or most) erupted units.

APPENDIX

SHRIMP DATA AND CATHODOLUMINESCENCE IMAGES OF ZIRCON GRAINS EXTRACTED FROM SWIFT CREEK STAGE ROCKS

(for cathodoluminescence images, see files SHD08-2Z_CL.pdf, SHD08-3Z_CL.pdf, SHD08-5Z_CL.pdf, SHD08-8Z_CL.pdf, SHD08-12Z_CL.pdf, SHD08-13Z_CL.pdf, SHD08-14Z_CL.pdf, and SHD08-15Z_CL.pdf)

Table A1. Radiometric age analyses of zircon grains extracted from Swift Creek stage rocks

Age Spot #	Trace Elements? [a]	($^{238}U/^{232}Th$)	±1σ	($^{230}Th/^{232}Th$)	±1σ	Isochron Slope [b]	±1σ	Model Age (ka) [c]	−1σ [c]	+1σ [c]	Corrected $^{238}U/^{206}Pb$ Age (Ma) ±1σ	Isochron Age (ka) [d]
SHD08-2Z												
1.1	yes	16.43	0.54	13.17	0.58	0.786	0.048	168	22	28	–	168
1.2	yes	13.20	0.43	10.31	0.39	0.759	0.045	155	19	22	–	168
2.1	yes	19.61	0.65	16.37	0.68	0.823	0.048	190	26	34	–	168
2.2	yes	12.66	0.42	10.79	0.32	0.836	0.043	198	26	34	–	168
3.1	yes	4.08	0.13	3.07	0.12	0.649	0.071	115	20	25	–	103
4.1	yes	12.12	0.40	7.48	0.36	0.574	0.041	93	10	11	–	103
SHD08-3Z												
1.2	yes	4.51	0.15	1.87	0.13	0.202	0.055	25	7	8	–	26
2.2	yes	16.72	0.54	14.72	0.52	0.871	0.046	224	34	49	–	280
2.3	yes	19.68	0.64	16.00	0.61	0.801	0.044	176	22	27	–	168
3.1	yes	8.58	0.28	4.21	0.25	0.408	0.041	57	7	8	–	62
4.1	yes	4.18	0.14	2.08	0.13	0.294	0.063	38	9	10	–	39
4.2	yes	8.47	0.28	2.37	0.16	0.161	0.028	19	4	4	–	16
5.1	yes	3.68	0.12	2.28	0.12	0.435	0.076	62	14	16	–	62
5.2	yes	8.76	0.29	8.27	0.53	0.936	0.082	300	90	und.	–	280
5.3	yes	7.13	0.23	2.65	0.16	0.244	0.035	31	5	5	–	26
6.1	yes	7.72	0.25	3.37	0.20	0.334	0.038	44	6	6	–	39
6.2	yes	9.17	0.30	3.35	0.24	0.270	0.036	34	5	5	–	26
6.3	yes	8.21	0.27	4.18	0.26	0.426	0.045	61	8	9	–	62
7.1	yes	21.96	0.71	21.35	0.62	0.971	0.046	385	102	und.	–	280
7.2	yes	45.46	1.48	35.91	1.25	0.784	0.039	167	18	22	–	168
8.1	yes	10.95	0.36	5.31	0.35	0.422	0.041	60	7	8	–	62
8.2	yes	11.64	0.38	10.04	0.26	0.847	0.042	205	27	35	–	168

Table A1. (continued)

Age Spot #	Trace Elements? [a]	($^{238}U/^{232}Th$)	±1σ	($^{230}Th/^{232}Th$)	±1σ	Isochron Slope [b]	±1σ	Model Age (ka) [c]	−1σ [c]	+1σ [c]	Corrected $^{238}U/^{206}Pb$ Age (Ma) ±1σ	Isochron Age (ka) [d]
SHD08-3Z												
9.1	yes	7.44	0.24	4.29	0.25	0.496	0.050	75	10	11	–	62
9.3	no	8.54	0.28	3.73	0.25	0.345	0.041	46	7	7	–	39
10.1	yes	7.56	0.25	2.21	0.12	0.158	0.028	19	4	4	–	16
10.2	yes	4.25	0.14	2.74	0.17	0.505	0.074	77	15	18	–	62
10.3	yes	4.64	0.15	2.97	0.19	0.515	0.072	79	15	18	–	62
10.4	yes	10.21	0.33	3.72	0.23	0.280	0.031	36	5	5	–	39
11.1	no	6.58	0.21	3.96	0.31	0.514	0.066	79	14	16	–	62
11.2	no	8.61	0.28	2.95	0.20	0.237	0.033	29	5	5	–	26
12.1	no	5.38	0.17	2.10	0.14	0.215	0.045	26	6	6	–	26
13.1	no	8.95	0.29	3.56	0.25	0.305	0.038	40	6	6	–	39
13.2	no	4.54	0.15	2.81	0.18	0.482	0.071	72	14	16	–	62
14.1	no	7.21	0.23	3.16	0.21	0.326	0.043	43	7	7	–	39
14.2	no	6.22	0.20	2.90	0.19	0.339	0.048	45	8	8	–	39
15.1	no	4.57	0.15	2.54	0.16	0.397	0.063	55	11	12	–	62
SHD08-5Z												
1.2	yes	10.69	0.30	3.91	0.08	0.286	0.018	37	3	3	–	39
1.3	no	11.32	0.35	3.41	0.19	0.218	0.023	27	3	3	–	26
2.2	yes	15.59	0.48	13.33	0.26	0.843	0.035	202	22	28	–	168
4.1	yes	3.64	0.11	1.82	0.07	0.255	0.060	32	9	9	–	39
5.2	yes	17.27	0.51	11.01	0.34	0.610	0.030	103	8	9	–	103
6.1	yes	3.45	0.10	1.64	0.05	0.196	0.060	24	8	8	–	26
7.2	yes	4.33	0.14	2.37	0.11	0.375	0.056	51	9	10	–	62
8.2	yes	13.95	0.40	11.94	0.29	0.842	0.037	202	23	29	0.21 ± 0.02	168

Table A1. (continued)

Age Spot #	Trace Elements? [a]	($^{238}U/^{232}Th$)	±1σ	($^{230}Th/^{232}Th$)	±1σ	Isochron Slope [b]	±1σ	Model Age (ka) [c]	–1σ [c]	+1σ [c]	Corrected $^{238}U/^{206}Pb$ Age (Ma) ±1σ	Isochron Age (ka) [d]
SHD08-5Z												
9.1	yes	8.46	0.26	7.99	0.31	0.934	0.059	297	70	250	–	280
9.2	yes	5.21	0.17	5.24	0.18	1.007	0.075	und.	und.	und.	25.5 ± 0.46	NA
10.1	yes	4.88	0.15	1.97	0.09	0.210	0.042	26	6	6	–	26
10.2	yes	7.80	0.28	2.38	0.12	0.179	0.027	22	4	4	–	26
11.1	yes	4.75	0.15	2.15	0.10	0.268	0.046	34	7	7	–	39
11.2	yes	8.56	0.28	3.62	0.18	0.329	0.032	44	5	5	–	39
12.1	yes	9.30	0.28	4.73	0.22	0.436	0.035	63	7	7	–	62
12.3	no	12.14	0.39	2.59	0.12	0.127	0.016	15	2	2	–	16
13.1	no	5.49	0.18	5.07	0.25	0.900	0.078	252	63	169	0.05 ± 0.30	280
14.1	no	8.77	0.27	4.87	0.20	0.485	0.036	72	7	8	–	62
14.2	no	6.51	0.20	2.53	0.09	0.250	0.030	31	4	4	–	26
15.1	no	8.93	0.28	2.66	0.12	0.189	0.024	23	3	3	–	26
16.1	no	16.33	0.52	1.36	0.08	0.011	0.009	1	1	1	–	NA
17.1	no	4.19	0.13	2.44	0.10	0.416	0.058	59	10	11	–	62
18.1	no	6.97	0.18	4.81	0.23	0.626	0.051	107	14	16	–	103
SHD08-8Z												
1.1	yes	6.40	0.21	3.44	0.28	0.431	0.063	62	11	13	–	62
1.2	yes	5.00	0.16	2.59	0.17	0.364	0.058	49	10	10	–	62
2.1	yes	11.92	0.39	2.87	0.19	0.156	0.022	19	3	3	–	16
2.2	yes	3.05	0.10	1.94	0.12	0.401	0.097	56	16	19	–	62
3.1	yes	8.20	0.27	3.09	0.18	0.269	0.033	34	5	5	–	39
3.2	yes	11.92	0.39	4.56	0.29	0.313	0.032	41	5	5	–	39
4.1	yes	14.38	0.47	11.41	0.49	0.775	0.048	163	21	26	–	168

Table A1. (continued)

Age Spot #	Trace Elements? [a]	($^{238}U/^{232}Th$)	±1σ	($^{230}Th/^{232}Th$)	±1σ	Isochron Slope [b]	±1σ	Model Age (ka) [c]	−1σ [c]	+1σ [c]	Corrected $^{238}U/^{206}Pb$ Age (Ma) ±1σ	Isochron Age (ka) [d]
SHD08-8Z												
4.2	yes	16.54	0.55	6.60	0.45	0.352	0.033	47	5	6	–	39
5.1	yes	4.20	0.14	2.55	0.14	0.451	0.067	66	13	14	–	62
6.1	yes	16.24	0.53	15.49	0.43	0.950	0.046	327	71	270	–	280
6.2	yes	24.23	0.80	22.00	0.64	0.903	0.043	255	40	63	–	280
7.1	yes	5.24	0.17	2.05	0.11	0.211	0.042	26	6	6	–	26
8.1	yes	11.68	0.38	7.78	0.39	0.628	0.046	108	13	14	–	103
8.2	yes	12.37	0.41	10.91	0.30	0.869	0.044	222	31	44	–	280
9.1	yes	4.44	0.15	2.49	0.09	0.396	0.052	55	9	10	–	62
9.3	no	17.40	0.58	8.25	0.54	0.435	0.038	62	7	8	–	62
10.1	no	19.89	0.65	19.26	0.60	0.967	0.048	371	97	und.	–	280
SHD08-12Z												
1.1	yes	5.04	0.15	1.95	0.08	0.196	0.039	24	5	5	–	26
1.2	yes	10.74	0.33	4.01	0.18	0.295	0.025	38	4	4	–	39
2.1	yes	16.69	0.50	7.92	0.31	0.434	0.026	62	5	5	–	62
4.2	yes	9.45	0.27	5.50	0.28	0.521	0.042	80	9	10	–	62
5.1	yes	6.25	0.19	5.18	0.24	0.788	0.064	170	29	39	–	168
5.2	yes	6.42	0.20	5.15	0.21	0.757	0.057	155	23	29	–	168
6.1	yes	13.90	0.41	4.44	0.21	0.255	0.021	32	3	3	–	39
7.1	yes	9.27	0.29	3.35	0.15	0.267	0.026	34	4	4	–	39
7.2	yes	7.63	0.24	4.83	0.24	0.564	0.048	91	11	13	–	103
8.1	yes	19.59	0.57	15.44	0.36	0.774	0.032	162	14	17	–	168
8.2	yes	20.56	0.63	16.25	0.43	0.777	0.034	164	16	18	–	168

Table A1. (continued)

Age Spot #	Trace Elements? [a]	($^{238}U/^{232}Th$)	±1σ	($^{230}Th/^{232}Th$)	±1σ	Isochron Slope [b]	±1σ	Model Age (ka) [c]	–1σ [c]	+1σ [c]	Corrected $^{238}U/^{206}Pb$ Age (Ma) ±1σ	Isochron Age (ka) [d]
SHD08-12Z												
9.1	yes	3.14	0.10	2.17	0.06	0.498	0.079	75	16	19	–	62
11.1	yes	3.24	0.11	2.03	0.05	0.408	0.072	57	12	14	–	62
11.3	yes	8.90	0.29	3.78	0.15	0.335	0.028	45	5	5	–	39
12.1	no	5.68	0.17	2.54	0.14	0.298	0.044	39	7	7	–	39
13.1	no	5.28	0.16	2.06	0.07	0.211	0.035	26	5	5	–	26
14.1	no	6.14	0.20	2.39	0.13	0.241	0.037	30	5	6	–	26
14.2	no	10.22	0.32	5.00	0.26	0.422	0.036	60	7	7	–	62
15.1	no	4.00	0.12	1.85	0.08	0.232	0.054	29	7	8	–	26
16.1	no	15.44	0.47	11.62	0.33	0.732	0.035	144	13	15	–	168
16.2	no	15.34	0.48	11.71	0.34	0.743	0.036	149	15	17	–	168
17.1	no	3.83	0.13	1.71	0.08	0.192	0.056	23	7	8	–	26
SHD08-13Z												
1.1	yes	7.53	0.25	1.84	0.11	0.101	0.027	12	3	3	–	16
1.2	yes	5.51	0.18	4.35	0.31	0.730	0.085	143	30	41	–	168
2.1	yes	5.47	0.18	2.98	0.20	0.417	0.058	59	10	11	–	62
3.1	yes	17.50	0.58	13.82	0.61	0.774	0.047	162	21	26	–	168
3.2	yes	17.47	0.58	11.36	0.50	0.624	0.039	107	11	12	–	103
4.3	yes	4.73	0.16	2.92	0.20	0.487	0.071	73	14	16	–	62
5.1	yes	4.34	0.14	2.14	0.16	0.301	0.066	39	10	11	–	39
5.3	yes	6.00	0.20	2.31	0.15	0.232	0.041	29	6	6	–	26
6.1	yes	3.69	0.12	1.49	0.09	0.118	0.060	14	7	8	–	16
7.2	yes	6.86	0.23	3.74	0.24	0.449	0.052	65	10	11	–	62
8.1	yes	3.27	0.11	1.81	0.08	0.295	0.074	38	11	12	–	39

Table A1. (continued)

Age Spot #	Trace Elements? [a]	($^{238}U/^{232}Th$)	±1σ	($^{230}Th/^{232}Th$)	±1σ	Isochron Slope [b]	±1σ	Model Age (ka) [c]	−1σ [c]	+1σ [c]	Corrected $^{238}U/^{206}Pb$ Age (Ma) ±1σ	Isochron Age (ka) [d]
SHD08-14Z												
1.1	yes	3.59	0.11	2.09	0.10	0.371	0.069	51	11	13	–	62
1.2	yes	4.41	0.14	2.27	0.12	0.334	0.055	44	9	9	–	39
2.1	yes	8.18	0.24	2.83	0.16	0.233	0.030	29	4	4	–	26
2.2	yes	11.81	0.38	5.35	0.30	0.391	0.034	54	6	6	–	62
4.1	yes	10.53	0.29	5.36	0.25	0.446	0.033	64	6	7	–	62
5.2	yes	9.15	0.29	6.22	0.37	0.631	0.055	109	15	18	–	103
7.2	yes	9.84	0.30	4.16	0.18	0.342	0.028	46	5	5	–	39
7.4	no	12.17	0.37	3.62	0.18	0.221	0.021	27	3	3	–	26
8.1	yes	4.66	0.14	1.39	0.07	0.054	0.041	6	5	5	–	NA
8.2	yes	6.86	0.21	2.27	0.12	0.189	0.031	23	4	4	–	26
10.1	yes	12.67	0.39	9.99	0.24	0.766	0.036	159	16	18	–	168
10.2	yes	20.22	0.62	16.51	0.52	0.805	0.039	178	20	24	–	168
12.2	yes	4.93	0.16	2.95	0.15	0.469	0.058	69	11	13	–	62
13.1	yes	21.67	0.66	19.60	0.75	0.899	0.047	250	42	69	32.4 ± 0.74	NA
14.1	no	9.97	0.35	7.71	0.27	0.742	0.046	148	18	21	–	168
14.2	no	10.17	0.33	4.27	0.18	0.343	0.028	46	5	5	–	39
15.1	no	8.60	0.27	9.77	0.42	1.158	0.075	und.	und.	und.	23.1 ± 0.50	NA
16.1	no	5.29	0.17	4.13	0.24	0.715	0.075	137	26	34	–	168
17.1	no	12.80	0.40	10.00	0.24	0.758	0.036	155	15	18	–	168
18.1	no	4.04	0.12	2.26	0.11	0.373	0.062	51	10	11	–	62
19.1	no	7.09	0.22	2.16	0.11	0.163	0.028	19	4	4	–	16
20.1	no	4.43	0.14	2.63	0.14	0.444	0.062	64	12	13	–	62

Table A1. (continued)

Age Spot #	Trace Elements? [a]	($^{238}U/^{232}Th$)	±1σ	($^{230}Th/^{232}Th$)	±1σ	Isochron Slope [b]	±1σ	Model Age (ka) [c]	–1σ [c]	+1σ [c]	Corrected $^{238}U/^{206}Pb$ Age (Ma) ±1σ	Isochron Age (ka) [d]
SHD08-15Z												
1.1	yes	4.41	0.15	1.62	0.11	0.132	0.051	15	6	7	–	16
2.1	yes	4.97	0.16	2.60	0.19	0.372	0.063	51	10	11	–	62
3.2	yes	7.04	0.23	3.43	0.23	0.382	0.047	53	8	9	–	62
4.1	yes	4.45	0.15	3.96	0.28	0.849	0.105	207	58	130	–	168
4.2	yes	6.77	0.22	2.61	0.20	0.253	0.044	32	6	7	–	26
5.1	yes	9.49	0.31	7.76	0.22	0.791	0.044	171	21	26	–	168
5.3	yes	16.74	0.55	12.87	0.47	0.751	0.042	152	17	20	–	168
6.1	yes	3.89	0.13	2.27	0.13	0.399	0.072	56	12	14	–	62
6.2	yes	4.93	0.16	2.68	0.19	0.396	0.064	55	11	12	–	62
6.3	no	3.61	0.12	2.14	0.12	0.391	0.075	54	13	14	–	62
7.1	yes	3.86	0.13	1.94	0.12	0.279	0.066	36	10	10	–	39
8.1	yes	3.41	0.11	1.53	0.06	0.150	0.061	18	8	8	–	16
8.2	yes	3.59	0.12	1.78	0.07	0.244	0.061	31	8	9	–	26
9.1	yes	6.90	0.23	6.42	0.31	0.915	0.072	269	67	205	–	280
10.1	yes	4.14	0.14	2.08	0.14	0.299	0.065	39	10	11	–	39
10.2	yes	2.99	0.10	1.83	0.08	0.353	0.086	48	14	16	–	39
11.1	yes	4.42	0.15	1.77	0.11	0.175	0.051	21	6	7	–	26
12.3	no	4.79	0.16	2.41	0.16	0.337	0.058	45	9	10	–	39

[a] This column states whether or not a trace element analysis was performed in the same spot (or the same zircon domain) as the radiometric age analysis. Note that corresponding trace element and radiometric age spots have the same spot #.
[b] Calculated between the zircon analysis and inferred melt values of ($^{238}U/^{232}Th$) = ($^{230}Th/^{232}Th$) = 1.2.
[c] und. = undefined
[d] Isochron ages reported here are those for all Swift Creek stage samples as a whole (see Fig. 8).

Table A2. Composition of zircon grains extracted from Swift Creek stage rocks (all elemental concentrations are in ppm).

Spot #	Grain Location	Li	Be	B	F	Na	Mg	Al	P	S	K	Ca	Sc	Ti	V	Cr	Mn
SHD08-2Z																	
1.1	center	0.004	0.17	0.1	4	1.5	0.7	26	290	0.4	0.6	2.7	99	3.0	0.02	0.06	0.02
1.2	interior	0.004	1.88	0.0	7	2.0	0.5	21	386	0.0	0.7	2.2	191	9.0	0.10	0.07	0.02
2.1	interior	0.014	0.01	0.1	4	1.8	0.8	21	138	2.2	0.8	1.9	51	2.6	0.02	0.05	0.02
2.2	interior	0.004	0.04	0.1	4	1.5	0.4	20	191	0.0	0.6	1.6	63	3.6	0.02	0.03	0.02
2.3	edge	0.002	0.00	0.0	3	3.5	1.3	32	362	1.1	2.6	2.1	139	3.8	0.03	0.04	0.05
3.1	center	0.008	0.00	0.0	6	3.8	4.0	26	564	1.8	1.3	3.1	172	17.3	0.08	0.07	0.08
3.2	interior	0.003	0.00	0.0	8	3.2	1.0	24	1066	0.7	1.1	4.2	430	14.2	0.22	0.07	0.03
4.1	center	0.006	1.39	0.0	8	3.6	0.6	32	269	1.4	1.2	2.8	119	4.3	0.05	0.06	0.04
4.2	interior	0.001	11.63	0.0	9	4.6	2.0	27	247	2.0	1.9	3.0	144	4.3	0.03	0.11	0.06
SHD08-3Z																	
1.1	interior	0.001	0.00	0.0	11	0.9	0.2	20	289	0.6	0.3	0.5	101	5.0	0.03	0.01	0.03
1.2	interior	0.000	0.00	0.0	14	1.2	0.2	15	167	0.3	0.3	0.5	50	11.5	0.20	0.03	0.03
2.1	tip	0.003	0.01	0.1	11	1.6	0.4	24	138	0.3	0.4	0.4	42	2.8	0.02	0.01	0.04
2.2	center	0.000	0.00	0.0	9	1.5	0.3	19	401	0.6	0.5	0.6	138	3.8	0.03	0.03	0.04
2.3	interior	0.083	0.00	0.0	10	15.9	0.3	74	320	0.3	26.4	1.9	174	6.9	0.05	0.03	0.12
3.1	interior	0.004	0.00	0.3	16	5.3	1.5	24	272	1.6	2.6	2.5	107	6.4	0.11	0.08	0.08
4.1	center	0.003	0.00	0.1	9	1.5	0.4	20	228	0.9	0.4	1.3	92	17.2	0.41	0.03	0.06
4.2	interior	0.003	0.00	0.1	10	1.4	0.3	20	254	0.9	0.4	1.1	110	16.5	0.42	0.01	0.06
4.3	interior	0.006	0.00	0.1	12	1.7	0.3	21	161	0.0	0.4	1.3	53	11.9	0.30	0.03	0.04
5.1	interior	0.003	0.01	0.0	12	1.5	3.5	21	308	0.3	0.3	1.3	102	17.7	0.72	0.03	0.03
5.2	edge	0.004	0.00	0.1	9	1.9	0.5	39	236	1.4	0.5	1.7	70	12.6	0.15	0.03	0.05
5.3	edge	0.006	0.00	0.1	15	1.2	0.4	23	282	1.0	0.4	1.6	118	16.3	0.37	0.03	0.06
5.4	edge	0.004	0.00	0.0	12	1.3	0.3	24	280	0.3	0.4	1.4	144	5.6	0.07	0.04	0.04
5.5	interior	0.001	0.00	0.1	14	1.3	0.3	20	236	0.3	0.4	1.4	97	16.2	0.38	0.04	0.06

Table A2. (continued)

Spot #	Grain Location	Li	Be	B	F	Na	Mg	Al	P	S	K	Ca	Sc	Ti	V	Cr	Mn
SHD08-3Z																	
6.1	center	0.002	0.00	0.0	15	1.9	0.6	26	698	0.9	1.3	2.9	300	23.5	0.03	0.01	0.08
6.2	edge	0.004	0.00	0.1	13	1.5	0.5	63	295	0.3	0.3	1.7	132	9.9	0.02	0.03	0.03
6.3	interior	0.013	0.00	0.0	11	7.2	0.8	42	505	0.3	2.2	2.1	181	26.4	0.11	0.03	0.10
7.1	center	0.329	0.01	0.1	11	32.3	0.9	153	333	0.3	50.2	4.6	170	7.2	0.11	0.03	0.22
7.2	interior	0.001	0.00	0.1	9	1.6	0.5	23	259	0.6	0.4	1.6	130	4.8	0.06	0.05	0.06
7.3	edge	0.020	0.00	0.1	14	2.1	0.7	41	565	0.0	0.5	2.0	158	6.8	0.06	0.03	0.06
8.1	edge	0.004	0.00	0.1	14	3.8	0.9	31	264	0.3	1.9	3.1	112	12.8	0.14	0.04	0.06
8.2	center	0.088	0.00	0.1	11	3.6	1.0	27	424	0.6	2.4	3.3	133	9.1	0.29	0.06	0.10
9.1	interior	0.011	0.02	0.1	18	1.8	0.6	38	177	0.6	0.6	2.1	45	9.1	0.08	0.01	0.05
9.2	interior	0.008	0.00	0.0	10	2.1	3.4	171	118	4.9	2.7	2.3	44	14.3	0.14	0.06	0.08
10.1	tip	0.010	0.01	0.2	12	19.2	1.2	214	394	2.3	48.5	6.3	219	8.3	0.13	0.05	0.30
10.2	center	0.002	0.00	0.1	17	1.6	0.4	39	392	0.9	0.4	1.9	125	16.2	0.42	0.05	0.05
10.3	interior	0.003	0.00	0.1	15	1.9	0.4	24	175	0.8	0.5	1.8	78	13.5	0.24	0.03	0.06
10.4	interior	0.001	0.00	0.1	14	2.1	0.5	33	156	0.0	0.6	1.9	57	11.0	0.05	0.03	0.05
SHD08-5Z																	
1.1	tip	0.022	15.27	0.1	12	2.6	0.8	15	337	0.2	0.9	2.0	136	7.5	0.07	0.10	0.13
1.2	interior	0.376	1.66	0.4	20	228.9	6.9	909	214	0.2	116.6	69.6	75	7.5	0.28	0.09	2.39
2.1	rim	0.070	10.75	0.1	9	2.5	0.7	16	276	0.5	0.6	1.9	92	11.0	0.24	0.06	0.04
2.2	center	0.100	19.91	0.1	12	25.0	2.1	152	303	0.2	17.0	6.7	117	6.9	0.06	0.09	0.56
3.1	interior	0.080	9.02	0.1	12	2.6	0.7	14	254	1.2	0.7	1.9	87	14.1	0.22	0.09	0.06
3.2	interior	0.039	3.81	0.2	14	21.3	1.2	35	314	0.7	1.6	2.7	91	11.5	0.08	0.08	0.09
4.1	center	0.357	116.72	0.1	15	5.7	0.8	17	423	0.7	1.8	2.2	138	19.7	1.78	0.09	0.10
4.2	edge	0.004	1.66	0.1	12	10.5	0.6	27	252	0.9	9.0	1.9	57	9.1	0.08	0.07	0.06
5.1	edge	0.038	1.72	0.1	11	113.4	14.2	14	130	2.7	23.7	35.9	40	2.2	0.00	0.07	0.11

Table A2. (continued)

Spot #	Grain Location	Li	Be	B	F	Na	Mg	Al	P	S	K	Ca	Sc	Ti	V	Cr	Mn
SHD08-5Z																	
5.2	center	0.122	3.69	0.1	12	21.5	1.1	53	356	0.6	6.7	3.5	131	3.9	0.04	0.10	0.21
6.1	interior	0.320	26.97	0.0	12	3.4	0.6	16	294	0.5	0.8	2.8	117	15.9	0.27	0.07	0.09
6.2	tip	0.126	0.01	0.0	7	3.4	0.7	16	110	0.0	1.2	1.7	30	3.0	0.04	0.08	0.08
7.1	tip	0.070	6.53	0.1	7	4.0	0.6	11	287	1.0	1.7	1.3	117	3.5	0.06	0.06	0.06
7.2	center	0.035	9.93	0.1	10	17.8	1.3	53	191	0.7	5.0	3.2	74	13.1	0.50	0.10	0.27
8.1	tip	0.106	32.84	0.3	13	13.8	1.4	60	301	1.4	5.5	4.1	135	5.6	0.11	0.14	0.10
8.2	center	0.084	18.02	0.1	13	4.0	1.2	20	409	1.2	1.0	2.7	151	7.9	0.08	0.09	0.13
9.1	rim	0.010	6.51	0.2	16	6.6	0.9	20	137	0.2	3.0	2.5	66	4.0	0.08	0.11	0.08
9.2	center	0.012	30.90	0.6	28	3.0	0.7	14	343	0.5	1.3	4.1	53	30.8	1.39	0.09	0.07
10.1	center	0.036	24.28	0.1	15	4.5	0.8	21	215	1.0	1.7	2.5	82	11.1	0.39	0.04	0.10
10.2	rim	0.012	34.42	0.1	11	3.5	4.2	16	332	1.2	0.9	4.5	176	9.9	0.13	0.11	0.09
11.1	center	0.178	17.87	0.1	9	2.2	0.7	40	280	2.1	0.6	2.2	80	18.8	0.42	0.08	0.10
11.2	interior	0.006	0.83	0.2	11	2.3	0.7	20	159	1.2	0.6	1.7	44	4.9	0.03	0.08	0.10
12.1	interior	0.045	11.14	0.1	10	3.4	1.1	22	323	1.0	1.0	3.0	88	8.0	0.04	0.06	0.13
12.2	interior	0.054	57.69	0.1	12	7.3	1.0	18	656	1.0	5.8	3.8	200	13.5	0.13	0.09	0.11
SHD08-8Z																	
1.1	center	0.000	0.30	0.1	11	3.7	1.0	52	434	1.2	1.7	4.1	99	10.9	0.26	0.12	0.04
1.2	edge	0.001	57.74	0.0	13	2.7	0.4	20	276	0.0	0.9	1.9	94	14.4	0.49	0.04	0.04
2.1	tip	0.008	36.33	0.1	10	2.8	0.6	19	366	1.0	1.4	2.3	237	7.7	0.04	0.07	0.03
2.2	center	0.060	58.30	0.1	22	2.3	0.5	19	479	0.3	1.0	2.5	50	41.4	0.89	0.06	0.03
2.3	rim	0.010	54.71	0.1	7	2.4	0.5	19	328	0.7	1.0	2.7	147	4.5	0.10	0.04	0.03
3.1	center	0.429	3.06	0.1	12	3.6	0.4	37	302	0.3	1.2	2.3	133	14.3	0.10	0.09	0.04
3.2	rim	0.011	13.19	0.0	13	4.1	0.7	22	337	0.7	1.5	2.7	199	5.6	0.04	0.05	0.03
4.1	center	0.006	12.87	0.1	14	3.2	0.5	23	313	0.7	1.2	2.8	127	2.8	0.02	0.05	0.04

Table A2. (continued)

Spot #	Grain Location	Li	Be	B	F	Na	Mg	Al	P	S	K	Ca	Sc	Ti	V	Cr	Mn
SHD08-8Z																	
4.2	rim	0.005	37.62	0.1	16	5.2	1.0	27	307	1.9	2.3	3.6	202	7.8	0.07	0.07	0.05
5.1	center	0.003	43.79	0.1	17	3.2	0.6	28	221	1.1	1.5	3.8	85	16.9	0.58	0.09	0.04
5.2	tip	0.059	35.56	0.0	13	8.4	1.2	32	315	4.2	3.4	3.8	195	6.4	0.09	0.13	0.06
6.1	tip	0.004	0.00	0.1	12	8.8	2.2	30	230	3.1	3.5	3.4	85	3.2	0.04	0.14	0.04
6.2	center	0.432	0.01	0.1	10	17.3	1.4	56	389	2.7	17.3	4.4	128	4.7	0.03	0.10	0.26
7.1	center	0.030	53.98	0.1	17	4.5	1.4	29	401	0.0	2.4	15.2	123	10.5	0.18	0.09	0.04
7.2	edge	0.043	34.10	0.1	13	9.4	2.5	37	373	5.2	3.8	3.8	188	8.1	0.11	0.10	0.08
8.1	rim	0.013	0.35	0.1	10	6.1	1.2	55	282	1.7	6.8	4.9	54	10.6	0.07	0.05	0.11
8.2	center	0.021	8.00	0.1	12	8.6	2.2	37	307	0.4	6.2	4.7	127	4.8	0.04	0.10	0.10
9.1	center	0.021	1.52	0.1	18	5.2	0.7	37	338	1.7	2.0	3.6	153	7.3	0.02	0.09	0.07
9.2	edge	0.029	22.89	0.1	14	10.7	1.9	36	411	2.5	3.9	5.4	258	7.5	0.10	0.15	0.06
SHD08-12Z																	
1.1	center	0.003	0.00	0.1	15	2.6	0.9	15	391	0.3	0.8	2.9	181	21.4	1.49	0.05	0.06
1.2	interior	0.000	0.00	0.1	12	5.7	2.0	17	393	1.0	2.2	5.8	132	14.0	0.33	0.08	0.05
2.1	center	0.026	0.00	0.1	14	4.2	1.0	19	232	0.0	1.4	2.5	85	4.2	0.09	0.05	0.07
2.2	edge	0.002	0.00	0.0	12	2.3	0.7	16	326	0.3	0.7	2.5	147	18.4	0.32	0.05	0.05
2.3	edge	0.000	0.00	0.0	13	2.3	0.7	31	333	0.5	0.8	2.3	91	13.5	0.22	0.08	0.09
3.1	interior	0.004	0.00	0.1	16	3.9	0.8	23	91	0.5	1.2	2.6	26	9.1	0.04	0.08	0.11
3.2	interior	0.001	0.00	0.0	12	2.9	1.4	28	101	1.0	0.9	2.8	25	7.1	0.25	0.15	0.08
4.1	edge	0.289	0.00	0.7	19	349.3	30.5	2057	136	0.5	180.3	87.3	46	32.0	0.28	0.08	5.99
4.2	center	0.022	0.00	0.2	14	17.3	1.9	24	114	1.0	2.5	4.5	34	9.0	0.02	0.05	0.05
5.1	center	0.012	0.00	0.5	15	3.2	1.0	21	216	0.7	0.9	2.7	36	24.7	0.85	0.10	0.09
5.2	interior	0.009	0.00	0.3	16	2.1	0.6	14	222	0.7	0.6	1.9	36	24.0	0.38	0.03	0.07
6.1	tip	0.003	0.00	0.2	18	2.8	0.5	16	309	0.7	0.7	1.9	111	3.7	0.02	0.08	0.07

Table A2. (continued)

Spot #	Grain Location	Li	Be	B	F	Na	Mg	Al	P	S	K	Ca	Sc	Ti	V	Cr	Mn
SHD08-12Z																	
6.2	center	0.011	0.00	0.2	12	1.7	0.7	59	217	0.0	0.6	2.1	67	11.2	0.05	0.07	0.07
7.1	interior	0.010	0.00	0.1	16	4.8	0.5	14	296	0.7	1.5	1.9	115	14.9	0.82	0.08	0.07
7.2	interior	0.004	0.00	0.1	13	9.1	0.6	29	349	0.6	6.4	1.8	105	13.3	0.45	0.06	0.04
7.3	edge	0.017	0.00	0.1	10	5.2	0.5	26	132	0.2	2.9	2.1	44	10.5	0.12	0.05	0.07
7.4	tip	0.058	0.00	0.1	12	14.2	0.9	84	201	0.4	11.5	3.0	80	10.0	0.19	0.05	0.25
8.1	interior	0.024	0.00	0.1	12	2.3	0.6	12	330	0.2	1.1	2.3	144	5.6	0.04	0.05	0.07
8.2	center	0.048	0.00	0.1	9	4.3	0.9	17	377	0.4	2.1	2.3	136	4.8	0.10	0.05	0.09
9.1	center	0.000	0.00	0.0	10	6.2	0.7	36	186	0.2	3.2	2.0	55	3.8	0.52	0.06	0.14
9.2	rim	0.000	0.00	0.0	16	2.1	0.5	20	151	0.5	0.6	1.6	41	11.9	0.15	0.04	0.04
10.1	center	0.052	0.00	0.0	13	2.3	0.7	16	283	0.4	0.6	1.9	106	16.2	0.30	0.03	0.04
10.2	edge	0.007	0.00	0.0	13	5.2	0.8	57	234	0.5	4.7	3.0	60	10.0	0.25	0.06	0.11
11.1	center	0.072	0.02	0.1	10	17.6	2.9	16	798	0.2	7.3	7.2	267	11.2	0.12	0.06	0.07
11.3	tip	0.016	0.01	0.2	8	4.3	0.7	16	327	0.2	2.7	1.8	110	6.9	0.21	0.08	0.07
SHD08-13Z																	
1.1	interior	1.311	43.84	0.0	15	2.0	0.6	15	292	1.4	1.0	1.7	182	7.1	0.10	0.04	0.03
1.2	center	0.594	14.84	0.0	10	1.3	0.3	21	131	0.5	0.7	1.5	48	11.2	0.17	0.06	0.02
2.1	interior	51.604	18.71	0.0	16	2.2	0.5	22	155	1.2	1.2	1.7	52	12.3	0.22	0.06	0.03
3.1	center	21.126	4.30	0.1	17	1.8	0.5	18	224	0.3	1.1	2.4	115	3.1	0.02	0.05	0.03
3.2	tip	30.645	34.17	0.0	12	2.3	0.9	20	348	1.8	2.8	1.4	187	17.1	0.15	0.04	0.09
4.1	tip	0.315	0.15	0.0	11	1.5	0.3	17	116	0.3	0.7	1.7	41	10.6	0.20	0.03	0.02
4.2	center	0.404	0.05	0.0	10	5.7	0.5	36	284	0.0	5.1	3.5	89	12.0	0.18	0.03	0.11
4.3	edge	0.990	1.56	0.0	9	1.0	0.2	18	144	0.9	0.7	1.5	56	7.2	0.10	0.04	0.03
5.1	interior	31.900	26.52	0.1	21	2.2	0.5	24	194	0.5	1.0	3.1	85	14.3	0.31	0.08	0.04

Table A2. (continued)

Spot #	Grain Location	Li	Be	B	F	Na	Mg	Al	P	S	K	Ca	Sc	Ti	V	Cr	Mn
SHD08-13Z																	
5.2	edge	1.705	0.52	0.1	18	2.9	0.7	40	402	0.8	1.3	3.4	124	14.3	0.31	0.08	0.04
5.3	tip	12.032	6.96	0.1	13	5.8	0.6	22	199	0.2	2.6	2.7	94	15.9	0.38	0.05	0.05
6.1	interior	7.739	69.03	0.0	19	2.5	0.6	22	371	1.1	1.4	2.9	102	19.5	1.04	0.06	0.03
7.1	interior	1.754	9.87	0.1	17	2.9	0.5	27	182	0.0	1.2	3.0	71	12.9	0.31	0.06	0.04
7.2	edge	1.514	11.62	0.1	16	2.2	0.5	26	273	0.0	1.2	2.6	91	14.7	0.37	0.05	0.03
8.1	interior	5.254	150.04	0.1	11	1.9	0.4	17	423	0.5	1.0	2.1	156	17.1	0.78	0.06	0.03
8.2	edge	6.166	197.33	0.0	15	2.4	0.6	19	567	0.7	1.1	2.5	208	17.9	1.00	0.03	0.02
8.3	edge	1.231	30.19	0.0	10	2.4	0.4	19	211	0.2	0.9	1.9	92	13.6	0.39	0.04	0.03
9.1	interior	8.945	12.03	0.0	9	1.8	3.5	37	178	0.2	0.8	1.7	54	9.7	0.08	0.05	0.03
10.1	center	3.623	19.71	0.1	16	10.3	0.8	18	188	1.1	3.6	3.7	55	10.9	0.77	0.10	0.06
SHD08-14Z																	
1.1	center	0.006	49.66	0.0	15	1.2	0.5	12	326	0.6	0.4	1.7	110	16.2	0.93	0.07	0.06
1.2	rim	0.000	13.19	0.1	6	1.3	0.6	14	314	0.5	0.5	1.6	104	12.3	0.25	0.07	0.08
2.1	center	0.000	25.58	0.1	10	2.5	0.8	21	296	0.7	0.7	2.0	92	9.9	0.26	0.08	0.06
2.2	tip	0.000	20.49	0.1	8	1.2	0.4	12	373	0.2	0.4	1.5	144	9.9	0.14	0.06	0.04
3.1	interior	0.000	8.00	0.1	15	2.7	1.0	24	145	0.9	0.9	3.2	40	8.8	0.17	0.05	0.08
3.2	interior	0.000	0.17	0.1	11	1.9	0.6	29	310	0.9	0.7	2.1	87	12.7	0.18	0.02	0.06
4.1	center	0.000	12.63	0.2	15	2.2	0.9	22	260	0.2	0.9	2.4	75	7.1	0.15	0.07	0.06
4.2	edge	0.000	2.01	0.0	11	2.0	1.2	25	176	2.9	0.9	3.1	41	8.4	0.04	0.07	0.06
4.3	edge	0.000	5.63	0.1	17	2.1	0.9	22	248	1.2	0.7	2.5	93	15.9	0.46	0.07	0.06
5.1	center	0.000	6.33	0.1	11	2.1	0.8	21	161	0.0	0.8	2.5	41	9.7	0.11	0.03	0.08
5.2	rim	0.000	30.37	0.3	13	2.4	0.9	17	313	0.8	0.9	3.0	112	10.0	0.12	0.04	0.07
6.1	edge	0.000	7.59	0.1	13	3.0	1.7	28	135	0.5	1.0	3.5	44	11.0	0.31	0.05	0.30

Table A2. (continued)

Spot #	Grain Location	Li	Be	B	F	Na	Mg	Al	P	S	K	Ca	Sc	Ti	V	Cr	Mn
SHD08-14Z																	
6.2	center	0.001	26.55	0.1	15	3.1	0.8	25	364	0.3	0.9	2.9	116	14.6	0.43	0.05	0.05
7.1	rim	0.009	25.55	0.1	18	2.0	0.7	14	394	0.2	0.7	17.9	156	7.1	0.07	0.06	0.07
7.2	center	0.008	15.13	0.1	13	2.4	0.7	17	397	0.5	0.8	2.7	149	6.4	0.13	0.09	0.07
7.3	interior	0.015	50.49	0.1	14	2.3	0.9	16	443	0.7	0.8	2.8	220	9.0	0.24	0.12	0.06
8.1	center	0.015	58.74	0.1	15	2.4	0.8	15	279	0.2	0.9	3.0	90	15.5	1.49	0.12	0.05
8.2	interior	0.009	46.81	0.2	18	3.1	1.1	17	433	0.0	1.1	3.2	220	22.9	0.63	0.03	0.07
8.3	edge	0.003	12.49	0.1	12	2.4	0.9	18	190	0.5	0.9	2.6	49	6.2	0.08	0.04	0.05
9.1	interior	0.017	77.78	0.2	19	13.5	3.9	40	345	1.9	4.5	6.2	89	16.3	1.17	0.15	0.15
10.1	tip	0.023	4.00	0.2	15	30.8	2.7	24	221	2.2	12.0	9.8	68	3.9	0.08	0.07	0.43
10.2	center	0.022	7.08	0.1	19	6.8	1.1	19	347	0.2	3.4	3.3	126	4.3	0.21	0.06	0.10
11.1	rim	0.009	7.50	0.2	15	3.2	0.8	21	202	0.3	1.2	2.8	82	9.5	0.26	0.09	0.08
11.2	center	0.007	3.89	0.1	15	3.6	0.9	26	153	1.0	1.4	2.8	37	9.4	0.16	0.07	0.08
12.1	center	0.003	0.64	0.1	17	3.6	0.8	35	383	1.8	1.8	2.6	107	13.4	0.28	0.07	0.09
12.2	interior	0.004	6.81	0.1	13	2.4	0.8	20	137	0.5	0.8	2.2	43	5.8	0.20	0.09	0.06
13.1	tip	0.010	0.10	0.2	18	4.1	2.5	25	100	1.5	1.2	3.8	28	1.6	0.00	0.08	0.11
13.2	interior	0.123	2.69	0.3	15	8.1	1.5	37	173	1.4	2.2	3.6	40	12.0	0.16	0.09	0.23
SHD08-15Z																	
1.1	center	19.050	0.34	0.1	15	2.3	2.9	38	290	0.6	0.9	6.2	65	11.3	0.05	0.04	0.03
2.1	interior	0.016	12.94	0.1	15	1.9	0.5	22	202	0.6	0.8	2.1	71	10.9	0.29	0.07	0.02
2.2	interior	0.016	23.96	0.1	13	2.4	0.8	25	189	1.2	1.1	1.8	67	13.1	0.25	0.05	0.05
3.1	interior	0.066	18.36	0.1	13	2.5	2.2	23	223	1.9	1.3	3.6	79	14.3	0.06	0.04	0.08
3.2	interior	0.931	3.62	0.1	17	3.1	1.1	37	245	0.8	1.3	3.2	65	12.4	0.10	0.06	0.10
4.1	edge	0.032	71.83	0.0	14	2.1	1.2	22	207	1.4	0.7	1.9	66	11.9	0.41	0.08	0.06

Table A2. (continued)

Spot #	Grain Location	Li	Be	B	F	Na	Mg	Al	P	S	K	Ca	Sc	Ti	V	Cr	Mn
SHD08-15Z																	
4.2	tip	0.067	36.52	0.1	12	10.7	4.4	32	291	2.2	2.6	2.8	130	17.7	0.44	0.16	0.19
5.1	rim	6.547	0.97	0.0	11	2.7	2.2	22	298	1.3	1.1	2.1	92	4.9	0.04	0.06	0.05
5.2	interior	12.141	2.54	0.1	18	5.7	3.9	30	251	1.3	4.1	2.5	120	3.9	0.06	0.10	0.10
5.3	center	7.312	0.91	0.0	13	1.6	0.7	11	281	0.3	0.9	1.3	120	3.1	0.03	0.02	0.02
6.1	edge	0.022	23.23	0.3	16	2.6	1.5	21	251	0.3	1.1	4.6	76	13.3	0.29	0.06	0.03
6.2	edge	0.068	25.20	0.4	18	13.7	1.7	60	198	0.6	26.8	3.2	71	15.5	0.40	0.06	0.24
7.1	interior	33.476	75.14	0.0	12	2.0	1.3	19	346	1.4	1.0	2.6	125	17.4	0.81	0.06	0.04
7.2	interior	4.089	0.58	0.0	9	2.7	1.4	20	94	0.8	1.3	2.6	36	3.5	0.03	0.06	0.06
8.1	center	0.096	61.70	0.2	13	2.5	1.5	21	363	0.0	0.9	3.6	63	9.8	0.18	0.06	0.05
8.2	edge	0.053	57.63	0.0	8	3.7	1.1	42	314	0.0	1.4	2.2	62	8.1	0.16	0.03	0.03
9.1	interior	0.499	5.97	0.8	22	20.3	2.3	363	135	4.2	65.5	7.4	34	13.9	0.85	0.10	0.29
10.1	rim	0.012	1.97	0.1	17	8.4	5.5	67	147	4.7	2.5	8.3	38	11.6	0.11	0.10	0.10
10.2	center	0.009	8.75	0.1	15	4.7	2.5	44	192	2.1	1.7	4.0	52	12.3	0.14	0.07	0.05
11.1	interior	0.017	22.12	0.1	16	4.1	2.6	49	456	2.1	1.6	4.2	119	20.1	0.14	0.09	0.12
12.1	center	0.114	0.35	0.1	16	3.9	2.6	43	83	0.9	1.8	6.6	23	8.3	0.08	0.09	0.04
12.2	edge	0.020	9.37	0.1	19	6.1	1.1	39	206	2.1	2.1	3.7	51	9.4	0.06	0.03	0.06

Table A2. (continued)

Spot #	Grain Location	Fe	Ge	Y	Nb	La	Ce	Ce* [a]	Pr [a]	Nd	Sm	Eu	Eu* [a]	Ho	Gd	Tb	Dy
SHD08-2Z																	
1.1	center	0.8	0.1	581	1	0.003	10	0.05	0.024	0.36	1.02	0.597	0.949	18	8	3.08	36
1.2	interior	0.9	0.4	1641	6	0.004	30	0.07	0.039	0.72	3.07	1.791	3.459	60	36	12.43	129
2.1	interior	0.7	0.0	321	1	0.016	5	0.02	0.010	0.15	0.47	0.216	0.521	11	5	2.09	22
2.2	interior	0.6	0.1	484	3	0.000	10	0.03	0.015	0.24	0.76	0.515	0.877	17	9	3.26	39
2.3	edge	2.4	0.1	676	1	0.012	7	0.05	0.021	0.35	1.13	0.719	1.208	25	12	5.05	50
3.1	center	3.0	0.2	1695	5	0.003	21	0.42	0.174	2.47	6.24	3.729	6.025	64	54	16.62	179
3.2	interior	1.2	0.4	4234	9	0.147	71	3.41	1.251	15.81	31.81	15.172	25.833	164	194	54.54	382
4.1	center	1.2	0.1	500	1	0.009	6	0.01	0.009	0.18	1.06	0.641	0.976	18	8	3.35	39
4.2	interior	1.4	0.2	915	4	0.017	16	0.06	0.028	0.48	1.69	0.901	1.782	33	17	6.63	69
SHD08-3Z																	
1.1	interior	0.4	0.1	548	1	0.008	6	0.07	0.028	0.41	1.08	0.400	1.199	21	12	4.39	42
1.2	interior	0.3	0.2	1004	1	0.017	16	0.77	0.248	2.76	4.31	2.095	3.777	38	31	9.44	94
2.1	tip	0.6	0.1	210	1	0.008	5	0.01	0.007	0.11	0.33	0.251	0.379	7	4	1.65	17
2.2	center	0.6	0.1	871	2	0.016	11	0.04	0.021	0.36	1.35	0.906	1.559	30	17	6.02	63
2.3	interior	5.4	0.4	1349	7	0.043	22	0.09	0.039	0.63	2.00	1.086	2.208	49	23	9.36	91
3.1	interior	1.1	0.2	1030	1	0.017	11	0.19	0.084	1.30	3.90	1.330	3.850	40	35	11.38	112
4.1	center	0.4	0.2	1197	1	0.025	15	0.52	0.195	2.51	5.19	2.536	4.916	48	43	12.89	128
4.2	interior	0.4	0.1	671	2	0.005	13	0.09	0.039	0.60	1.75	0.815	1.772	25	17	5.49	57
4.3	interior	0.5	0.2	778	1	0.010	11	0.54	0.181	2.08	3.47	1.774	3.096	29	26	7.77	76
5.1	interior	0.6	0.1	1982	2	0.046	23	0.68	0.260	3.42	7.48	3.715	7.404	78	68	21.83	197
5.2	edge	0.7	0.3	454	1	0.003	8	0.06	0.029	0.45	1.35	0.678	1.398	17	13	4.45	40
5.3	edge	0.5	0.2	754	2	0.008	14	0.05	0.027	0.49	2.01	0.888	1.890	29	16	5.68	56
5.4	edge	0.5	0.3	797	2	0.007	9	0.07	0.031	0.49	1.51	0.489	1.688	31	17	6.79	65
5.5	interior	0.5	0.2	1307	2	0.036	16	0.54	0.213	2.88	6.63	2.970	5.998	53	50	15.16	129

Table A2. (continued)

Spot #	Grain Location	Fe	Ge	Y	Nb	La	Ce	Ce*[a]	Pr [a]	Nd	Sm	Eu	Eu* [a]	Ho	Gd	Tb	Dy
SHD08-3Z																	
6.1	center	16.1	0.2	2342	3	0.008	17	0.27	0.128	2.10	7.17	6.050	7.181	90	66	22.72	217
6.2	edge	3.1	0.2	586	1	0.012	5	0.09	0.040	0.61	1.82	1.421	1.824	22	17	5.61	54
6.3	interior	8.8	0.2	1729	5	0.018	15	0.17	0.082	1.33	4.43	4.228	5.097	67	54	18.79	145
7.1	center	8.6	0.2	1366	8	0.066	17	0.06	0.029	0.49	1.75	0.910	2.083	47	23	9.07	100
7.2	interior	1.1	0.1	754	3	0.017	11	0.03	0.014	0.27	1.21	0.722	1.264	26	12	4.87	52
7.3	edge	1.0	0.2	882	2	0.005	8	0.09	0.042	0.65	1.95	0.987	2.033	31	20	6.70	61
8.1	edge	0.7	0.2	657	1	0.028	7	0.07	0.032	0.49	1.51	0.681	1.424	25	12	4.50	52
8.2	center	2.9	0.2	1255	3	0.094	21	0.69	0.237	2.83	5.05	3.171	4.365	45	35	10.76	87
9.1	interior	1.1	0.3	319	2	0.014	8	0.05	0.021	0.30	0.73	0.398	0.700	10	6	1.94	22
9.2	interior	14.4	0.2	513	1	0.459	10	0.42	0.141	1.65	2.82	1.455	2.242	19	16	4.90	45
10.1	tip	15.3	0.3	1228	3	0.065	14	0.06	0.030	0.53	2.12	0.647	2.383	48	25	9.81	110
10.2	center	0.4	0.1	856	1	0.019	13	0.15	0.063	0.91	2.45	1.245	2.553	36	25	8.25	87
10.3	interior	0.5	0.3	831	1	0.005	12	0.24	0.099	1.44	3.85	1.769	3.520	32	30	9.29	89
10.4	interior	0.5	0.2	340	1	0.010	8	0.09	0.033	0.41	0.80	0.576	0.777	11	7	2.49	27
SHD08-5Z																	
1.1	tip	3.4	0.2	942	4	0.074	19	0.07	0.034	0.59	2.22	0.951	2.398	36	24	8.67	94
1.2	interior	67.8	0.4	335	2	0.472	6	0.11	0.038	0.45	0.79	0.476	0.761	13	7	2.56	31
2.1	rim	1.1	0.2	721	2	0.006	12	0.05	0.025	0.41	1.39	0.610	1.400	27	13	4.45	57
2.2	center	66.5	0.2	937	5	0.114	15	0.08	0.036	0.55	1.56	0.882	1.662	33	16	6.05	77
3.1	interior	1.5	0.2	691	2	0.003	10	0.08	0.031	0.44	1.09	0.743	1.237	26	13	4.41	57
3.2	interior	2.5	0.3	615	1	0.009	8	0.10	0.042	0.58	1.43	0.732	1.514	24	15	5.30	58
4.1	center	2.9	0.2	2795	5	0.055	34	0.67	0.291	4.34	12.12	5.542	11.303	116	97	31.19	316
4.2	edge	1.4	0.2	429	1	0.018	8	0.09	0.034	0.48	1.15	0.642	1.115	16	10	3.41	40
5.1	edge	0.9	0.1	322	2	0.261	6	0.01	0.007	0.11	0.38	0.298	0.477	11	6	2.26	27

Table A2. (continued)

Spot #	Grain Location	Fe	Ge	Y	Nb	La	Ce	Ce* [a]	Pr [a]	Nd	Sm	Eu	Eu* [a]	Ho	Gd	Tb	Dy
SHD08-5Z																	
5.2	center	14.1	0.2	741	2	0.042	9	0.03	0.017	0.29	1.12	0.608	1.285	26	14	4.91	63
6.1	interior	5.5	0.3	1239	5	0.168	22	0.72	0.248	2.93	5.18	5.023	4.663	47	39	11.89	126
6.2	tip	4.6	0.1	110	1	0.003	3	0.00	0.002	0.04	0.21	0.119	0.200	4	2	0.74	9
7.1	tip	1.3	0.3	686	3	0.006	14	0.04	0.020	0.35	1.41	0.511	1.637	27	18	6.06	68
7.2	center	22.6	0.2	561	1	0.059	10	0.11	0.045	0.65	1.72	0.796	1.767	23	17	5.58	60
8.1	tip	3.5	0.2	877	5	0.027	22	0.08	0.036	0.59	2.02	0.900	2.009	31	18	7.69	83
8.2	center	5.4	0.3	1070	3	0.033	10	0.16	0.077	1.25	4.13	1.575	3.981	39	35	11.49	113
9.1	rim	3.6	0.2	352	1	0.015	4	0.02	0.010	0.16	0.55	0.322	0.627	12	7	2.57	30
9.2	center	0.7	0.2	1714	1	0.111	13	0.86	0.296	3.52	6.29	1.142	5.458	67	44	15.08	165
10.1	center	6.7	0.3	823	1	0.015	11	0.25	0.101	1.39	3.37	1.251	3.061	34	26	8.15	88
10.2	rim	1.5	0.4	1186	4	0.018	19	0.06	0.033	0.58	2.29	1.011	2.654	48	28	10.24	122
11.1	center	9.4	0.1	980	2	0.086	10	0.66	0.220	2.53	4.22	2.826	3.801	38	32	9.75	101
11.2	interior	4.2	0.1	259	1	0.006	6	0.02	0.009	0.14	0.51	0.217	0.563	9	6	2.14	24
12.1	interior	4.5	0.2	847	3	0.066	11	0.61	0.210	2.47	4.31	2.682	3.467	31	26	8.34	81
12.2	interior	3.3	0.2	2379	10	0.140	43	2.02	0.698	8.31	14.83	9.994	12.372	92	95	27.90	270
SHD08-8Z																	
1.1	center	0.9	0.1	560	1	0.016	10	0.06	0.027	0.44	1.41	0.558	1.350	21	12	3.91	42
1.2	edge	0.8	0.2	1481	2	0.041	18	0.71	0.242	2.85	4.98	2.407	4.775	60	42	14.06	129
2.1	tip	0.8	0.2	1308	6	0.006	22	0.07	0.037	0.65	2.53	1.279	2.864	51	30	10.75	110
2.2	center	0.9	0.3	2087	4	0.102	28	1.25	0.433	5.16	9.20	3.256	8.463	85	72	23.39	203
2.3	rim	0.9	0.3	1490	2	0.018	20	0.33	0.145	2.16	6.06	2.410	5.748	59	50	15.66	120
3.1	center	5.6	0.1	1065	2	0.009	8	0.04	0.019	0.33	1.29	1.227	1.576	41	18	7.38	84
3.2	rim	1.6	0.2	1077	3	0.009	15	0.06	0.030	0.53	2.07	0.879	2.306	42	24	8.38	86
4.1	center	1.3	0.4	700	2	0.009	10	0.07	0.029	0.43	1.16	0.622	1.264	25	13	4.65	49

Table A2. (continued)

Spot #	Grain Location	Fe	Ge	Y	Nb	La	Ce	Ce* [a]	Pr [a]	Nd	Sm	Eu	Eu* [a]	Ho	Gd	Tb	Dy
SHD08-8Z																	
4.2	rim	1.5	0.3	1033	5	0.006	14	0.02	0.013	0.30	1.88	1.019	2.188	41	24	8.43	100
5.1	center	1.2	0.2	1326	2	0.021	16	0.44	0.169	2.24	4.97	2.582	4.666	57	41	14.12	122
5.2	tip	1.3	0.3	1006	4	0.016	17	0.04	0.022	0.41	1.93	0.839	2.180	39	23	8.50	91
6.1	tip	1.2	0.3	676	4	0.010	11	0.03	0.016	0.29	1.18	0.572	1.211	24	11	5.03	50
6.2	center	13.2	0.2	841	2	0.108	8	0.07	0.030	0.45	1.28	0.696	1.399	26	14	5.32	59
7.1	center	2.3	0.1	1845	2	0.095	19	0.65	0.253	3.42	7.87	3.406	7.250	76	62	19.39	188
7.2	edge	2.7	0.1	1278	4	0.044	20	0.09	0.041	0.68	2.25	1.379	2.708	48	30	11.05	112
8.1	rim	43.9	0.2	406	1	0.033	7	0.09	0.032	0.40	0.77	0.430	0.811	15	8	2.89	27
8.2	center	60.5	0.1	738	2	0.011	9	0.04	0.019	0.32	1.15	0.781	1.285	27	13	4.79	48
9.1	center	2.9	0.1	981	4	0.024	20	0.20	0.075	0.96	1.94	1.649	2.003	39	19	7.07	69
9.2	edge	2.2	0.3	1369	5	0.018	19	0.09	0.042	0.69	2.41	1.108	2.856	54	31	10.80	115
SHD08-12Z																	
1.1	center	0.8	0.2	1653	5	0.027	25	0.28	0.110	1.49	3.44	1.744	3.412	64	31	12.29	152
1.2	interior	0.7	0.3	1047	3	0.010	10	0.10	0.041	0.59	1.52	0.775	1.649	38	17	6.47	83
2.1	center	0.8	0.2	512	1	0.013	8	0.04	0.019	0.29	0.93	0.426	0.987	18	10	3.88	47
2.2	edge	0.8	0.2	965	3	0.006	16	0.13	0.054	0.78	2.08	1.005	2.072	38	19	6.88	84
2.3	edge	0.7	0.1	476	1	0.010	8	0.04	0.020	0.32	1.11	0.558	1.125	19	11	3.77	45
3.1	interior	0.7	0.1	217	1	0.013	6	0.03	0.013	0.19	0.55	0.285	0.515	8	4	1.66	19
3.2	interior	0.9	0.1	180	1	0.010	5	0.02	0.011	0.15	0.42	0.199	0.397	6	3	1.26	15
4.1	edge	221.9	0.3	303	1	0.723	7	0.12	0.041	0.47	0.78	0.365	0.739	11	7	2.28	26
4.2	center	0.6	0.2	390	1	0.006	9	0.06	0.027	0.44	1.48	0.777	1.282	13	10	3.06	34
5.1	center	1.1	0.3	914	2	0.025	8	0.14	0.065	1.00	3.05	0.680	3.090	35	29	9.26	99
5.2	interior	0.6	0.3	479	2	0.009	9	0.08	0.032	0.46	1.17	0.274	1.213	18	12	4.22	47
6.1	tip	0.8	0.1	680	2	0.012	10	0.02	0.013	0.25	1.18	0.496	1.378	26	15	5.70	64

Table A2. (continued)

Spot #	Grain Location	Fe	Ge	Y	Nb	La	Ce	Ce* [a]	Pr [a]	Nd	Sm	Eu	Eu* [a]	Ho	Gd	Tb	Dy
SHD08-12Z																	
6.2	center	1.4	0.1	312	1	0.029	3	0.11	0.042	0.54	1.12	0.685	0.947	11	7	2.51	28
7.1	interior	0.8	0.1	802	3	0.014	14	0.17	0.062	0.80	1.68	0.855	1.674	30	15	5.53	69
7.2	interior	0.6	0.3	534	1	0.005	9	0.05	0.025	0.39	1.24	0.653	1.278	21	12	4.61	54
7.3	edge	1.6	0.3	615	1	0.034	11	0.49	0.162	1.85	3.04	1.621	2.531	23	19	6.29	62
7.4	tip	8.3	0.3	474	1	0.029	5	0.03	0.016	0.26	0.85	0.479	0.889	18	9	3.36	40
8.1	interior	1.5	0.2	1263	7	0.018	24	0.06	0.031	0.51	1.77	0.973	1.954	45	20	8.10	99
8.2	center	1.8	0.2	871	2	0.025	9	0.10	0.043	0.61	1.56	0.954	1.592	30	15	6.01	71
9.1	center	3.3	0.2	598	3	0.034	13	0.13	0.052	0.69	1.51	0.665	1.539	24	14	5.00	56
9.2	rim	0.6	0.2	308	2	0.003	9	0.03	0.014	0.23	0.77	0.454	0.809	12	8	2.49	29
10.1	center	0.4	0.3	1432	2	0.066	17	0.60	0.222	2.83	5.76	2.754	5.659	60	51	15.55	160
10.2	edge	3.4	0.2	376	1	0.026	8	0.05	0.021	0.32	0.97	0.542	0.923	14	8	2.69	33
11.1	center	3.2	0.2	2707	8	0.075	94	0.69	0.281	3.93	9.70	5.909	9.224	105	81	26.05	278
11.3	tip	0.7	0.2	839	3	0.003	19	0.09	0.039	0.55	1.39	0.911	1.686	33	19	7.24	80
SHD08-13Z																	
1.1	interior	1.6	0.3	969	2	0.008	12	0.04	0.021	0.39	1.78	0.688	1.962	39	20	8.03	93
1.2	center	1.2	0.2	471	1	0.006	7	0.07	0.033	0.49	1.44	0.809	1.317	18	11	3.65	37
2.1	interior	4.6	0.2	921	1	0.014	13	0.55	0.196	2.39	4.48	1.934	3.808	34	30	9.24	78
3.1	center	1.6	0.2	581	1	0.006	10	0.03	0.014	0.25	1.01	0.407	0.930	14	8	3.33	37
3.2	tip	9.2	0.2	1037	3	0.012	12	0.04	0.020	0.40	1.96	0.876	2.001	41	19	7.65	91
4.1	tip	0.8	0.2	286	1	0.004	8	0.02	0.010	0.18	0.76	0.407	0.740	11	7	2.28	24
4.2	center	15.2	0.2	374	1	0.004	8	0.05	0.020	0.32	0.98	0.475	0.941	15	8	3.35	23
4.3	edge	1.5	0.2	448	1	0.004	8	0.09	0.040	0.65	2.14	1.090	2.017	19	18	5.31	42
5.1	interior	6.1	0.1	924	1	0.008	12	0.38	0.148	1.96	4.36	2.104	4.154	35	37	10.48	106

Table A2. (continued)

Spot #	Grain Location	Fe	Ge	Y	Nb	La	Ce	Ce* [a]	Pr [a]	Nd	Sm	Eu	Eu* [a]	Ho	Gd	Tb	Dy
SHD08-13Z																	
5.2	edge	1.2	0.2	613	1	0.015	10	0.06	0.027	0.43	1.44	0.808	1.531	21	15	4.82	49
5.3	tip	2.5	0.3	567	2	0.014	10	0.09	0.038	0.57	1.62	0.871	1.625	21	15	4.90	50
6.1	interior	2.9	0.3	2332	3	0.039	24	0.71	0.273	3.62	8.02	4.327	8.364	103	81	26.58	238
7.1	interior	33.2	0.3	856	1	0.006	12	0.23	0.099	1.44	3.83	1.850	3.562	34	31	9.41	85
7.2	edge	4.1	0.3	851	2	0.013	12	0.25	0.093	1.19	2.48	1.256	2.396	29	21	6.74	73
8.1	interior	5.4	0.2	2916	5	0.072	44	1.00	0.396	5.38	12.51	6.073	12.088	118	108	33.23	324
8.2	edge	8.8	0.2	3733	6	0.087	63	1.08	0.458	6.71	18.08	8.430	17.009	157	148	44.98	439
8.3	edge	2.3	0.3	821	1	0.012	15	0.27	0.106	1.46	3.47	1.579	3.156	34	27	8.41	71
9.1	interior	4.1	0.1	456	1	0.010	4	0.26	0.094	1.15	2.17	1.280	1.848	18	15	4.57	43
10.1	center	2.4	0.2	945	1	0.047	8	0.11	0.050	0.75	2.15	0.832	2.316	38	23	8.68	96
SHD08-14Z																	
1.1	center	1.0	0.2	2110	3	0.047	25	0.76	0.288	3.76	8.06	3.865	7.820	88	70	22.23	228
1.2	rim	1.2	0.1	849	2	0.003	8	0.09	0.037	0.53	1.40	0.730	1.434	32	14	5.49	68
2.1	center	10.8	0.3	1051	1	0.026	10	0.36	0.136	1.78	3.85	1.858	3.490	41	29	9.60	104
2.2	tip	1.1	0.2	1061	3	0.009	13	0.05	0.025	0.42	1.46	0.799	1.563	40	15	6.23	81
3.1	interior	1.5	0.1	599	1	0.019	10	0.33	0.119	1.48	2.85	1.474	2.372	22	18	5.36	55
3.2	interior	0.8	0.2	433	1	0.000	8	0.05	0.022	0.34	1.06	0.568	1.037	17	9	3.46	42
4.1	center	2.7	0.2	647	2	0.009	11	0.05	0.025	0.43	1.69	0.981	1.837	24	18	5.36	57
4.2	edge	1.9	0.2	355	1	0.058	8	0.06	0.025	0.36	0.98	0.446	0.816	12	6	2.47	29
4.3	edge	1.2	0.2	565	2	0.009	10	0.05	0.023	0.38	1.39	0.745	1.369	22	12	4.52	50
5.1	center	1.1	0.3	491	1	0.006	8	0.23	0.079	0.94	1.69	1.045	1.580	18	14	4.52	46
5.2	rim	1.5	0.1	1203	2	0.025	14	0.18	0.079	1.20	3.44	1.663	3.322	48	30	10.40	121
6.1	edge	57.9	0.2	573	1	0.006	10	0.11	0.048	0.75	2.26	1.113	2.067	22	17	5.59	59

Table A2. (continued)

Spot #	Grain Location	Fe	Ge	Y	Nb	La	Ce	Ce* [a]	Pr [a]	Nd	Sm	Eu	Eu* [a]	Ho	Gd	Tb	Dy
SHD08-14Z																	
6.2	center	1.0	0.2	1155	2	0.016	16	0.32	0.130	1.83	4.55	2.179	4.401	47	39	12.25	133
7.1	rim	1.5	0.1	1173	4	0.114	17	0.08	0.038	0.62	2.00	0.887	2.180	44	22	8.75	103
7.2	center	2.3	0.2	1064	2	0.016	13	0.20	0.086	1.23	3.23	1.779	3.346	49	32	11.63	131
7.3	interior	1.5	0.1	1608	6	0.003	25	0.15	0.065	0.95	2.59	1.410	2.878	61	30	11.83	142
8.1	center	1.2	0.3	1772	2	0.070	19	0.57	0.218	2.87	6.26	2.817	6.025	72	54	18.75	191
8.2	interior	2.2	0.2	1496	6	0.013	26	0.15	0.066	1.00	2.86	1.410	2.909	57	27	10.71	130
8.3	edge	1.6	0.2	795	1	0.003	13	0.45	0.158	1.88	3.38	1.598	2.882	30	23	7.36	77
9.1	interior	3.2	0.2	2135	3	0.111	22	0.70	0.262	3.37	6.99	3.522	6.935	88	64	21.71	231
10.1	tip	2.4	0.3	489	3	0.302	18	0.04	0.021	0.34	1.16	0.577	1.254	18	13	4.18	48
10.2	center	4.6	0.2	746	2	0.018	10	0.04	0.020	0.32	1.07	0.700	1.188	27	12	4.86	61
11.1	rim	2.0	0.2	537	1	0.007	7	0.03	0.016	0.26	0.87	0.475	0.939	21	9	3.71	48
11.2	center	1.4	0.2	419	1	0.006	8	0.11	0.044	0.62	1.49	0.860	1.359	16	11	3.59	41
12.1	center	1.3	0.3	544	1	0.010	9	0.07	0.031	0.46	1.31	0.783	1.349	21	13	5.05	55
12.2	interior	1.5	0.2	518	1	0.003	9	0.12	0.051	0.76	2.12	1.061	1.943	19	16	5.01	53
13.1	tip	2.8	0.1	129	1	0.010	2	0.00	0.001	0.02	0.11	0.124	0.147	4	2	0.69	10
13.2	interior	5.8	0.3	427	2	0.061	5	0.02	0.010	0.18	0.74	0.235	0.740	17	7	2.98	39
SHD08-15Z																	
1.1	center	5.1	0.2	1167	2	0.072	11	0.86	0.279	3.14	5.00	3.408	4.361	45	35	11.42	123
2.1	interior	2.6	0.2	695	1	0.010	11	0.15	0.066	1.01	2.96	1.139	2.687	27	23	7.01	73
2.2	interior	4.1	0.1	1018	1	0.027	15	0.66	0.227	2.67	4.66	2.160	4.269	41	36	11.18	117
3.1	interior	3.4	0.3	675	3	0.007	14	0.18	0.065	0.82	1.65	0.877	1.423	23	11	3.98	46
3.2	interior	3.1	0.4	496	2	0.011	9	0.05	0.023	0.38	1.34	0.579	1.195	18	10	3.69	32
4.1	edge	2.2	0.3	911	1	0.029	12	0.34	0.137	1.89	4.49	2.170	4.037	38	34	10.11	99

Table A2. (continued)

Spot #	Grain Location	Fe	Ge	Y	Nb	La	Ce	Ce* [a]	Pr [a]	Nd	Sm	Eu	Eu* [a]	Ho	Gd	Tb	Dy
SHD08-15Z																	
4.2	tip	11.4	0.3	783	3	0.026	14	0.15	0.057	0.77	1.77	0.970	1.830	29	17	5.79	70
5.1	rim	16.2	0.2	780	5	0.011	23	0.07	0.033	0.54	1.83	0.911	1.882	29	18	6.59	64
5.2	interior	71.0	0.3	786	4	0.037	13	0.02	0.012	0.23	1.11	0.536	1.326	28	15	5.31	61
5.3	center	12.1	0.2	678	1	0.015	8	0.04	0.017	0.29	1.02	0.658	1.111	23	11	4.12	52
6.1	edge	2.7	0.3	1104	1	0.012	14	0.44	0.164	2.07	4.19	1.866	4.041	46	36	11.48	111
6.2	edge	21.3	0.2	958	2	0.172	14	0.44	0.158	1.95	3.73	1.603	3.498	37	30	9.35	80
7.1	interior	9.9	0.4	2020	3	0.056	23	0.71	0.271	3.59	7.91	3.769	7.550	80	67	21.87	138
7.2	interior	1.2	0.2	170	1	0.018	5	0.00	0.002	0.05	0.36	0.151	0.325	7	3	1.21	14
8.1	center	12.0	0.2	2135	5	0.047	21	0.85	0.297	3.58	6.54	4.156	6.173	76	54	18.64	198
8.2	edge	7.7	0.3	1580	4	0.106	20	0.51	0.201	2.72	6.26	3.779	5.691	60	48	15.12	136
9.1	interior	12.3	0.2	418	1	0.212	8	0.51	0.123	1.01	0.86	0.660	0.875	15	8	2.82	28
10.1	rim	21.7	0.2	261	1	0.010	4	0.04	0.016	0.24	0.65	0.503	0.681	10	7	2.08	22
10.2	center	3.9	0.1	672	1	0.056	7	0.62	0.198	2.18	3.33	2.339	2.961	28	24	7.67	63
11.1	interior	12.3	0.2	1092	3	0.009	10	0.16	0.060	0.79	1.71	1.670	2.143	44	25	10.05	109
12.1	center	1.7	0.1	188	1	0.008	6	0.02	0.010	0.15	0.42	0.273	0.387	7	3	1.39	16
12.2	edge	1.6	0.3	684	1	0.018	12	0.28	0.107	1.39	2.94	1.379	2.607	27	21	5.99	71

[a] Measured Pr values are likely inaccurate due to potential interference with $^{140}Ce^{1}H$. Reported values of Pr and Ce* were determined by fitting a regression line through chondrite-normalized values of Nd and Sm and then calculating the values of Pr and Ce that fall along the line. Reported values of Eu* were similarly determined by fitting a regression line through chondrite-normalized values of Sm and Gd.

Table A2. (continued)

Spot #	Grain Location	Er	Tm	Yb	Lu	Hf	Th	U	$T_{Ti\text{-}in\text{-}zirc}$ (°C) [b]
SHD08-2Z									
1.1	center	74	19	173	40	9748	43	167	671
1.2	interior	262	56	498	99	10500	141	508	770
2.1	interior	51	12	111	24	12443	16	130	659
2.2	interior	79	18	159	35	11939	57	312	687
2.3	edge	107	25	218	46	10976	30	174	692
3.1	center	241	51	407	79	8170	134	269	838
3.2	interior	595	111	846	149	8920	364	539	816
4.1	center	83	20	181	39	10022	18	101	702
4.2	interior	159	36	318	67	11904	64	338	701
SHD08-3Z									
1.1	interior	95	20	178	33	11607	27	115	714
1.2	interior	177	39	334	65	9207	83	136	795
2.1	tip	37	9	87	18	11673	26	122	666
2.2	center	155	38	361	74	10794	56	332	691
2.3	interior	230	54	505	99	12116	88	555	745
3.1	interior	173	35	286	54	11172	67	181	737
4.1	center	202	41	309	57	8775	49	73	838
4.2	interior	124	28	244	48	8484	23	69	833
4.3	interior	136	30	252	48	9136	47	83	798
5.1	interior	344	69	517	88	8370	107	137	841
5.2	edge	82	17	155	27	9351	18	40	804
5.3	edge	133	30	238	47	8906	28	73	832
5.4	edge	137	30	246	48	11005	46	157	725
5.5	interior	223	43	346	60	8371	59	82	831
6.1	center	375	73	577	102	7323	30	93	874
6.2	edge	97	20	165	32	8130	5	25	780
6.3	interior	258	50	381	66	8298	28	77	888
7.1	center	224	53	465	92	11389	62	518	748
7.2	interior	130	32	298	65	11375	34	284	711
7.3	edge	153	37	331	69	9582	24	312	743
8.1	edge	127	30	276	55	8389	27	96	805
8.2	center	196	44	378	78	11005	111	378	771
9.1	interior	54	14	140	29	9573	35	88	771
9.2	interior	83	18	160	33	9193	41	72	818

Table A2. (continued)

Spot #	Grain Location	Er	Tm	Yb	Lu	Hf	Th	U	$T_{Ti\text{-}in\text{-}zirc}$ (°C) [b]
SHD08-3Z									
10.1	tip	205	46	378	70	10888	70	241	762
10.2	center	153	33	253	48	8427	37	64	831
10.3	interior	133	27	217	37	8768	29	52	811
10.4	interior	58	15	146	31	8979	24	71	790
SHD08-5Z									
1.1	tip	156	31	262	48	11602	106	296	752
1.2	interior	60	13	118	22	10904	61	364	753
2.1	rim	123	28	257	50	9588	32	102	790
2.2	center	165	38	343	69	11778	80	470	745
3.1	interior	131	30	286	59	8672	29	99	816
3.2	interior	107	23	193	38	8716	18	52	795
4.1	center	473	91	690	120	8494	166	188	853
4.2	edge	76	18	170	35	9858	27	66	771
5.1	edge	59	14	139	29	13317	26	247	647
5.2	center	135	32	297	61	12035	41	347	693
6.1	interior	219	50	462	90	7694	488	539	829
6.2	tip	20	5	47	11	11427	25	114	672
7.1	tip	118	25	198	37	12377	75	257	684
7.2	center	108	22	182	33	8783	27	48	808
8.1	tip	141	30	254	48	11842	100	322	726
8.2	center	172	36	325	61	11205	106	479	757
9.1	rim	61	14	130	28	9997	19	86	696
9.2	center	287	57	422	73	9823	128	225	907
10.1	center	144	29	237	42	9296	32	67	791
10.2	rim	221	46	377	71	10647	113	337	779
11.1	center	166	35	308	60	7646	81	133	848
11.2	interior	42	10	86	17	11423	40	129	714
12.1	interior	132	28	255	49	8536	62	161	758
12.2	interior	387	80	669	123	9018	309	535	811
SHD08-8Z									
1.1	center	82	17	145	28	8482	18	38	789
1.2	edge	236	47	375	68	8781	69	101	818
2.1	tip	225	46	377	72	11053	76	257	755
2.2	center	325	63	475	86	8285	147	145	946

Table A2. (continued)

Spot #	Grain Location	Er	Tm	Yb	Lu	Hf	Th	U	$T_{Ti\text{-}in\text{-}zirc}$ (°C) [b]
SHD08-8Z									
2.3	rim	227	45	359	67	11689	101	254	706
3.1	center	207	47	426	83	8656	41	158	817
3.2	rim	181	37	310	59	10942	53	191	725
4.1	center	119	27	268	57	12208	45	266	666
4.2	rim	184	39	318	61	10409	56	204	756
5.1	center	234	48	378	67	8611	76	105	836
5.2	tip	172	36	295	55	11282	52	201	738
6.1	tip	115	28	245	48	12542	67	495	676
6.2	center	128	30	283	58	11076	42	305	709
7.1	center	322	67	536	97	9092	146	249	786
7.2	edge	218	46	388	72	10635	176	377	759
8.1	rim	69	16	146	29	8966	17	42	787
8.2	center	121	30	272	60	10729	35	255	711
9.1	center	208	51	497	110	7711	527	957	750
9.2	edge	230	47	380	72	10755	68	249	752
SHD08-12Z									
1.1	center	301	62	505	93	8959	90	157	863
1.2	interior	187	43	382	79	8346	44	140	815
2.1	center	90	21	197	40	12771	28	163	701
2.2	edge	173	37	326	62	8317	35	88	845
2.3	edge	81	18	145	28	9127	15	35	811
3.1	interior	36	9	81	17	10369	10	30	771
3.2	interior	33	7	74	16	10898	10	30	748
4.1	edge	55	13	122	26	11806	22	72	912
4.2	center	61	14	122	25	10737	24	49	770
5.1	center	155	29	231	39	10247	59	98	880
5.2	interior	83	18	141	25	10409	48	98	877
6.1	tip	121	25	207	39	12206	70	243	690
6.2	center	50	11	109	23	7345	15	41	791
7.1	interior	155	34	320	64	8861	31	108	822
7.2	interior	94	20	171	32	9098	16	40	810
7.3	edge	105	24	208	41	9742	51	91	786
7.4	tip	95	21	209	43	9488	17	73	780
8.1	interior	209	48	458	96	12037	92	589	726

Table A2. (continued)

Spot #	Grain Location	Er	Tm	Yb	Lu	Hf	Th	U	$T_{Ti\text{-}in\text{-}zirc}$ (°C) [b]
SHD08-12Z									
8.2	center	151	36	343	70	10470	47	303	712
9.1	center	95	21	183	36	12672	117	201	691
9.2	rim	53	13	113	22	9947	16	46	798
10.1	center	248	49	376	68	8613	67	100	831
10.2	edge	66	15	146	30	10036	18	51	780
11.1	center	459	93	789	141	9343	545	748	792
11.3	tip	146	31	281	53	10773	163	341	744
SHD08-13Z									
1.1	interior	178	36	329	60	11042	52	198	747
1.2	center	74	14	119	23	8856	15	29	792
2.1	interior	164	34	289	52	9174	51	90	802
3.1	center	87	21	206	46	9972	32	178	674
3.2	tip	170	36	305	55	10446	55	201	837
4.1	tip	51	11	100	19	10362	10	30	786
4.2	center	64	15	102	24	9515	12	32	799
4.3	edge	87	18	144	28	8117	22	39	748
5.1	interior	150	31	245	43	8840	37	53	818
5.2	edge	96	21	167	32	8432	19	40	818
5.3	tip	98	24	197	38	8494	20	55	829
6.1	interior	450	88	682	112	8997	132	162	852
7.1	interior	148	30	239	43	9868	36	58	807
7.2	edge	144	31	271	51	8655	36	77	820
8.1	interior	467	91	711	124	8220	216	231	837
8.2	edge	631	123	915	155	8522	240	248	842
8.3	edge	142	30	240	43	9120	41	73	812
9.1	interior	79	17	143	29	6614	20	40	777
10.1	center	173	36	288	55	10738	32	51	789
SHD08-14Z									
1.1	center	356	68	527	93	8671	114	149	831
1.2	rim	146	33	291	60	8572	36	108	802
2.1	center	188	41	351	67	8549	60	134	779
2.2	tip	190	44	395	81	9636	55	202	779
3.1	interior	98	22	194	40	9772	47	87	768
3.2	interior	76	16	142	26	9013	11	31	805

Table A2. (continued)

Spot #	Grain Location	Er	Tm	Yb	Lu	Hf	Th	U	$T_{Ti\text{-}in\text{-}zirc}$ (°C) [b]
SHD08-14Z									
4.1	center	98	20	170	32	10311	72	178	747
4.2	edge	62	16	152	33	10627	27	77	764
4.3	edge	102	22	193	37	8622	19	50	829
5.1	center	80	18	158	30	9539	23	48	777
5.2	rim	229	51	426	84	9740	85	204	780
6.1	edge	96	21	180	32	9991	26	51	790
6.2	center	204	41	328	59	8802	51	83	820
7.1	rim	201	44	382	76	10927	98	307	747
7.2	center	253	55	506	97	9543	114	322	738
7.3	interior	280	60	511	102	10377	119	417	770
8.1	center	308	61	476	87	9137	93	133	826
8.2	interior	281	60	496	91	8877	72	163	871
8.3	edge	140	31	288	59	11479	95	185	734
9.1	interior	364	73	563	100	8521	120	159	832
10.1	tip	88	20	178	36	12466	187	472	693
10.2	center	140	33	309	67	10838	37	274	701
11.1	rim	105	24	218	44	9463	26	85	775
11.2	center	74	16	147	30	10270	26	52	775
12.1	center	97	21	174	33	8592	16	40	811
12.2	interior	93	22	196	39	11985	59	134	729
13.1	tip	26	6	64	13	13008	14	147	626
13.2	interior	81	18	158	29	10191	12	40	799
SHD08-15Z									
1.1	center	201	47	401	81	8120	101	178	793
2.1	interior	118	23	194	36	9634	30	51	789
2.2	interior	178	36	285	53	9493	57	88	808
3.1	interior	116	31	271	61	9669	45	135	818
3.2	interior	89	22	200	43	8970	29	76	803
4.1	edge	156	31	245	43	8960	37	56	798
4.2	tip	138	30	261	49	8804	33	79	841
5.1	rim	133	31	273	56	12064	201	701	713
5.2	interior	130	29	271	54	12244	57	422	694
5.3	center	111	28	257	56	12295	35	287	674
6.1	edge	201	41	322	61	9062	65	93	810

Table A2. (continued)

Spot #	Grain Location	Er	Tm	Yb	Lu	Hf	Th	U	$T_{Ti\text{-}in\text{-}zirc}$ (°C) [b]
SHD08-15Z									
6.2	edge	151	31	253	45	8910	38	66	826
7.1	interior	315	64	481	86	8174	107	133	839
7.2	interior	31	7	65	14	11951	13	64	684
8.1	center	333	71	592	114	9163	270	412	778
8.2	edge	247	54	454	87	10794	251	339	759
9.1	interior	70	17	162	35	9815	68	151	814
10.1	rim	47	11	93	19	9104	18	44	796
10.2	center	121	26	230	46	7499	77	138	802
11.1	interior	212	47	406	78	7780	72	121	855
12.1	center	35	8	81	18	11404	12	36	762
12.2	edge	132	30	284	51	12222	59	117	774

[b] Ti-in-zircon temperature calculated using the calibration of Ferry and Watson (2007). We utilized activity values of 1 for SiO_2 and 0.7 for TiO_2.

REFERENCES

Bachmann, O., Dungan, M.A., and Bussy, F. (2005) Insights into shallow magmatic processes in large silicic magma bodies: The trace element record in the Fish Canyon magma body, Colorado. *Contributions to Mineralogy and Petrology* **149**(3), p. 338–349.

Bachmann, O., Miller, C.F., and de Silva, S.L. (2007) The volcanic-plutonic connection as a stage for understanding crustal magmatism. *Journal of Volcanology and Geothermal Research* **167**(1–4), p. 1–23.

Bacon, C.R., and Druitt, T.H. (1988) Compositional evolution of the zoned calcalkaline magma chamber of Mount Mazama, Crater Lake, Oregon. *Contributions to Mineralogy and Petrology* **98**(1/2), p. 224–256.

Bacon, C.R., and Lowenstern, J.B. (2005) Late Pleistocene granodiorite source for recycled zircon and phenocrysts in rhyodacite lava at Crater Lake, Oregon. *Earth and Planetary Science Letters* **233**(3/4), p. 277–293.

Baker, V.R., and Bunker, R.C. (1985) Cataclysmic late Pleistocene flooding from glacial Lake Missoula: A review. *Quaternary Science Reviews* **4**(1), p. 1–41.

Bea, F., Montero, P., and Ortega, M. (2006) A LA-ICP-MS evaluation of Zr reservoirs in common crustal rocks: Implications for Zr and Hf geochemistry and zircon-forming processes. *The Canadian Mineralogist* **44**(3), p. 693–714.

Berlo, K., Turner, S., Blundy, J., and Hawkesworth, C. (2004) The extent of U-series disequilibria produced during partial melting of the lower crust with implications for the formation of the Mount St. Helens dacites. *Contributions to Mineralogy and Petrology* **148**(1), p. 122–130.

Blundy, J., and Cashman, K. (2005) Rapid decompression-driven crystallization recorded by melt inclusions from Mount St. Helens volcano. *Geology* **33**(10), p. 793–796.

Bolhar, R., Weaver, S.D., Palin, J.M., Cole, J.W., and Paterson, L.A. (2008) Systematics of zircon crystallisation in the Cretaceous Separation Point Suite, New Zealand, using U/Pb isotopes, REE and Ti geothermometry. *Contributions to Mineralogy and Petrology* **156**(2), p. 133–160.

Booth, A.L., Zeitler, P.K., Kidd, W.S.F., Wooden, J., Liu, Y., Idleman, B., Hren, M., and Chamberlain, C.P. (2004) U-Pb zircon constraints on the tectonic evolution of southeastern Tibet, Namche Barwa area. *American Journal of Science* **304**(10), p. 889–929.

Cherniak, D.J., Hanchar, J.M., and Watson, E.B. (1997a) Diffusion of tetravalent cations in zircon. *Contributions to Mineralogy and Petrology* **127**(4), p. 383–390.

Cherniak, D.J., Hanchar, J.M., and Watson, E.B. (1997b) Rare-earth diffusion in zircon. *Chemical Geology* **134**(4), p. 289–301.

Cherniak, D.J., and Watson, E.B. (2003) Diffusion in zircon. In: Hanchar, J.M., and Hoskin, P.W.O. (eds.), *Zircon*. Mineralogical Society of America, Reviews in Mineralogy and Geochemistry **53**, p. 113–143.

Cherniak, D.J., and Watson, E.B. (2007) Ti diffusion in zircon. *Chemical Geology* **242**(3/4), p. 470–483.

Clague, J.J., Barendregt, R., Enkin, R.J., and Foit, F.F., Jr. (2003) Paleomagnetic and tephra evidence for tens of Missoula floods in southern Washington. *Geology* **31**(3), p. 247–250.

Claiborne, L.L., Miller, C.F., Flanagan, D.M., Clynne, M.A., and Wooden, J.L. Zircon reveals protracted magma storage and recycling beneath Mount St. Helens. In preparation for *Geology*.

Claiborne, L.L., Miller, C.F., Wooden, J.L., and Mazdab, F.K. (in revision) Trace element composition of igneous zircon: A thermal and compositional record of the accumulation and evolution of a large silicic batholith. *Contributions to Mineralogy and Petrology*.

Clynne, M.A., Calvert, A.T., Wolfe, E.W., Evarts, R.C., Fleck, R.J., and Lanphere, M.A. (2008) The Pleistocene eruptive history of Mount St. Helens, Washington, from 300,000 to 12,800 years before present. In: Sherrod, D.R., Scott, W.E., and Stauffer, P.H. (eds.), *A Volcano Rekindled: The Renewed Eruption of Mount St. Helens, 2004–2006*. U.S. Geological Survey Professional Paper **1750**, p. 593–627.

Coleman, D.S., Gray, W., and Glazner, A.F. (2004) Rethinking the emplacement and evolution of zoned plutons: Geochronologic evidence for incremental assembly of the Tuolumne Intrusive Suite, California. *Geology* **32**(5), p. 433–436.

Cooper, K.M., and Reid, M.R. (2003) Re-examination of crystal ages in recent Mount St. Helens lavas: Implications for magma reservoir processes. *Earth and Planetary Science Letters* **213**(1/2), p. 149–167.

Cooper, K.M., and Donnelly, C.T. (2008) ^{238}U-^{230}Th-^{226}Ra disequilibria in dacite and plagioclase from the 2004–2005 eruption of Mount St. Helens. In: Sherrod, D.R., Scott, W.E., and Stauffer, P.H. (eds.), *A Volcano Rekindled: The Renewed Eruption of Mount St. Helens, 2004–2006*. U.S. Geological Survey Professional Paper **1750**, p. 827–846.

Crandell, D.R., Mullineaux, D.R., Rubin, M., Spiker, E., and Kelley, M.L. (1981) *Radiocarbon dates from volcanic deposits at Mount St. Helens, Washington*. U.S. Geological Survey Open-File Report **81-844**, 15 p.

Crandell, D.R. (1987) *Deposits of Pre-1980 Pyroclastic Flows and Lahars from Mount St. Helens Volcano, Washington*. U.S. Geological Survey Professional Paper **1444**, 89 p.

Defant, M.J., and Drummond, M.S. (1993) Mount St. Helens: Potential example of the partial melting of the subducted lithosphere in a volcanic arc. *Geology* **21**(6), p. 547–550.

Evarts, R.C., Ashley, R.P., and Smith, J.G. (1987) Geology of the Mount St. Helens area: Record of discontinuous volcanic and plutonic activity in the Cascade arc of southern Washington. *Journal of Geophysical Research–Solid Earth* **92**(B10), p. 10155–10169.

Fairbanks, R.G., Mortlock, R.A., Chiu, T.-C., Cao, L., Kaplan, A., Guilderson, T.P., Fairbanks, T.W., Bloom, A.L., Grootes, P.M., and Nadeau, M.-J. (2005) Radiocarbon calibration curve spanning 0 to 50,000 years BP based on paired $^{230}Th/^{234}U/^{238}U$ and ^{14}C dates on pristine corals. *Quaternary Science Reviews* **24**(16/17), p. 1781–1796.

Ferriss, E.D.A., Essene, E.J., and Becker, U. (2008) Computational study of the effect of pressure on the Ti-in-zircon geothermometer. *European Journal of Mineralogy* **20**(5), p. 745–755.

Ferry, J.M., and Watson, E.B. (2007) New thermodynamic models and revised calibrations for the Ti-in-zircon and Zr-in-rutile thermometers. *Contributions to Mineralogy and Petrology* **154**(4), p. 429–437.

Fu, B., Page, F.Z., Cavosie, A.J., Fournelle, J., Kita, N.T., Lackey, J.S., Wilde, S.A., and Valley, J.W. (2008) Ti-in-zircon thermometry: Applications and limitations. *Contributions to Mineralogy and Petrology* **156**(2), p. 197–215.

Fujimaki, H. (1986) Patition coefficient of Hf, Zr, and REE between zircon, apatite, and liquid. *Contributions to Mineralogy and Petrology* **94**(1), p. 42–45.

Gardner, J.E., Carey, S., Rutherford, M.J., and Sigurdsson, H. (1995) Petrologic diversity in Mount St. Helens dacites during the last 4,000 years: Implications for magma mixing. *Contributions to Mineralogy and Petrology* **119**(2/3), p. 224–238.

Glazner, A.F., Bartley, J.M., Coleman, D.S., Gray, W., and Taylor, R.Z. (2004) Are plutons assembled over millions of years by amalgamation from small magma chambers? *GSA Today* **14**(4/5), p. 4–11.

Halliday, A.N., Fallick, A.E., Dickin, A.P., Mackenzie, A.B., Stephens, W.E., and Hildreth, W. (1983) The isotopic and chemical evolution of Mount St. Helens. *Earth and Planetary Science Letters* **63**(2), p. 241–256.

Hayden, L.A., and Watson, E.B. (2007) Rutile saturation in hydrous siliceous melts and its bearing on Ti-thermometry of quartz and zircon. *Earth and Planetary Science Letters* **258**(3/4), p. 561–568.

Hill, G.J., Caldwell, T.G., Heise, W., Chertkoff, D.G., Bibby, H.M., Burgess, M.K., Cull, J.P., and Cas, R.A.F. (2009) Distribution of melt beneath Mount St Helens and Mount Adams inferred from magnetotelluric data. *Nature Geoscience* **2**(11), p. 785–789.

Hofmann, A.E., Valley, J.W., Watson, E.B., Cavosie, A.J., and Eiler, J.M. (2009) Sub-micron scale distribution of trace elements in zircon. *Contributions to Mineralogy and Petrology* **158**(3), p. 317–335.

Hoskin, P.W.O., and Schaltegger, U. (2003) The composition of zircon and igneous and metamorphic petrogenesis. In: Hanchar, J.M., and Hoskin, P.W.O. (eds.), *Zircon*. Mineralogical Society of America, Reviews in Mineralogy and Geochemistry **53**, p. 27–62.

Hyde, J.H. (1975) *Upper Pleistocene pyroclastic-flow deposits and lahars south of Mount St. Helens volcano, Washington*. U.S. Geological Survey Bulletin **1383-B**, 20 p.

Le Bas, M.J., Le Maitre, A., Streckeisen, A., and Zanettin, B. (1986) A chemical classification of volcanic rocks based on the total alkali-silica diagram. *Journal of Petrology* **27**(3), p. 745–750.

Lipman, P.W. (2007) Incremental assembly and prolonged consolidation of Cordilleran magma chambers: Evidence from the Southern Rocky Mountain volcanic field. *Geosphere* **3**(1), p. 42–70.

Lowery Claiborne, L., Miller, C.F., Walker, B.A., Wooden, J.L., Mazdab, F.K., and Bea, F. (2006) Tracking magmatic processes through Zr/Hf ratios in rocks and Hf and Ti zoning in zircons: An example from the Spirit Mountain batholith, Nevada. *Mineralogical Magazine* **70**(5), p. 517–543.

Ludwig, K.R. (2003) *Isoplot 3.00: A Geochronological Toolkit for Microsoft Excel*. Berkeley Geochronology Center Special Publication **4**, 70 p.

Major, J.J., and Scott, K.M. (1988) *Volcaniclastic sedimentation in the Lewis River valley, Mount St. Helens, Washington — Processes, extent, and hazards*. U.S. Geological Survey Bulletin **1383-D**, 38 p.

Miller, J.S., Matzel, J.E.P., Miller, C.F., Burgess, S.D., and Miller, R.B. (2007) Zircon growth and recycling during the assembly of large, composite arc plutons. *Journal of Volcanology and Geothermal Research* **167**(1–4), p. 282–299.

Mullineaux, D.R., and Crandell, D.R. (1981) The eruptive history of Mount St. Helens. In: Lipman, P.W., and Mullineaux, D.R. (eds.), *The 1980 Eruptions of Mount St. Helens, Washington*. U.S. Geological Survey Professional Paper **1250**, p. 3–15.

Mullineaux, D.R. (1996) *Pre-1980 tephra-fall deposits erupted from Mount St. Helens, Washington*. U.S. Geological Survey Professional Paper **1563**, 99 p.

Pallister, J.S., Hoblitt, R.P., Crandell, D.R., and Mullineaux, D.R. (1992) Mount St. Helens a decade after the 1980 eruptions: Magmatic models, chemical cycles, and a revised hazards assessment. *Bulletin of Volcanology* **54**(2), p. 126–146.

Pallister, J.S., Thornber, C.R., Cashman, K.V., Clynne, M.A., Lowers, H.A., Mandeville, C.W., Brownfield, I.K., and Meeker, G.P. (2008) Petrology of the 2004–2006 Mount St. Helens lava dome — Implications for magmatic plumbing and eruption triggering. In: Sherrod, D.R., Scott, W.E., and Stauffer, P.H. (eds.), *A Volcano Rekindled: The Renewed Eruption of Mount St. Helens, 2004–2006*. U.S. Geological Survey Professional Paper **1750**, p. 647–702.

Rutherford, M.J., Sigurdsson, H., Carey, S., and Davis, A. (1985) The May 18, 1980 eruption of Mount St. Helens 1. Melt composition and experimental phase equilibria. *Journal of Geophysical Research–Solid Earth* **90**(B4), p. 2929–2947.

Rutherford, M.J., and Devine, J.D., III (2008) Magmatic conditions and processes in the storage zone of the 2004–2006 Mount St. Helens dacite. In: Sherrod, D.R., Scott, W.E., and Stauffer, P.H. (eds.), *A Volcano Rekindled: The Renewed Eruption of Mount St. Helens, 2004–2006*. U.S. Geological Survey Professional Paper **1750**, p. 703–725.

Sambridge, M.S., and Compston, W. (1994) Mixture modeling of multi-component data sets with application to ion-probe zircon ages. *Earth and Planetary Science Letters* **128**(3/4), p. 373–390.

Shane, P., Smith, V.C., and Nairn, I. (2008) Millenial timescale resolution of rhyolite magma recharge at Tarawera volcano: Insights from quartz chemistry and melt inclusions. *Contributions to Mineralogy and Petrology* **156**(3), p. 397–411.

Sisson, T.W. (1994) Hornblende-melt trace element partitioning measured by ion microprobe. *Chemical Geology* **117**(1–4), p. 331–344.

Smith, D.R., and Leeman, W.P. (1987) Petrogenesis of Mount St. Helens dacitic magmas. *Journal of Geophysical Research–Solid Earth* **92**(B10), p. 10313–10334.

Smith, D.R., and Leeman, W.P. (1993) The origin of Mount St. Helens andesites. *Journal of Volcanology and Geothermal Research* **55**(3/4), p. 271–303.

Sun, S.-s., and McDonough, W.F. (1989) Chemical and isotopic systematics of oceanic basalts: Implications for mantle composition and processes. In: Saunders, A.D., and Norry, M.J. (eds.), *Magmatism in the Ocean Basins*. Geological Society [London] Special Publication **42**, p. 313–345.

Waitt, R.B., Jr. (1985) Case for periodic, colossal jökulhlaups from Pleistocene glacial Lake Missoula. *Geological Society of America Bulletin* **96**(10), p. 1271–1286.

Walker, B.A., Jr., Miller, C.F., Lowery Claiborne, L., Wooden, J.L., and Miller, J.S. (2007) Geology and geochronology of the Spirit Mountain batholith, southern Nevada: Implications for timescales and physical processes of batholith construction. *Journal of Volcanology and Geothermal Research* **167**(1–4), p. 239–262.

Watson, E.B., and Harrison, T.M. (1983) Zircon saturation revisited: Temperature and composition effects in a variety of crustal magma types. *Earth and Planetary Science Letters* **64**(2), p. 295–304.

Watson, E.B., and Harrison, T.M. (2005) Zircon thermometer reveals minimum melting conditions on earliest Earth. *Science* **308**(5723), p. 841–844.

Watson, E.B., Wark, D.A., and Thomas, J.B. (2006) Crystallization thermometers for zircon and rutile. *Contributions to Mineralogy and Petrology* **151**(4), p. 413–433.

Weaver, C.S., Grant, W.C., and Shemeta, J.E. (1987) Local crustal extension at Mount St. Helens, Washington. *Journal of Geophysical Research–Solid Earth* **92**(B10), p. 10170–10178.

Wilson, C.J.N., and Charlier, B.L.A. (2009) Rapid rates of magma generation at contemporaneous magma systems,Taupo volcano, New Zealand: Insights from U-Th model-age spectra in zircons. *Journal of Petrology* **50**(5), p. 875–907.